Spring 2019

Predicting floods from space: a case study of Puerto Rico

Anthony James Emigh
University of Iowa

Follow this and additional works at: https://ir.uiowa.edu/etd
Part of the Civil and Environmental Engineering Commons

PREDICTING FLOODS FROM SPACE: A CASE STUDY OF PUERTO RICO

by

Anthony James Emigh

A thesis submitted in partial fulfillment
of the requirements for the Master of Science
degree in Civil and Environmental Engineering in the
Graduate College of
The University of Iowa

May 2019

Thesis Supervisor: Professor Witold F. Krajewski

ACKNOWLEDGEMENTS

Thank you Professor Witold Krajewski for your guidance, support, and especially your patience. It has been a privilege and pleasure to work with you. For as many skills I have gained as your student, I have also learned many lessons about myself. I appreciate your dedication as an advisor and a coach.

To my committee members, Allen Bradley, Ricardo Mantilla, and Witold Krajewski, thank you for helping shape my entire collegiate education. I can hang my experience as an engineering student on posts you have set- from my first class as an undergraduate to construction sites abroad to the publication of this thesis.

Thank you to my colleagues at IIHR. Many of you have taught me essential skills and dug me out of holes, making this research possible, including Felipe Quintero, Andre Della Libera Zanchetta, Maral Razmand, Ganesh Ghimire, Ray Hammond, and Radek Goska. Thank you to the administrative and computer staff of IIHR and the Department of Civil and Environmental Engineering for your hard work and enthusiasm.

Thank you to the staff of the Hydrologic Research Center for hosting me for Step Three training of the Flash Flood Guidance system. Kosta Georgakakos, Bob Jubach, Eylon Shamir, Theresa Modrick, Rochelle Campbell, Jason Sperfslage, Randall Banks, and Zhengyang Cheng, your passion and expertise truly inspires me. Thank you to my fellow trainees from Indonesia, Malaysia, Brunei, Timor-Leste, the Philippines, Myanmar, Papua New Guinea, and Israel for your warm friendship. Your unique perspectives have greatly widened my own.

To my friends and family, your support is always appreciated and never taken for granted.

ABSTRACT

Floods are a significant threat to communities around the world and require substantial resources and infrastructure to predict. Limited local resources in developing nations make it difficult to build and maintain dense sensor networks like those present in the United States, creating a large disparity in flood prediction across borders. To address this disparity, I operated the Iowa Flood Center Top Layer model to predict floods in Puerto Rico without relying on in-situ data measurements. Instead, all model forcing was provided by satellite remote sensing datasets that offer near-global coverage.

I used three datasets gathered via satellite remote sensing to build and operate watershed streamflow models: elevation data obtained by the Space Shuttle Endeavour through the Shuttle Radar Topography Mission (SRTM), rainfall estimates gathered by a constellation of satellites through the Global Precipitation Measurement Mission (GPM), and evapotranspiration rate estimates collected by Moderate Resolution Imaging Spectroradiometer (MODIS) sensors aboard the Aqua and Terra satellites. While these satellite remote sensing datasets make observations of nearly the entire world, their spatiotemporal resolution is coarse compared to conventional on-the-ground measurements.

Hydrologic models were assembled for 75 basins upstream of streamflow gages monitored by the United States Geologic Survey (USGS). Model simulations were compared to real-time measurements at these gages. Continuous simulations spanning 58 months achieve poor Nash Sutcliffe Efficiency and Klinge Gupta Efficiency of -112.0 and -0.5, respectively. The sources of error that influence model performance were investigated, underlining some limitations of relying solely on satellite data for operational flood prediction efforts.

PUBLIC ABSTRACT

Floods are a significant threat to communities around the world and require substantial resources and infrastructure to predict. Limited local resources in developing nations make it difficult to build and maintain dense on-the-ground sensor networks like those present in the United States, creating a large disparity in flood prediction across borders. To address this disparity and help predict floods in Puerto Rico, I have built a series of hydrologic models that rely on free and readily available data gathered by satellites. Hydrologic models are capable of simulating streamflow at locations ungauged by stream sensors. Flood-related satellite data is available from the National Aeronautics and Space Administration (NASA) Global Precipitation Measurement (GPM) Mission and Shuttle Radar Topography Mission (SRTM), among others. Operating hydrologic models with only globally available satellite data from these sources is a strategy available to predict floods for nearly any resource-constrained community, but its accuracy is not fully understood.

The objective of this research is to test the capabilities of hydrologic models to provide accurate streamflow predictions across the main island of Puerto Rico. Models were assembled for 75 basins upstream of on-the-ground streamflow gages monitored by the United States Geologic Survey (USGS). Flood model outputs were compared to real-time measurements at these 75 locations, showing limited accuracy. The sources of error that influence the accuracy of the models were investigated, underlining some limitations of relying solely on satellite remote sensing data for operational flood prediction efforts.

TABLE OF CONTENTS

LIST OF TABLES

LIST OF FIGURES

CHAPTER 1: INTRODUCTION

In the past 50 years, 90% of all recorded natural disasters were flood related. Moreover, natural disasters like floods are occurring nearly five times as often as they were in the 1970s, with both developed and developing countries bearing the burden of repeated floods (World Meteorological Organization, 2014). To become resilient, communities must be able to prepare themselves by predicting floods locally. However, traditional flood prediction strategies rely on measurement of on-the-ground data, requiring substantial financial resources, expertise, and infrastructure. Such information is simply not available to all vulnerable communities. Instead, flood conditions can be simulated where measurement is not feasible by taking advantage of remotely sensed data. Many satellites orbit Earth to measure flood-related data here and now. Their observations cover the globe and cost individual communities nothing. This research was then motivated by one question: Can we predict floods from space?

1.1 Motivation

Satellite measurements of rainfall, evapotranspiration, and terrain topography are powerful because they are freely available and offer global coverage. As such, they benefit both communities rich and poor. This research attempts to address the disparity between well-informed, flood-resilient communities like many across Iowa and communities that are left victim to flood-related natural disasters.

The Iowa Flood Center (IFC) was established at the University of Iowa in 2009 after the devastating floods of 2008 highlighted a critical lack of publically-available flood information (Krajewski et al., 2017). The IFC was charged by the Iowa legislature to improve the availability of flood-relevant information to Iowans. The IFC's projects include the deployment of over 250 bridge-mounted stream-stage sensors and the creation of a community flood inundation map library. Most notably, the IFC developed an operational statewide, real-time flood forecasting system that forces evapotranspiration and radar rainfall inputs into a rainfall-runoff distributed model with streamflow routing.

While stream sensors monitor the current behavior of rivers where they are installed, hydrologic models serve an important role in flood prediction. Hydrologic models are capable of estimating river flows at ungauged locations throughout the river network. Hydrologic models represent the basin-scale water balance with a series of equations that partition rainfall and upstream flow between storage in the soil, evapotranspiration, and downstream flow. If rainfall, evapotranspiration, and soil composition can be accurately represented, streamflow is simply estimated by balancing storage and flux rates (Ajami, Gupta, Wagener, & Sorooshian, 2004). The IFC model provides streamflow predictions for over 2,000 points on the river network across Iowa including 1,000 communities (Krajewski et al., 2017). A priority of the IFC staff is to provide flood-relevant information to the public, emergency management, and state and local authorities through an interactive online portal called Iowa Flood Information System (IFIS) (Demir & Krajewski, 2013).

However, there are no such information resources for communities in Nicaragua, a developing country in Central America that suffered over 3,800 fatalities from Hurricane Mitch in 1998, a storm that never entered its borders; in Bangladesh, a developing country in South Asia whose citizens account for 2.2% of the world population and over 16.5% of the world population exposed to flood risk according to the World Resources Institute (WRI) Aqueduct Global Flood Analyzer; in Myanmar, a developing country in Southeast Asia that lost over 138,000 lives in the Ayeyarwady delta in 2008 from storm surge and intense rain cause by tropical storm Nargis; and in Afghanistan, a developing nation in the Middle East that had no flood hazard maps or federal data records on the occurrence and impact of floods until after 2010 (Basha & Rus, 2008; Brakenridge et al., 2017; Hagen & Teufer, 2009; Ivette Gómez, Munk Ravnborg, & Rivas Hermann, 2007; Thwin, Chan, Fritz, Thu, & Blount, 2011; United Nations Department of Economic and Social Affairs, 2018; Ward et al., 2013; Winsemius, Van Beek, Jongman, Ward, & Bouwman, 2013). Developing countries across the world simply lack the resources to invest in the necessary tools to effectively predict floods at a local level. If efforts by the Iowa Flood Center represent the cutting edge, chronic vulnerability to floods in resource-constrained communities is the status quo.

1.2 Objective

The objective of this research is to evaluate the performance of a regional hydrologic model driven exclusively by satellite remote sensing data. Developing communities may not be monitored by meteorological and soil sensors if they lack stream sensors so direct measurement of inputs for hydrologic models can be unfeasible. By operating a hydrologic model using only satellite data, this research tests the capability of flood models in the most difficult scenario where no in-situ measurements of a watershed's physical characteristics, meteorology, or state are available. Understanding the performance of this approach may establish a baseline for flood prediction in the most data scarce areas of the world.

1.3 Approach

The current standard hydrologic model used by the Iowa Flood Center was operated in 75 gauged watersheds on the main island of Puerto Rico to continuously simulate streamflow. Puerto Rico is an appropriate study area for this research because it shares both socioeconomic and hydro-meteorological characteristics of nearby developing countries in the western hemisphere tropical region. Moreover, due to its commonwealth status, Puerto Rico is actively monitored by the United States Geological Survey (USGS), National Weather Service (NWS), United States Army Corps of Engineers (USACE), the National Oceanic and Atmospheric Administration (NOAA) and commonwealth agencies, allowing for evaluation of model performance and satellite data accuracy by comparison to on-the-ground measurements. To build and force these models, I have used three datasets gathered via satellite remote sensing to build and operate watershed streamflow models: elevation data obtained by the Space Shuttle Endeavour through the Shuttle Radar Topography Mission (SRTM), rainfall estimates gathered by a constellation of satellites through the Global Precipitation Measurement Mission (GPM), and evapotranspiration rate estimates collected by Moderate Resolution Imaging Spectroradiometer (MODIS) sensors aboard the Aqua and Terra satellites. Each model was built and organized using SRTM data, while GPM and MODIS data provided all model forcing.

CHAPTER 2: LITERATURE REVIEW

2.1 Introduction

Many modelling efforts have indirectly used satellite observations to perform validation, calibration, parameter estimation, and risk assessment (Di Baldassarre, Schumann, & Bates, 2009; García-Pintado, Neal, Mason, Dance, & Bates, 2013; Scanlon et al., 2006; Schumann & Di Baldassarre, 2010; Schumann et al., 2007; Skakun, Kussul, Shelestov, & Kussul, 2014; Stephens, Bates, Freer, & Mason, 2012; Tramblay et al., 2012; Yan, Di Baldassarre, Solomatine, & Schumann, 2015). Still, direct use of satellite remote sensing data to directly drive the lumped and distributed hydrologic models described in Chapter 2.2 has not yet been fully explored. As discussed in Chapter 2.3, satellite estimation of precipitation and rainfall has advanced rapidly, offering benefits that may not supersede that of existing sensor networks in developed areas. Regions in the developing world will likely benefit most from flood-related satellite remote sensing data, as they are also most vulnerable to floods. Perhaps the most relevant application of satellite remote sensing data for flood prediction in such communities is the Flash Flood Guidance System (FFGS) developed by the World Meteorological Organization (WMO) and Hydrologic Research Center (HRC), as discussed in Chapter 2.4.

2.2 Hydrologic Modelling

The development of hydrologic models began 5 decades ago and has been greatly advanced by high performance computing, remote sensing techniques, and geographic information systems (GIS). Lumped models were initially applied during the first phase of hydrologic model development, due to computational limits. Spatial variability of the landscape characteristics, hydro-meteorological forcings, or antecedent conditions were not accounted for by these models. To overcome such challenges, effective parameters were heavily calibrated to match simulations to observed streamflow behavior based on the hydrographs at watershed outlets. Parameter calibration can allow for correct overall mass balance but may falter in accurately representing physical processes throughout the catchment. Perhaps calibration is wholly justifiable when data is sparse and the ultimate use is for operational predictions of streamflow. However, with the advancement of GIS technology and remote sensing techniques, an abundance of near-global data has been made available to describe a watershed's physical characteristics (e.g. topography, land cover, soil properties), hydro-meteorological fluxes (e.g. precipitation and evapotranspiration), and state (e.g. soil moisture). As such, modern lumped models are physically-based, representing the processes that occur in the watershed via control volumes that influence the catchment's hydrologic cycle. Lumped models are capable of accurate hydrologic simulation across a variety of scales. Notably, lumped models are utilized by the Iowa Flood Center and National Weather Service River Forecast Centers.

Distributed hydrologic models are capable of accounting for spatial heterogeneity, but require a set of parameters for each and every control volume. An enormous amount of observations describing each hydrologic function would be required to accurately calibrate these parameters for an entire region (Sawicz, Wagener, Sivapalan, Troch, & Carrillo, 2011). Lacking accurate measurement of hydrologic function across the watershed of interest, some distributed models are calibrated using only the outlet hydrograph. The many degrees of freedom for each set of parameters can affect the same outcome in similar ways. Thusly, it is possible to get lost in a fog of calibration, wondering if the distributed model results are right for the wrong reasons when multiple errors effectively compensate for each other (Ebel & Loague, 2006).

Perhaps the unique challenges presented by both lumped and distributed hydrologic would be overcome if calibration methods could be improved to the extent that a singular optimal solution is achieved for each area and time of interest. Still, optimal parameter calibration to reach this optimal solution is only possible for a perfectly organized model that is build using error-free measurements of watershed characteristics. Even so, parameter calibration using historical data relies on an assumption of stationarity, which is ill-fitting in a world affected by climate change, urbanization, and land cover modification (Falkenmark et al., 2008). I avoided model calibration by choosing parameters that describe hydrologic characteristics and processes at the hillslope scales. Each parameter was based on measurable physical properties that could be reasonably obtained for watersheds across the world.

2.3 Satellite Remote Sensing of Land Surface Hydrology

The study of land surface hydrology using remote sensing techniques has advanced greatly since the launch of the U.S. National Aeronautics and Space Administration (NASA) Earth Observing System (EOS). Precipitation is the primary driver of the land hydrological cycle, and great advances have been made to accurately estimate precipitation using visible, infrared, and microwave technology aboard satellites (Tang, Gao, Lu, & Lettenmaier, 2009). Visible and infrared sensors were the first technologies used to estimate rainfall from satellites (Petty & Krajewski, 2010). Visible and infrared sensors do not directly measure precipitation due to the presence of clouds. Instead, precipitation is inferred from cloud top brightness temperature. However, microwave signals directly interact with precipitation particles and are much less sensitive to cloud cover. Early satellite retrievals of precipitation over land were gathered by the Special Sensory Microwave Imager (SSM/I) aboard the Defense Meteorological

Satellite Program (DMSP) platforms, TRMM Microwave Imager (TMI) aboard the Tropical Rainfall Measuring Mission (TRMM) satellite, and Advanced Microwave Scanning Radiometer-EOS (ASMR-E) aboard the EOS Aqua Satellite (Dinku & Anagnostou, 2005; Grecu, Olson, & Anagnostou, 2004; Kummerow et al., 2001; Prabhakara, Iacovazzi, & Yoo, 2004; Spencer, Goodman, & Hood, 1988; G. L. Stephens & Kummerow, 2007). New active microwave sensors (radar) provide direct estimates of the vertical distribution of precipitation. TRMM offered the first spaced-based precipitation radar estimates and its successor, the Global Precipitation Measurement (GPM) mission provides near-global coverage. Though visible, infrared, and microwave sensors have their own limitations, algorithms that utilize their intercalibration can generate rainfall estimates at high spatiotemporal resolution. Algorithms like Precipitation Estimation from Remotely Sensed Information using Artificial Neural Networks (PERSIANN) and Integrated Multi-Satellite Retrievals for GPM (IMERG) that use intermittent coverage of rain rates provided by constellations of earth-orbiting satellites alongside retrievals from geosynchronous satellites represent the furthest advancement of satellite precipitation estimation (Huffman et al., 2009, 2018).

After precipitation, evapotranspiration (ET) is the second largest component of the land surface water cycle. While remote sensing methods cannot measure ET directly, a number of advancements have been made to estimate ET using satellite observations of surface energy flux and vegetation. Early efforts to estimate ET relied on ground measurement of surface temperature and vegetation indices (Jackson, Reginato, & Idso, 1977). Satellite observations of global surface albedo, emissivity, reflectance, and land cover supplement this information to track the surface energy balance (Wan, Zhang, Zhang, & Li, 2004). Several algorithms have inferred latent heat flux from this balance to map ET regionally (Allen et al., 2005; Allen et al., 2007; Bastiaanssen et al., 1998). The latest advanced ET algorithms use the Penman-Monteith equation with remote sensing data as primary inputs, but must rely on some in-situ data that cannot be measured by satellites (Cleugh, Leuning, Mu, & Running, 2007; Mu, Zhao, & Running, 2013). A common sensor used by these algorithms is the Moderate Resolution Imaging Spectroradiometer (MODIS) launched aboard the NASA Terra and Aqua satellites in 1999 and 2002, respectively.

Satellite remote sensing data will be most valuable to communities in data scarce regions. Consider that the NWS currently operates 159 of Next-Generation Radar (NEXRAD) systems. The network has been upgraded during its 27 years of operation to improve resolution and include dual polarization technology. Satellite estimates of rainfall provide little benefit to areas covered by the radar network. But, they can play a critical role in developing countries lacking dense, large-scale networks of weather radar or raingages. The utility of satellite remote sensing products providing flood data is magnified in developing countries because their communities are most vulnerable to flood-related natural disasters (Few, 2003; Schanze, Zeman, & Marsalek, 2006).

2.4 Flash Flood Guidance System

Recognizing that floods have a particularly disastrous impact on lives and properties of the affected populations, the 15th WMO Congress approved the implementation of a Flash Flood Guidance System project with global coverage. Is was developed by the WMO Commission for Hydrology (CHy) jointly with the WMO Commission for Basic Systems (CBS) and in collaboration with the US National Weather Service, the Hydrologic Research Center, and the United States Agency for International Development Office of U.S. Foreign Disaster Assistance

(USAID/OFDA). This system focuses on flash floods because they are among the world's deadliest natural disasters, causing more than 5,000 lives to be lost annually. Flash floods have the highest mortality rate among different classes of flooding, causing the highest number of deaths per person affected (World Meteorological Organization, 2016). The Hydrologic Research Center has implemented regional Flash Flood Guidance Systems in the following 12 regions in cooperation with the national meteorological and hydrological services within them: Black Sea and Middle East, Central Asia, Central America, Haiti and Dominican Republic, Mekong River, Myanmar, Northwest South America, South America, Southeast Asia, Southeastern Asia-Oceania, and South East Europe (World Meteorological Organization, 2016b, 2016c, 2017a, 2017b, 2017c, 2018a, 2018b, 2018c, 2018d).

Important technical elements of the Flash Flood Guidance System are the development and use of high-resolution numerical weather prediction model outputs, bias-corrected satellite precipitation estimate field, and physically-based hydrological modelling to determine flood risk on a catchment scale. The latter two elements of the FFGS are shared in common with the research approach presented here. In addition, small basins are delineated for each regional FFGS using global digital terrain elevation databases, relying on satellite topography measurements where land surveys and LiDAR information is unavailable.

Notably, the real-time satellite precipitation estimates that drive the regional systems are specialized products provided by NOAA and the WMO. These products are shared with each regional FFGS in discrete time windows to provide the highest quality data available as soon as possible. As such, satellite precipitation estimates continue to improve for time *t* as additional satellite observations pass the area of interest later. Each regional FFGS is built to estimate rainfall first from passive microwave and infrared-based satellite observations. Unlike this research, radar and gauge data is used both to bias-correct these satellite estimates on a seasonal basis and to provide supplementary observations of rainfall.

The backbone of the FFGS models built and operated by the HRC is its threshold-runoff (Thresh-R) component (Ntelekos, Georgakakos, & Krajewski, 2006). Thresh-R is a computation of the amount of effective rainfall of a given duration that is capable of causing minor flooding, identified by causing bankfull conditions at the catchment outlet. Sacramento Soil Moisture Accounting Model (SACSMA) is used to forecast the generation of runoff that certain rainfall volumes would create over given durations. Thresh-R values are calculated at each basin and compared to SACSMA scenarios via rainfall-runoff curves produced for specific time interval and initial soil moisture conditions. Runoff values equal to Thresh-R for each scenario are termed flash flood guidance (FFG) values. Therefore, evaluation of FFG informs national meteorological and hydrological services about flash flood risk by providing an estimate of the precipitation amount that would generate bankfull discharge at the outlets of small, flash flood prone basins throughout their country. Local experts integrate local knowledge to validate the guidance and issue a warning through channels appropriate to each country as necessary (World Meteorological Organization, 2016).

Though the modelling approach of FFGS is very different from this research, it is motivated by the same challenge- predicting floods everywhere. The operation of FFGS to benefit global populations is impressive for its technical capabilities. Moreover, the WMO and HRC has demonstrated an outstanding ability to bridge the gap between scientific research and real-world application benefiting a diverse set of stakeholders. The FFGS serves as a proof that satellite remote sensing techniques can effectively be used to predict floods.

CHAPTER 3: PUERTO RICO

3.1 Introduction

The Estado Libre Asociado de Puerto Rico has commonwealth status within the United States federal system. Its per capita income of $18,626 in 2015 places it below the lowest category for US states and in the middle income group internationally. Both Puerto Rico's rural and urban population are highly vulnerable to floods. But, the island is well gaged by hydro-meteorological services, making it a suitable study area for this research (Azar & Rain, 2007).

3.2 Hydro-meteorology of Puerto Rico

Puerto Rico is the smallest island of the Greater Antilles, a grouping of islands that constitute 90% of the land mass of the mountainous islands that stretch from south of Florida to Venezuela. It is bounded by the Atlantic Ocean to the north and the Caribbean Sea to the south. The principal topographic feature of the island is the Cordillera Central, an east-west mountain range with peak elevations commonly ranging from 3,000 to 4,000 feet above sea level. The Cordillera Central divides the island into a northern two-thirds and a southern one-third, forming the principal drainage divide of the larger streams (López, Colón-Dieppa, & Cobb, 1979; López & Fields, 1970).

Nearly 70 non-navigable rivers and streams originate in the Cordillera Central. These rivers are narrow, shallow, and generally less than 30 km long, making them susceptible to over-bank floods and flash floods. Flash floods typically result from rainfall that is intense in the upper basins but is sparse or nonexistent on the coast (Ramos-Gines, 1999). Streams on the south coast are more susceptible to flash floods than those on the north coast because of their shorter length and steeper upper basin gradients. Average stream length and slope are 35 kilometers (km) and 25 meters per kilometer (m/km), respectively, on the north side of the island and 23 km and 45 m/km on the south coast (Puerto Rico Department of Natural Resources, 1980).

Figure 1 and Figure 2 illustrate the width function histogram and width function map of Puerto Rico rivers, respectively. All 51 watersheds defined by the National Hydrography Dataset Plus (NHD+) on the main island of Puerto Rico with outlets draining to the Atlantic Ocean and Caribbean Sea are included (Moore & Dewald, 2016). The width function is defined as the distribution of the distances from any point in a watershed to its outlet (Kirkby, 1976). Half of the streams on the main island of Puerto Rico are located 25 km or less from ocean outlets, demonstrating that streams often respond quickly to rainfall on the main island of Puerto Rico.

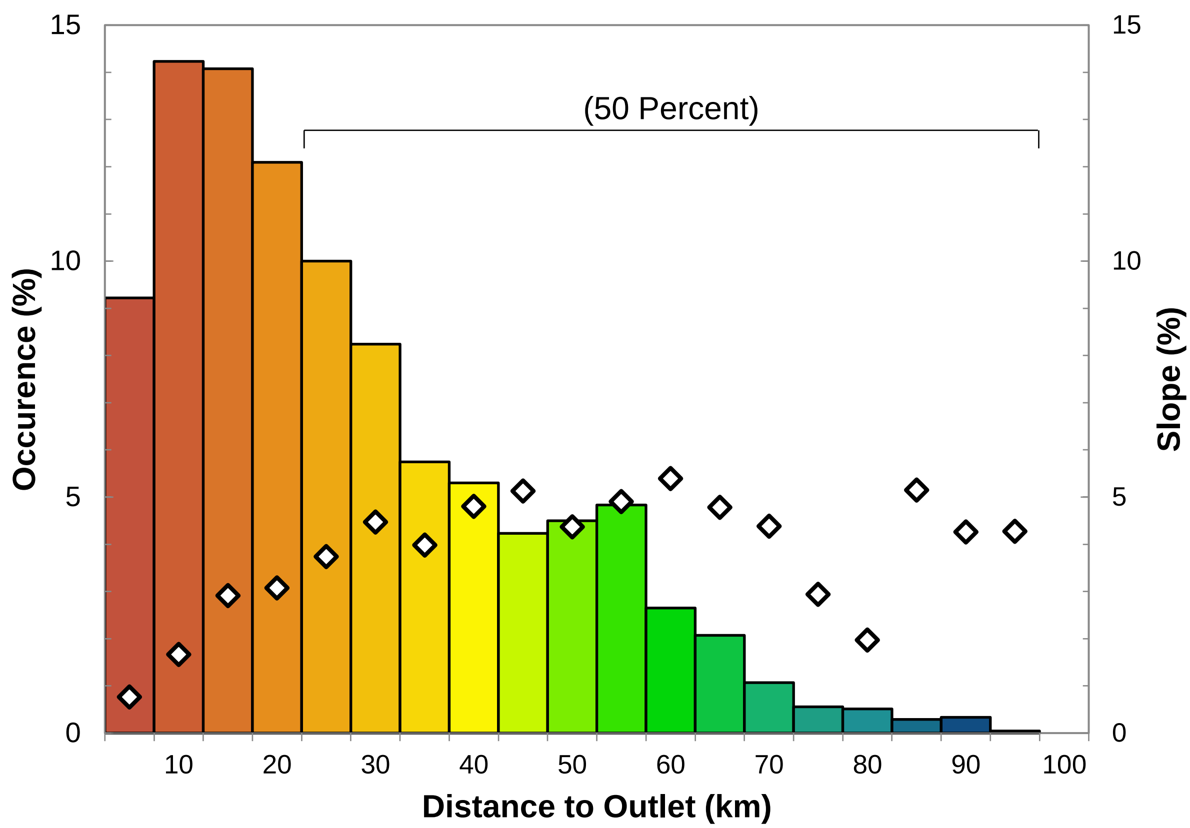

Figure 1: Histogram of width function distribution and average slope of links within each bin for all streams within watersheds defined by NHD+ (Moore & Dewald, 2016).

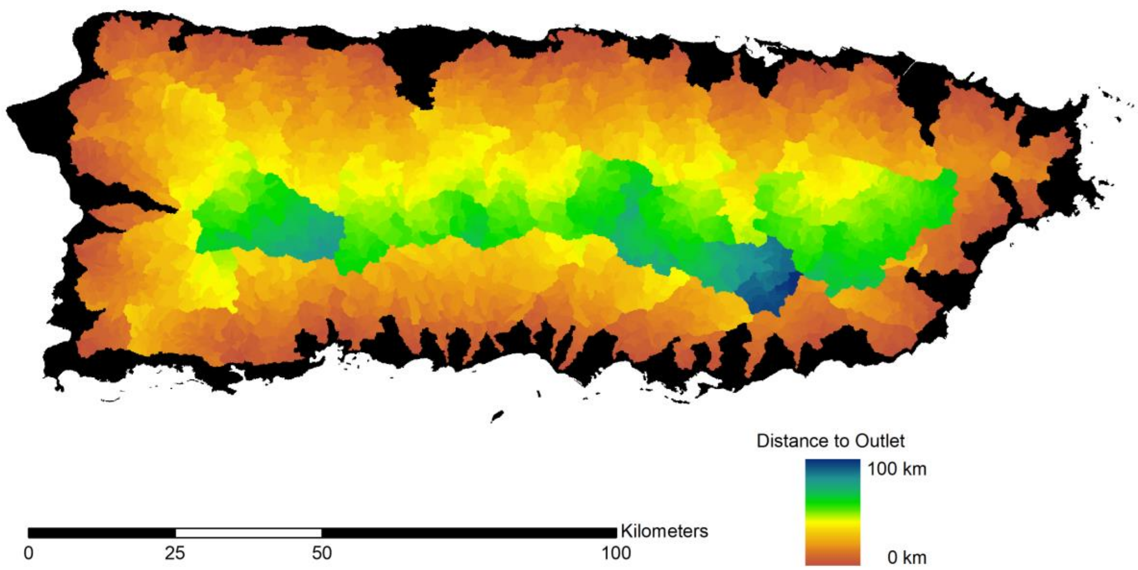

Figure 2: Map of width function distribution for all streams within watersheds defined by NDH+ (Moore & Dewald, 2016).

Puerto Rico has a tropical marine climate. Rain-producing weather systems generally move over the island from the east during June 1 to November 30 (hurricane season), and from the northwest during December to May. In the hurricane season, the dominating weather systems are tropical waves that develop in the trade-wind current, and upper-atmospheric troughs or cyclones in the tropical belt. During December to May, the weather-producing systems are frontal systems and low-pressure troughs (Ramos-Gines, 1999). Tropical cyclones play a central role in the hydrology of extreme floods in Puerto Rico and many of the record flood peak measurements in Puerto Rico were associated with tropical cyclones, most notably Hurricane Donna on 6 September, 1960; Hurricane Hortense on 10 September, 1996; Hurricane Georges on 21- 22, September 1998; and Hurricane Maria on September 20, 2017. The interior mountain region of Puerto Rico produces some of the largest unit discharge flood peaks in the United States. Orographic mechanisms play a major role in amplifying rainfall accumulations in these mountainous regions, relative to open ocean rainfall (Smith, Paula, & Baeck, 2005).

3.3 Puerto Rico Study Area: Characteristics and Available Data

To compare model simulations of streamflow across the main island of Puerto Rico to measured values, the systematic record and historic data for existing and continued gaging sites on the island were obtained from the USGS database. By 2019, the USGS reported data from 108 active gaging sites operated and maintained by the Junta de Calidad Ambiental (JCA), Autoridad de Energía Eléctrica de Puerto Rico (AEEPR), Autoridad de Acueductos y Alcantarillado de Puerto Rico (AAAPR), and United States Army Corps of Engineers (USACE). However, many stream gages exclusively reported water elevation or monitored manmade canals in urban areas and were excluded from this study. Only those watersheds with time series of streamflow in natural channels recorded after March 2014 were included. Model simulations are driven by satellite remote sensing data that became available in March 2014.

In total, 75 streamgage stations were included, and their corresponding upstream watersheds comprise the study area of this research. Figure 3 shows the location of each watershed and its outlet to the major rivers on the main island of Puerto Rico. All 75 watersheds were modelled, of which 44 had 25 years or more of daily streamflow record. Figure 4 shows a timeline of streamflow records at the 75 gaging sites for both daily and near real time data. Some of the 75 watersheds contain streamflow regulation structures like dams and reservoirs. Model performance within regulated watersheds was evaluated separately.

Hydrologic and climatic basin characteristics were computed using GIS software. The characteristics were determined by digitizing historic maps or measuring digital coverages and overlays of terrain features, drainage basin properties, mean annual rainfall, 2-, 5-, 10-, 25-, 50-, and 100-year 24-hour rainfall intensity contours, and soil properties. The studied characteristics are listed below and a summary of all included hydrologic and climatic basin characteristics is presented in Table 1 and Table 2, respectively. In addition, a statistical summary of these characteristics is presented in Table 3.

TDA: total drainage area measured up to the gaging site, in square kilometers: the total area of land whose runoff flows to the gaging site.

DR: depth-to-rock, in meters: the basin average value of the maximum soil depth. Values were obtained from six regional United States Natural Resources Conservation Services (USNRCS) soil survey reports (Acevedo, 1982; Boccheciamp, 1977, 1978; Carter, 1965; Gierbolini, 1975, 1979).

CS: channel slope, in percent: the average slope of channels within the basin.

CL: channel length, in kilometers: the distance along the stream from the gaging site to the drainage-basin divide along the longest channel.

PF: peak flow with 10-year return period, in cubic meters per second: the flowrate at the watershed outlet with a probability of exceedance equaling 0.10. Values were calculated using USGS Bulletin 17B (B17B) procedures within USGS PeakFQ software (Flynn, Kirby, & Hummel, 2006; U.S. Interagency Advisory Committee on Water Data, 1982).

MAR: mean annual rainfall, in millimeters: the basin average total accumulated depth of annual. Values were interpolated from 30-year climate normals provided by the National Oceanic and Atmospheric Administration (NOAA) National Climatic Data Center (NCDC) at 51 weather stations located across the main island of Puerto Rico.

RI-*i*: depth of rainfall accumulation during *i*-year 24-hour storm, in millimeters: the basin average rainfall depth of a storm lasting 24 hours for a return period of 1, 2, 5, 10, 25, 50, or 100 years. Values were calculated using NOAA Atlas 14 Volume 3 precipitation-frequency estimates (Bonnin et al., 2006).

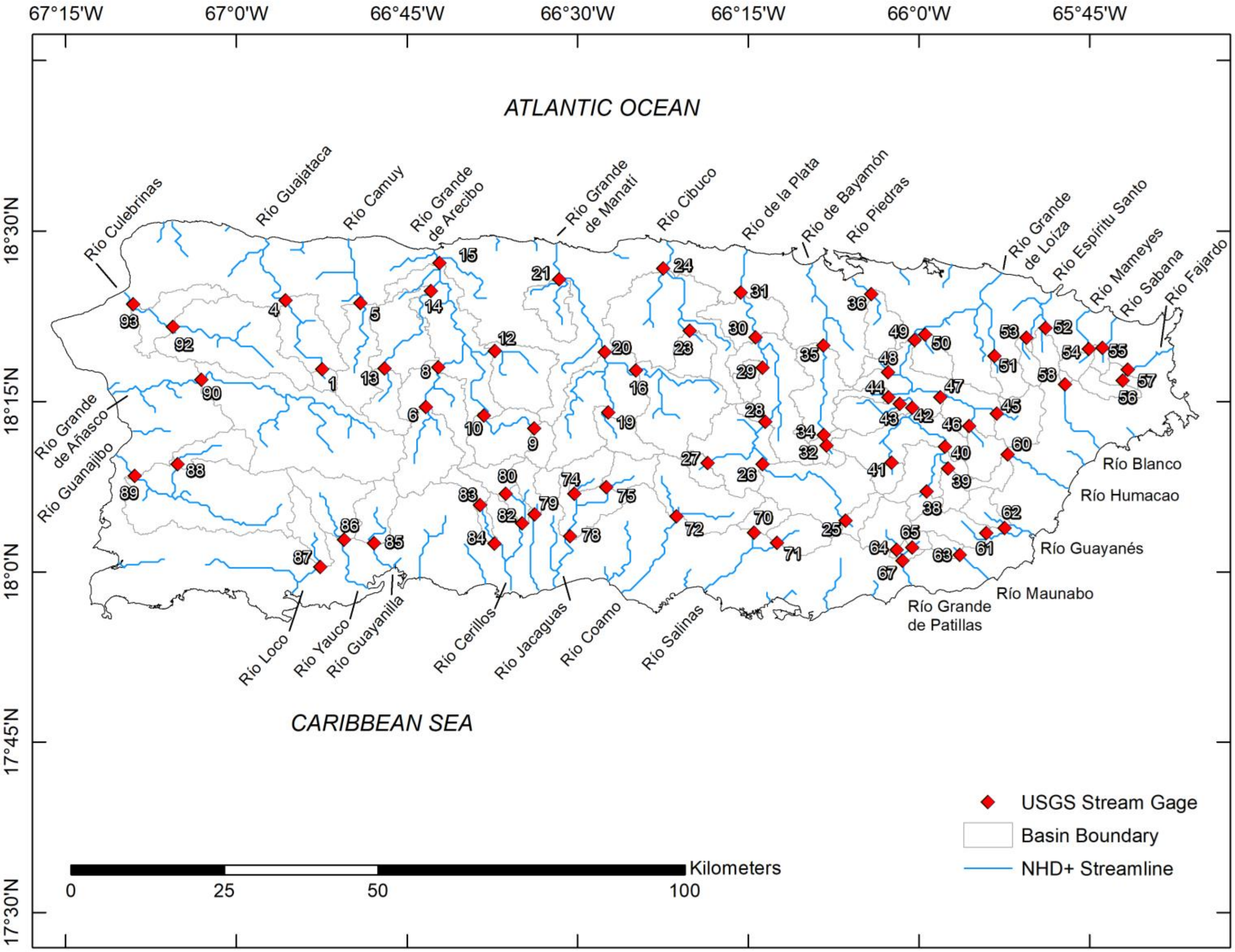

Figure 3: Locations of 75 modelled watersheds and the USGS streamgages at their outlets, numbered by Study Index as listed in Table 1. Streams provided by National Hydrography Dataset Plus (Moore & Dewald, 2016).

Table 1: Hydrologic characteristics of 75 modelled watersheds in Puerto Rico

[*Study Index*, identifier of each gage, created for this study; *USGS Streamgage*, identifier for USGS each streamgage station located at basin outlet; *Site Name*, name describing USGS streamgage station; *Type*, identifier for data recorded by USGS streamgage station (R = rainfall, S = streamflow); *Lat.*, decimal latitude of watershed outlet with NAD83 datum; *Lon.*, decimal longitude of watershed outlet with NAD83 datum; *Years of Record*, number of full years of streamflow record; *Period of Record*, timeline of streamflow record availability; *TDA*, total drainage area; *DR*, depth-to-rock; *CS*, channel slope; *CL*, channel length; *PF*, 10-yr peak flow]

Study Index	USGS Streamgage	Site Name	Type	Lat.	Lon.	Years of Record	Period of Record	TDA (km^2)	DR (m)	CS (%)	CL (km)	PF (m^3/s)
1	50010500	Río Guajataca at Lares	R, S	18.297	-66.873	1	2017-'19	8.2	1.35	4.1	3.0	N/A[3]
4	50011200	Río Guajataca below Lago Guajataca	S	18.398	-66.927	32	1986-'19	98.1	1.28	1.5	20.6	N/A[1]
5	50014800	Río Camuy near Bayaney	R, S	18.394	-66.818	29	1989-'19	83.1	1.34	2.4	23.0	179
6	50021700	Río Grande de Arecibo above Utuado	S	18.242	-66.722	20	1998-'19	93.2	1.36	5.0	19.1	N/A[1,2]
8	50024950	Río Grande de Arecibo below Utuado	S	18.300	-66.704	22	1996-'19	169.9	1.38	4.6	27.7	N/A[1]
9	50025155	Río Saliente at Coabey near Jayuyu	S	18.211	-66.563	30	1988-'19	24.0	1.15	8.8	7.2	245
10	50026025	Río Caonillas at Paso Palma	R, S	18.229	-66.637	23	1995-'19	98.4	1.21	5.4	22.5	560
12	50027000	Río Limon above Lago Dos Bocas	R, S	18.324	-66.621	19	1999-'19	86.0	1.24	4.4	17.3	533
13	50028000	Río Tanama near Utuado	R, S	18.299	-66.783	18	2000-'19	47.7	1.47	2.6	14.9	265
14	50028400	Río Tanama at Charco Hondo	S	18.412	-66.714	23	1995-'19	57.5	1.35	2.7	27.3	244
15	50029000	Río Grande de Arecibo at Central Cambalache	R, S	18.454	-66.702	22	1996-'19	518.0	1.31	3.9	59.5	N/A[1]
16	50031200	Río Grande de Manatí near Morovis	S	18.296	-66.414	30	1987-'17	143.2	1.30	4.9	32.5	769
19	50034000	Río Gauta near Orocovis	S	18.234	-66.454	29	1989-'19	43.3	1.11	8.5	14.3	285
20	50035000	Río Grande de Manatí at Ciales	R, S	18.322	-66.460	31	1987-'19	331.5	1.24	5.5	43.1	1583
21	50038100	Río Grande de Manatí at Highway 2 near Manatí	S	18.429	-66.526	29	1989-'19	510.2	1.22	2.7	12.3	2266
23	50038320	Río Cibuco below Corozal	S	18.354	-66.335	27	1989-'17	40.0	1.22	3.7	9.5	N/A[1]
24	50039500	Río Cibuco at Vega Baja	S	18.445	-66.374	29	1989-'19	256.7	1.16	2.1	36.4	532
25	50039995	Río Carité at spillway	R, S	18.075	-66.107	13	2005-'19	21.2	1.04	2.3	7.0	N/A[1]
26	50043000	Río de la Plata at Proyecto La Plata	R, S	18.158	-66.229	28	1986-'14	141.9	1.05	2.5	36.0	N/A[1]
27	50043197	Río Usabón at Highway 162 near Barranquitas	R, S	18.160	-66.309	11	2007-'19	22.2	1.06	1.5	7.0	205
28	50043800	Río de la Plata at Comerio	R, S	18.220	-66.224	27	1991-'19	281.0	1.07	3.4	48.2	2180

Table 1 − Continued

Study Index	USGS Streamgage	Site Name	Type	Lat.	Lon.	Years of Record	Period of Record	TDA (km^2)	DR (m)	CS (%)	CL (km)	PF (m^3/s)
29	50044810	Río Guadiana near Guadiana	S	18.299	-66.228	17	2001-'19	20.9	1.08	5.3	8.5	242
30	50045010	Río de la Plata below La Plata damsite	S	18.344	-66.238	28	1990-'19	447.6	1.08	3.7	70.6	N/A[1]
31	50046000	Río de la Plata at Highway 2 near Toa Alta	R, S	18.410	-66.261	33	1985-'19	538.7	1.00	3.4	81.5	1717
32	50047535	Río de Bayamón at Arenas	R, S	18.167	-66.122	18	2000-'19	7.0	1.07	1.2	3.7	N/A[1]
34	50047560	Río de Bayamón below Lago de Cidra Dam	S	18.201	-66.139	28	1990-'19	21.5	1.05	0.4	5.5	N/A[1]
35	50047850	Río de Bayamón near Bayamón	R, S	18.332	-66.139	29	1989-'19	108.3	1.06	2.3	25.9	N/A[2]
36	50049100	Río Piedras at Hato Rey	R, S	18.408	-66.069	24	1994-'19	39.4	1.09	1.1	11.7	262
38	50050900	Río Grande de Loíza at Quebrada Arenas	S	18.118	-65.988	29	1989-'19	15.5	1.12	2.5	5.1	384
39	50051310	Río Cayaguas at Cerro Gordo	R, S	18.152	-65.956	29	1989-'19	26.2	1.01	1.2	10.0	354
40	50051800	Río Grande de Loíza at Highway 183 San Lorenzo	S	18.184	-65.961	28	1990-'19	106.4	0.97	2.3	15.9	791
41	50053025	Río Turabo above Borinquen	S	18.160	-66.040	28	1990-'19	18.5	1.07	6.0	5.4	158
42	50055000	Río Grande de Loíza at Caguas	S	18.241	-66.009	33	1985-'19	232.6	0.94	2.6	27.4	1313
43	50055225	Río Caguitas at Villa Blanca at Caguas	R, S	18.247	-66.027	28	1990-'19	43.0	0.96	2.9	13.9	362
44	50055380	Río Bairoa above Abiroa, Caguas	S	18.256	-66.044	16	2002-'19	12.3	0.98	2.4	7.7	90
45	50055750	Río Gurabo below El Mango	S	18.232	-65.885	28	1990-'19	57.8	1.01	2.2	10.4	308
46	50056400	Río Valenciano near Juncos	R, S	18.214	-65.926	29	1989-'19	38.0	0.91	1.7	10.6	603
47	50057000	Río Gurabo at Gurabo	S	18.256	-65.968	33	1985-'19	155.9	0.93	1.6	21.2	1409
48	50058350	Río Canas at Río Canas	S	18.293	-66.045	28	1990-'19	19.5	1.00	0.7	3.8	137
49	50059050	Río Grande de Loíza below Loíza damsite	R, S	18.340	-66.006	22	1996-'19	541.3	1.03	1.9	43.3	N/A[1]
50	50059210	Quebrada Grande at Barrio Dos Bocas	S	18.348	-65.990	6	2012-'19	33.4	1.06	2.7	7.7	N/A[3]
51	50061800	Río Canovanas near Campo Rico	R, S	18.316	-65.889	25	1993-'19	25.5	1.21	4.9	9.5	379
52	50063800	Río Espíritu Santo near Río Grande	R, S	18.358	-65.814	24	1994-'19	22.3	1.38	8.7	9.7	402
53	50064200	Río Grande near El Verde	R, S	18.343	-65.842	28	1990-'19	18.9	1.36	11.2	7.9	372
54	50065500	Río Mameyes near Sabana	S	18.327	-65.750	27	1991-'19	17.8	1.17	8.9	5.5	458
55	50067000	Río Sabana at Sabana	S	18.329	-65.731	27	1991-'19	10.3	1.50	5.5	3.0	201
56	50070900	Río Fajardo at Paraíso near Fajardo	R, S	18.281	-65.701	15	2003-'19	24.5	1.22	2.5	8.8	N/A[2]
57	50071000	Río Fajardo near Fajardo	S	18.297	-65.693	29	1989-'19	38.6	1.20	2.1	11.1	409

Table 1 − Continued

Study Index	USGS Streamgage	Site Name	Type	Lat.	Lon.	Years of Record	Period of Record	TDA (km^2)	DR (m)	CS (%)	CL (km)	PF (m^3/s)
58	50075000	Río Icacos near Naguabo	R, S	18.275	-65.785	26	1992-'19	3.3	1.44	0.9	1.0	51
60	50081000	Río Humacao at Las Piedras	S	18.172	-65.869	29	1989-'19	17.2	0.89	2.3	12.6	352
61	50083500	Río Guayanés near Yabucoa	R, S	18.057	-65.901	16	2002-'19	44.5	0.80	3.4	13.8	193
62	50085100	Río Guayanés at Central Roig	S	18.064	-65.874	12	2006-'19	68.9	0.81	2.2	9.6	95
63	50090500	Río Maunabo at Lizas	R, S	18.025	-65.940	27	1991-'19	13.9	0.73	3.1	5.5	192
64	50092000	Río Grande de Patillas near Patillas	R, S	18.032	-66.032	29	1989-'19	47.4	0.88	8.0	11.6	407
65	50093000	Río Marín near Patillas	S	18.036	-66.009	18	2000-'19	11.5	0.88	6.6	2.4	107
67	50093120	Río Grande de Patillas below Lago Patillas	S	18.016	-66.024	13	2005-'19	66.5	0.87	7.3	14.5	N/A[1]
70	50100200	Río Lapa near Rabo del Buey	S	18.058	-66.241	19	1999-'19	25.7	1.04	6.8	6.3	N/A[2]
71	50100450	Río Majada at la Plena	S	18.043	-66.207	21	1997-'19	43.3	1.01	5.0	10.0	N/A[1]
72	50106100	Río Coamo at Highway 14 at Coamo	R, S	18.082	-66.354	31	1987-'19	112.7	1.08	3.6	17.2	430
74	50110650	Río Jacaguas above Lago Guayabal	S	18.115	-66.504	6	2012-'19	35.6	1.19	9.5	10.2	N/A[3]
75	50110900	Río Toa Vaca above Lago Toa Vaca	S	18.125	-66.457	28	1990-'19	36.8	1.16	7.9	12.6	190
78	50111500	Río Jacaguas at Juana Díaz	R, S	18.052	-66.511	28	1990-'19	129.0	1.19	6.0	28.4	N/A[2]
79	50112500	Río Inabón at Real Abajo	R, S	18.084	-66.563	29	1989-'19	25.1	1.22	10.6	10.1	107
80	50113800	Río Cerrillos above Lago Cerrillos near Ponce	R, S	18.115	-66.605	28	1990-'19	30.8	1.13	7.4	7.5	208
82	50114000	Río Cerrillos below Lago Cerrillos near Ponce	S	18.071	-66.581	27	1991-'19	46.1	1.05	5.3	14.8	N/A[1]
83	50114900	Río Portugues near Tibes	R, S	18.098	-66.642	21	1997-'19	18.8	1.13	6.2	7.8	83
84	50115240	Río Portugues at Parque Ceremonial Tibes	R, S	18.042	-66.621	5	2013-'19	31.1	1.09	6.4	16.4	N/A[3]
85	50124200	Río Guayanilla near Guayanilla	R, S	18.042	-66.798	29	1989-'19	49.0	1.20	5.3	15.0	279
86	50126150	Río Yauco above Diversión Monserrate near Yauco	R, S	18.047	-66.841	16	2002-'19	70.4	1.22	3.9	17.2	N/A[1]
87	50129254	Río Loco at Las Latas near La Joya near Guanica	S	18.007	-66.876	11	2007-'19	42.0	1.22	3.0	15.4	N/A[2]
88	50136400	Río Rosario near Hormigueros	R, S	18.158	-67.085	28	1990-'19	50.0	1.05	3.2	17.9	215
89	50138000	Río Guanajibo near Hormigueros	R, S	18.141	-67.148	30	1988-'19	310.8	0.90	1.9	39.4	716
90	50144000	Río Grande de Añasco near San Sebastián	R, S	18.282	-67.051	29	1989-'19	244.2	1.32	3.8	54.1	1306
92	50147800	Río Culebrinas at Highway 404 near Moca	R, S	18.360	-67.092	28	1990-'19	184.4	1.36	1.7	29.0	1021
93	50148890	Río Culebrinas at Margarita damsite near Aguada	S	18.393	-67.151	20	1998-'19	245.0	1.30	1.5	38.9	133

[1] Known effect of flow regulation upstream, [2] Known effect of urbanization occurring during period of record, [3] Period of record of peak flows shorter than ten years

Table 2: Climatic characteristics of 75 modelled watersheds in Puerto Rico

[*Study Index*, numerical identifier of each gage, created for this study; *USGS Streamgage*, numerical identifier for USGS each streamgage station located at basin outlet; *Site Name*, name describing USGS streamgage station; *Type*, identifier for data recorded by USGS streamgage station (R = rainfall, S = streamflow); *Lat.*, decimal latitude of watershed outlet with NAD83 datum; *Lon.*, decimal longitude of watershed outlet with NAD83 datum; *MAR*, mean annual rainfall; *RI-1*, 1-yr 24-hour rainfall intensity; *RI-2*, 2-yr 24-hour rainfall intensity; *RI-5*, 5-yr 24-hour rainfall intensity; *RI-10*, 10-yr 24-hour rainfall intensity; *RI-25*, 25-yr 24-hour rainfall intensity; *RI-50*, 50-yr 24-hour rainfall intensity; *RI-100*, 100-yr 24-hour rainfall intensity]

Study Index	USGS Streamgage	Site Name	Type	Lat.	Lon.	MAR (mm)	RI-1 (mm)	RI-2 (mm)	RI-5 (mm)	RI-10 (mm)	RI-25 (mm)	RI-50 (mm)	RI-100 (mm)
1	50010500	Río Guajataca at Lares	R, S	18.297	-66.873	1917	98	124	162	195	246	290	340
4	50011200	Río Guajataca below Lago Guajataca	S	18.398	-66.927	1920	101	126	153	176	210	237	267
5	50014800	Río Camuy near Bayaney	R, S	18.394	-66.818	1954	103	131	165	197	243	282	325
6	50021700	Río Grande de Arecibo above Utuado	S	18.242	-66.722	1911	100	127	170	210	272	325	384
8	50024950	Río Grande de Arecibo below Utuado	S	18.300	-66.704	1939	103	131	170	206	262	310	363
9	50025155	Río Saliente at Coabey near Jayuyu	S	18.211	-66.563	2240	111	144	200	254	343	422	511
10	50026025	Río Caonillas at Paso Palma	R, S	18.229	-66.637	2088	107	137	187	234	310	376	450
12	50027000	Río Limon above Lago Dos Bocas	R, S	18.324	-66.621	2001	105	133	174	212	272	323	378
13	50028000	Río Tanama near Utuado	R, S	18.299	-66.783	1949	107	137	179	218	279	333	394
14	50028400	Río Tanama at Charco Hondo	S	18.412	-66.714	2030	91	116	148	176	214	245	279
15	50029000	Río Grande de Arecibo at Central Cambalache	R, S	18.454	-66.702	1997	87	111	141	166	199	226	253
16	50031200	Río Grande de Manatí near Morovis	S	18.296	-66.414	1885	110	143	194	238	302	358	417
19	50034000	Río Gauta near Orocovis	S	18.234	-66.454	1985	100	131	182	228	297	358	424
20	50035000	Río Grande de Manatí at Ciales	R, S	18.322	-66.460	1973	108	140	189	232	297	351	411
21	50038100	Río Grande de Manatí at Highway 2 near Manatí	S	18.429	-66.526	1733	96	124	163	196	242	282	320
23	50038320	Río Cibuco below Corozal	S	18.354	-66.335	1927	110	143	191	231	287	333	381
24	50039500	Río Cibuco at Vega Baja	S	18.445	-66.374	1876	98	127	168	202	248	284	325
25	50039995	Río Carité at spillway	R, S	18.075	-66.107	1745	107	141	201	253	328	394	462
26	50043000	Río de la Plata at Proyecto La Plata	R, S	18.158	-66.229	1667	103	137	192	240	310	368	432
27	50043197	Río Usabón at Highway 162 near Barranquitas	R, S	18.160	-66.309	1639	92	122	171	212	272	320	373
28	50043800	Río de la Plata at Comerio	R, S	18.220	-66.224	1659	99	130	181	223	282	333	386

Table 2 – Continued

Study Index	USGS Streamgage	Site Name	Type	Lat.	Lon.	MAR (mm)	RI-1 (mm)	RI-2 (mm)	RI-5 (mm)	RI-10 (mm)	RI-25 (mm)	RI-50 (mm)	RI-100 (mm)
28	50043800	Río de la Plata at Comerio	R, S	18.220	-66.224	1659	99	130	181	223	282	333	386
29	50044810	Río Guadiana near Guadiana	S	18.299	-66.228	1834	104	136	184	224	282	328	378
30	50045010	Río de la Plata below La Plata damsite	S	18.344	-66.238	1695	106	138	184	223	279	323	371
31	50046000	Río de la Plata at Highway 2 near Toa Alta	R, S	18.410	-66.261	1711	103	134	179	215	267	307	353
32	50047535	Río de Bayamón at Arenas	R, S	18.167	-66.122	1674	105	139	197	247	320	384	452
34	50047560	Río de Bayamón below Lago de Cidra Dam	S	18.201	-66.139	1671	105	138	195	245	318	378	445
35	50047850	Río de Bayamón near Bayamón	R, S	18.332	-66.139	1735	98	128	175	214	269	318	366
36	50049100	Río Piedras at Hato Rey	R, S	18.408	-66.069	1781	91	118	157	189	232	267	302
38	50050900	Río Grande de Loíza at Quebrada Arenas	S	18.118	-65.988	2023	122	163	231	292	381	460	544
39	50051310	Río Cayaguas at Cerro Gordo	R, S	18.152	-65.956	2245	121	161	228	287	376	452	536
40	50051800	Río Grande de Loíza at Highway 183 San Lorenzo	S	18.184	-65.961	2154	107	142	200	250	323	384	450
41	50053025	Río Turabo above Borinquen	S	18.160	-66.040	1867	104	138	195	244	318	376	442
42	50055000	Río Grande de Loíza at Caguas	S	18.241	-66.009	1995	97	128	180	224	287	343	399
43	50055225	Río Caguitas at Villa Blanca at Caguas	R, S	18.247	-66.027	1763	95	125	176	219	282	333	389
44	50055380	Río Bairoa bove Abiroa, Caguas	S	18.256	-66.044	1770	94	124	174	216	277	328	381
45	50055750	Río Gurabo below El Mango	S	18.232	-65.885	2100	110	146	206	257	330	391	455
46	50056400	Río Valenciano near Juncos	R, S	18.214	-65.926	2030	107	142	200	250	320	381	445
47	50057000	Río Gurabo at Gurabo	S	18.256	-65.968	1975	100	132	186	231	297	353	411
48	50058350	Río Canas at Río Canas	S	18.293	-66.045	1774	102	134	186	230	295	348	406
49	50059050	Río Grande de Loíza below Loíza damsite	R, S	18.340	-66.006	1920	108	141	191	233	292	340	394
50	50059210	Quebrada Grande at Barrio Dos Bocas	S	18.348	-65.990	1791	105	138	188	229	287	338	389
51	50061800	Río Canovanas near Campo Rico	R, S	18.316	-65.889	2007	115	152	212	262	335	396	462
52	50063800	Río Espíritu Santo near Río Grande	R, S	18.358	-65.814	2133	106	141	198	247	318	373	437
53	50064200	Río Grande near El Verde	R, S	18.343	-65.842	2117	115	152	213	264	340	404	472
54	50065500	Río Mameyes near Sabana	S	18.327	-65.750	2273	117	155	218	272	348	414	483
55	50067000	Río Sabana at Sabana	S	18.329	-65.731	2209	116	153	214	267	340	404	472
56	50070900	Río Fajardo at Paraíso near Fajardo	R, S	18.281	-65.701	2378	120	158	222	277	358	424	498
57	50071000	Río Fajardo near Fajardo	S	18.297	-65.693	2325	117	154	215	267	343	406	475

Table 2 – Continued

Study Index	USGS Streamgage	Site Name	Type	Lat.	Lon.	MAR (mm)	RI-1 (mm)	RI-2 (mm)	RI-5 (mm)	RI-10 (mm)	RI-25 (mm)	RI-50 (mm)	RI-100 (mm)
58	50075000	Río Icacos near Naguabo	R, S	18.275	-65.785	2406	128	169	240	302	391	467	551
60	50081000	Río Humacao at Las Piedras	S	18.172	-65.869	2098	121	161	227	284	368	439	518
61	50083500	Río Guayanés near Yabucoa	R, S	18.057	-65.901	1983	112	148	210	264	343	409	483
62	50085100	Río Guayanés at Central Roig	S	18.064	-65.874	2083	110	146	207	262	340	406	480
63	50090500	Río Maunabo at Lizas	R, S	18.025	-65.940	1891	107	142	201	252	328	391	460
64	50092000	Río Grande de Patillas near Patillas	R, S	18.032	-66.032	1744	96	128	181	226	292	348	409
65	50093000	Río Marín near Patillas	S	18.036	-66.009	1809	98	130	184	229	295	351	409
67	50093120	Río Grande de Patillas below Lago Patillas	S	18.016	-66.024	1744	97	128	182	228	295	351	409
70	50100200	Río Lapa near Rabo del Buey	S	18.058	-66.241	1558	98	130	185	231	300	356	419
71	50100450	Río Majada at la Plena	S	18.043	-66.207	1716	99	131	186	233	302	361	424
72	50106100	Río Coamo at Highway 14 at Coamo	R, S	18.082	-66.354	1576	99	131	186	234	307	368	434
74	50110650	Río Jacaguas above Lago Guayabal	S	18.115	-66.504	1943	106	139	198	252	338	414	498
75	50110900	Río Toa Vaca above Lago Toa Vaca	S	18.125	-66.457	1845	110	145	206	262	353	432	521
78	50111500	Río Jacaguas at Juana Díaz	R, S	18.052	-66.511	1726	93	124	177	223	292	351	414
79	50112500	Río Inabón at Real Abajo	R, S	18.084	-66.563	2114	108	142	203	259	348	429	518
80	50113800	Río Cerrillos above Lago Cerrillos near Ponce	R, S	18.115	-66.605	1924	119	155	222	287	389	483	587
82	50114000	Río Cerrillos below Lago Cerrillos near Ponce	S	18.071	-66.581	1877	108	142	204	262	351	429	521
83	50114900	Río Portugues near Tibes	R, S	18.098	-66.642	1750	126	166	237	307	422	526	645
84	50115240	Río Portugues at Parque Ceremonial Tibes	R, S	18.042	-66.621	1693	101	133	189	242	323	396	478
85	50124200	Río Guayanilla near Guayanilla	R, S	18.042	-66.798	1528	104	137	196	249	330	401	480
86	50126150	Río Yauco above Diversión Monserrate near Yauco	R, S	18.047	-66.841	1500	111	147	211	267	353	429	513
87	50129254	Río Loco at Las Latas near La Joya near Guanica	S	18.007	-66.876	1322	96	127	182	229	300	361	427
88	50136400	Río Rosario near Hormigueros	R, S	18.158	-67.085	1984	94	121	167	210	277	335	404
89	50138000	Río Guanajibo near Hormigueros	R, S	18.141	-67.148	1710	94	122	167	210	277	335	401
90	50144000	Río Grande de Añasco near San Sebastián	R, S	18.282	-67.051	1888	85	108	142	171	216	254	295
92	50147800	Río Culebrinas at Highway 404 near Moca	R, S	18.360	-67.092	1811	91	116	146	172	211	243	277
93	50148890	Río Culebrinas at Margarita damsite near Aguada	S	18.393	-67.151	1797	95	119	145	168	202	230	259

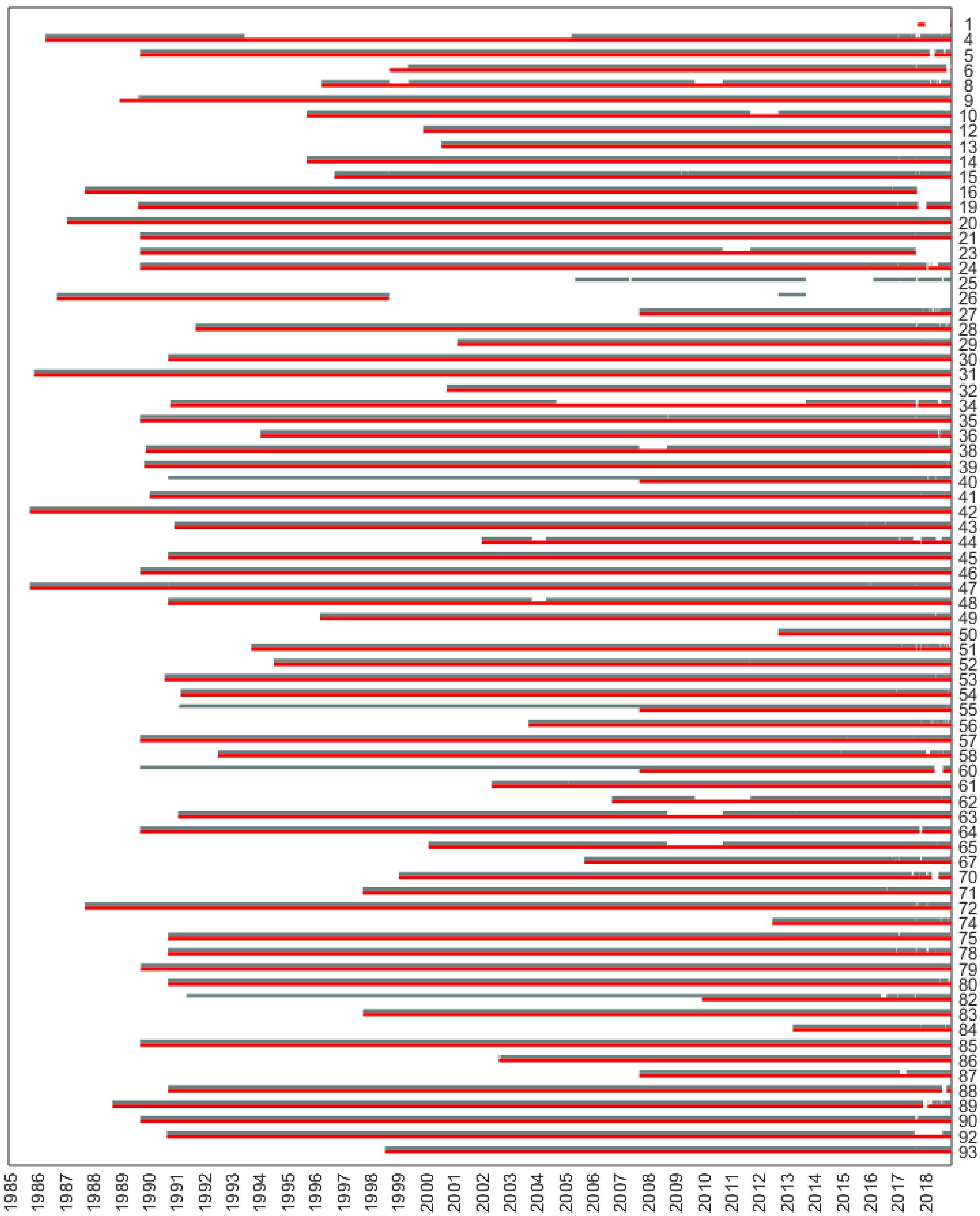

Figure 4: Timeline of streamflow record reported at 75 selected USGS monitoring stations, ordered by their Study Index. Both daily (grey) and near real time (red) records are shown.

Table 3: Statistical summary of hydrologic and climatic characteristics for 75 modelled watersheds in Puerto Rico

Basin Characteristic		Minimum	Maximum	Median	Mean	Standard Deviation
TDA	(km^2)	3.26	541.31	43.25	102.94	133.94
DR	(m)	0.73	1.50	1.11	1.13	0.17
CS	(%)	0.40	11.18	3.41	4.10	2.52
CL	(km)	0.99	81.47	12.60	18.30	15.92
PF	(m^3/s)	24.40	2265.91	322.25	498.75	510.87
MAR	(mm)	1321.82	2406.40	1890.78	1893.39	209.50
RI-1	(mm)	85.09	127.51	104.14	104.42	9.08
RI-2	(mm)	108.20	169.42	136.65	136.69	12.88
RI-5	(mm)	141.22	240.28	186.94	188.92	22.28
RI-10	(mm)	165.61	307.34	231.90	234.50	31.54
RI-25	(mm)	199.39	421.64	299.72	302.27	46.54
RI-50	(mm)	226.06	525.78	358.14	359.94	60.76
RI-100	(mm)	252.98	645.16	419.10	422.85	77.25

3.3.1 Local Hydrologic Data

As shown in Figure 4, the record for many active streamgages in Puerto Rico extends past 2 decades. While model analysis only necessitates the use of the most recent records, historical data allowed me to complete flood frequency analysis across the main island. Understanding historical peak flows has informed the modelling analysis detailed in Chapter 6.

The magnitude of 10-yr floods occurring at each streamgage site, listed in Table 1, was estimated using the USGS Bulletin 17B guidelines for determining flood flow frequency. Bulletin 17B recommends using the method-of-moments (MOM) to fit a Pearson type 3 (P3) distribution to the logarithms of the flood series, thereby yielding a log-Pearson type 3 (LP3) distribution to model observed streamflow data. Estimates of the mean, standard deviation, and skew coefficient of the logarithms of the sample data are computed using traditional moment estimators. However, because available at sites across the main island of Puerto Rico are mostly limited to less than 30 years, the skewness estimator is likely unstable (Stedinger & Griffis, 2008). In addition, the skew coefficient in LP3 analysis for short records is highly sensitive to extreme events. To address these issues, I weighted the at-site skew with a regional skewness estimator for two regions in Puerto Rico, where the recommended weights are inversely proportional to the precision of each estimator. While the average skew for the entire main island of Puerto Rico has been reported to be near zero, I have utilized published regional skew coefficients that divide the island into the North Coast-East Coast (NC-EC) and the South Coast-West Coast (SC-WC) skew regions (López et al., 1979; United States Water Resources Council, 1978). Figure 6 shows the location of each USGS streamgage station on the main rivers they monitor within each region.

A review of the 2,416 recorded annual maximum peak-discharges with known dates at the 75 modelled watersheds show that 72 percent of the peaks (1735 peaks) occurred during the 6-month-long hurricane season, June 1 to November 30 each year, as illustrated in Figure 5.

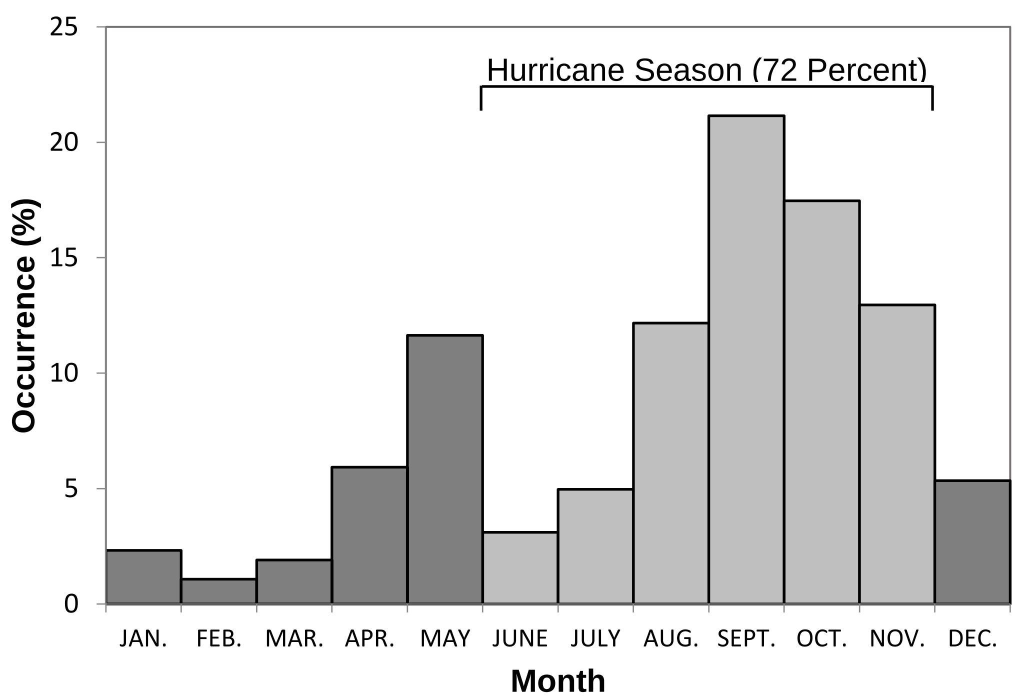

Figure 5: Monthly occurrence of 2,416 annual maximum peak discharges for 75 stream-gaged sites in Puerto Rico, from 1899 to 2019

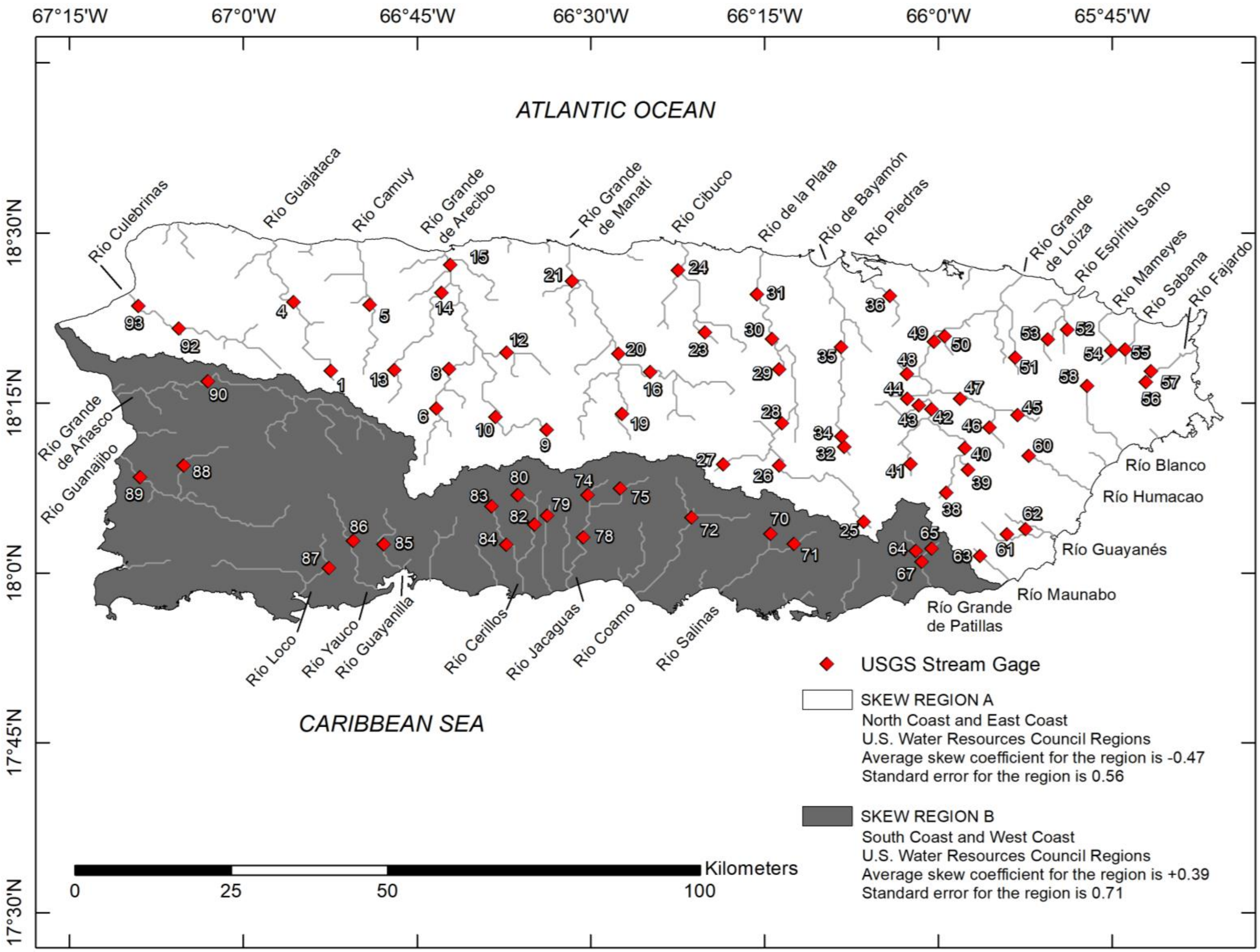

Figure 6: Locations of USGS streamgages within Puerto Rico Skew Regions, numbered by Study Index as listed in Table 1. Streams provided by National Hydrography Dataset Plus (Moore & Dewald, 2016).

3.3.2 Local Climatic and Meteorological Data

Together, the USGS and NOAA report weather data from 130 stations across the main island of Puerto Rico. While the NOAA stations provide insight into the historical climate of Puerto Rico, the USGS stations allow for validation of remote sensing estimates of daily rainfall. Table 4 and Table 5 list the active raingages and weather stations used in this study with some basic characteristics, while Figure 7 shows their location alongside USGS streamgages.

Mean annual rainfall accumulations for each modelled watershed was estimated using NOAA's 1981- 2010 climate normals, the latest decadal installment of 30-yr averages and other statistics of meteorological variables for the United States and its territories. Climate normals of annual rainfall were provided at 51 NOAA weather stations located across the main island of Puerto Rico (Arguez et al., 2012). In addition, the intensity of 24-hour storms was estimated using NOAA Atlas 14, the official United States government source of precipitation frequency estimates. Point values of mean annual rainfall and 24-hour storm intensity were interpolated using an ordinary kriging method that has seen popular use in basic meteorological applications (Noel, 1990). Then, basin averages were calculated at each of the 75 modelled basins, shown in Table 1.

The USGS reports daily rainfall accumulations at 79 raingage stations operated by the JCA, AEEPR, AAAPR, and USACE. Nearly 47% (37 stations) have a record shorter than one full year. Data gathered by these stations was only used to validate GPM IMERG estimates of rainfall when available. Figure 8 shows a timeline of rain accumulation records at 79 USGS raingage sites compared to the record of GPM rainfall estimates.

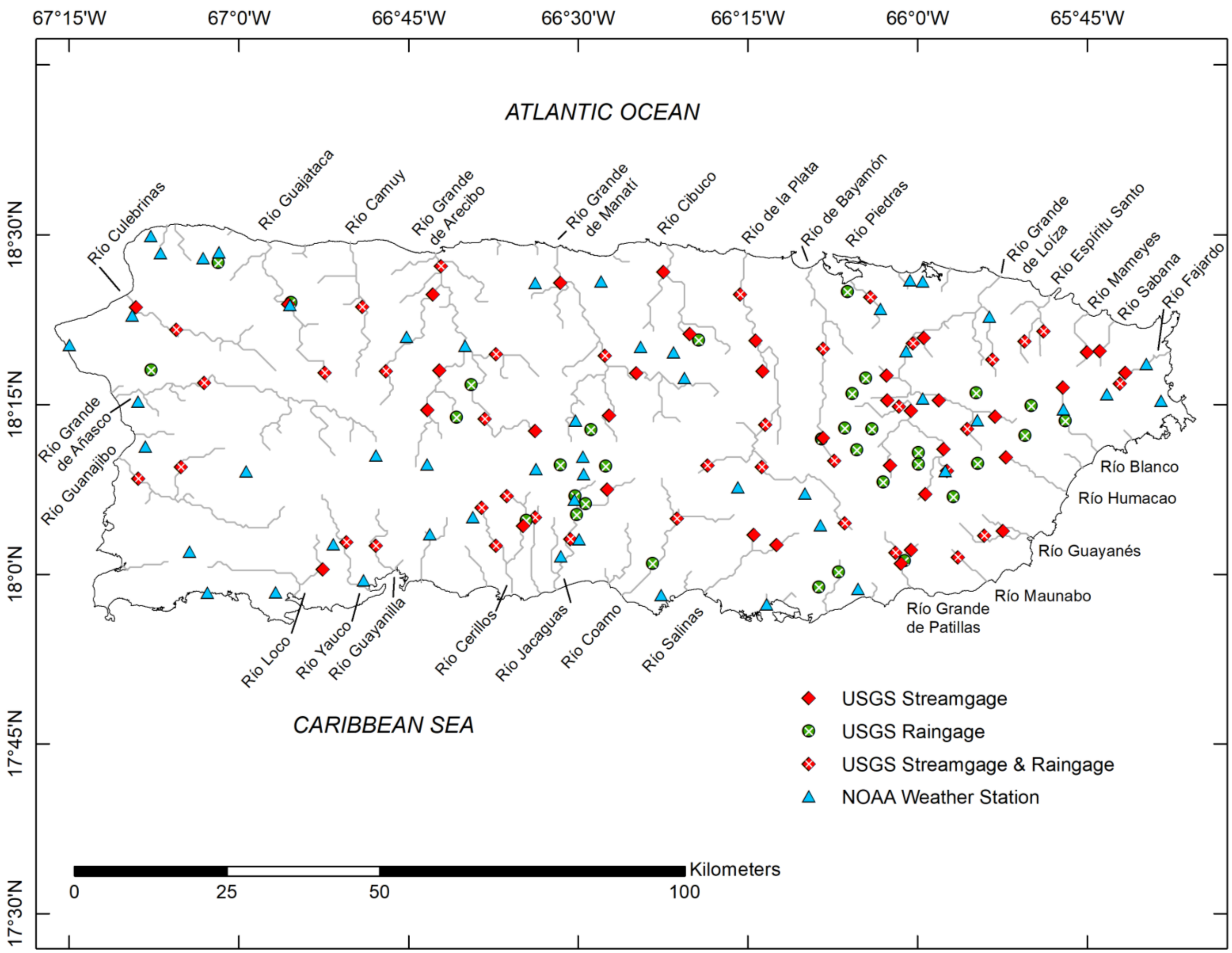

Figure 7: Gage locations. Streams provided by National Hydrography Dataset Plus (Moore & Dewald, 2016).

Table 4: Active USGS Raingages on main island of Puerto Rico

[*Study Index*, numerical identifier of each gage, created for this study; *USGS Raingage*, numerical identifier for each USGS raingage station; *Site Name*, name describing USGS raingage station; *Type*, identifier for data recorded by USGS raingage station (R = rainfall, S = streamflow); *Lat.*, decimal latitude of watershed outlet with NAD83 datum; *Lon.*, decimal longitude of watershed outlet with NAD83 datum]

Study Index	USGS Raingage	Site Name	Type	Lat.	Lon.	Years of Record	Period of Record
1	50010500	Río Guajataca at Lares	R, S	18.297	-66.873	3	2016-'19
2	50010800	Lago Guajataca at damsite near Quebradillas	R	18.400	-66.923	<1	2018-'19
3	50011088	Lago Regulador de Isabela near Highway 112 Isabella	R	18.459	-67.030	3	2016-'19
5	50014800	Río Camuy near Bayaney	R, S	18.394	-66.818	<1	2018-'19
7	50023110	Lago Vivi near Utuado	R	18.231	-66.679	3	2016-'19
10	50026025	Río Caonillas at Paso Palma	R, S	18.229	-66.637	<1	2018-'19
11	50026140	Lago Caonillas at damsite near Utuado	R	18.279	-66.657	<1	2018-'19
12	50027000	Río Limon above Lago Dos Bocas	R, S	18.324	-66.621	<1	2018-'19
13	50028000	Río Tanama near Utuado	R, S	18.299	-66.783	3	2016-'19
15	50029000	Río Grande de Arecibo at Central Cambalache	R, S	18.454	-66.702	3	2016-'19
17	50032290	Lago Guineo at damsite near Villalba	R	18.161	-66.526	<1	2018-'19
18	50032590	Lago de Matrullas at damsite near Orocovis	R	18.213	-66.481	3	2016-'19
20	50035000	Río Grande de Manatí at Ciales	R, S	18.322	-66.460	<1	2018-'19
22	50038300	Río Corozal at Corozal	R	18.345	-66.322	<1	2018-'19
25	50039995	Río Carité at spillway	R, S	18.075	-66.107	<1	2018-'19
26	50043000	Río de la Plata at Proyecto La Plata	R, S	18.158	-66.229	<1	2018-'19
27	50043197	Río Usabón at Highway 162 near Barranquitas	R, S	18.160	-66.309	3	2016-'19
28	50043800	Río de la Plata at Comerio	R, S	18.220	-66.224	3	2016-'19
31	50046000	Río de la Plata at Highway 2 near Toa Alta	R, S	18.412	-66.261	<1	2018-'19
32	50047535	Río de Bayamón at Arenas	R, S	18.167	-66.122	<1	2018-'19
33	50047550	Lago de Cidra at damsite near Cidra	R	18.199	-66.141	3	2016-'19
35	50047850	Río de Bayamón near Bayamón	R, S	18.332	-66.139	<1	2018-'19
36	50049100	Río Piedras at Hato Rey	R, S	18.408	-66.069	<1	2018-'19
37	50049620	Quebrada Margarita at Caparra near Guaynabo	R	18.416	-66.103	3	2016-'19
39	50051310	Río Cayaguas at Cerro Gordo	R, S	18.152	-65.956	3	2016-'19
43	50055225	Río Caguitas at Villa Blanca at Caguas	R, S	18.247	-66.027	3	2016-'19
46	50056400	Río Valenciano near Juncos	R, S	18.214	-65.926	3	2016-'19
49	50059050	Río Grande de Loíza below Loíza damsite	R, S	18.340	-66.006	<1	2018-'18
51	50061800	Río Canovanas near Campo Rico	R, S	18.316	-65.889	<1	2018-'19
52	50063800	Río Espíritu Santo near Río Grande	R, S	18.358	-65.814	2	2017-'19
53	50064200	Río Grande near El Verde	R, S	18.343	-65.842	<1	2018-'19
56	50070900	Río Fajardo at Paraíso near Fajardo	R, S	18.281	-65.701	<1	2018-'19
58	50075000	Río Icacos near Naguabo	R, S	18.275	-65.785	3	2016-'19
59	50076800	Lago Blanco near Naguabo	R	18.226	-65.782	<1	2018-'19
61	50083500	Río Guayanés near Yabucoa	R, S	18.057	-65.901	<1	2018-'19
63	50090500	Río Maunabo at Lizas	R, S	18.025	-65.940	<1	2018-'19
64	50092000	Río Grande de Patillas near Patillas	R	18.032	-66.032	<1	2018-'19

Table 4 – Continued

Study Index	USGS Raingage	Site Name	Type	Lat.	Lon.	Years of Record	Period of Record
66	50093045	Lago Patillas at damsite near Patillas	R	18.020	-66.019	3	2016-'19
68	50095000	Canal de Guamani Oeste at Highway 15 Guayama	R	18.003	-66.116	<1	2018-'19
69	50095800	Lago Melania near Guayama	R	17.981	-66.145	2	2017-'19
72	50106100	Río Coamo at Highway 14 at Coamo	R, S	18.082	-66.354	3	2016-'19
73	50106850	Lago Coamo near Los Llanos	R	18.016	-66.390	3	2016-'19
76	50111210	Lago Toa Vaca at damsite near Villalba	R	18.104	-66.489	3	2016-'19
77	50111300	Lago Guayabal at damsite near Juana Diaz	R	18.088	-66.502	<1	2018-'19
78	50111500	Río Jacaguas at Juana Díaz	R, S	18.052	-66.511	<1	2018-'19
79	50112500	Río Inabón at Real Abajo	R, S	18.084	-66.563	<1	2018-'19
80	50113800	Río Cerrillos above Lago Cerrillos near Ponce	R, S	18.115	-66.605	<1	2018-'19
81	50113950	Lago Cerrillos at damsite near Ponce	R	18.079	-66.576	2	2017-'19
83	50114900	Río Portugues near Tibes	R, S	18.098	-66.642	3	2016-'19
84	50115240	Río Portugues at Parque Ceremonial Tibes nr Ponce	R, S	18.042	-66.621	3	2016-'19
85	50124200	Río Guayanilla near Guayanilla	R, S	18.042	-66.798	<1	2018-'19
86	50126150	Río Yauco above Diversión Monserrate near Yauco	R, S	18.047	-66.841	3	2016-'19
88	50136400	Río Rosario near Hormigueros	R, S	18.158	-67.085	<1	2018-'19
89	50138000	Río Guanajibo near Hormigueros	R, S	18.141	-67.148	<1	2018-'19
90	50144000	Río Grande de Añasco near San Sebastián	R, S	18.282	-67.051	<1	2018-'19
91	50146073	Lago Daguy above Añasco	R	18.301	-67.129	<1	2018-'19
92	50147800	Río Culebrinas at Highway 404 near Moca	R, S	18.360	-67.092	<1	2018-'19
94	50999954	Quebrada Salvatierra Raingage at San Lorenzo	R	18.179	-65.998	<1	2018-'19
95	50999956	Quebrada Blanca Raingage at San Lorenzo	R	18.162	-65.998	3	2016-'19
96	50999958	Pueblito del Río Raingage at Las Piedras	R	18.248	-65.832	3	2016-'19
97	50999959	Gurabo Abajo Raingage at Gurabo	R	18.267	-65.913	<1	2018-'19
98	50999960	Quebrada Arenas Raingage at San Lorenzo	R	18.114	-65.947	3	2016-'19
99	50999961	La Plaza Raingage at Caguas	R	18.136	-66.050	3	2016-'19
100	50999962	Canaboncito Raingage at Aguas Buenas	R	18.215	-66.107	3	2016-'19
101	50999963	Jagueyes Abajo Raingage at Aguas Buenas	R	18.289	-66.076	3	2016-'19
102	50999964	Bairoa Arriba Raingage at Aguas Buenas	R	18.266	-66.096	3	2016-'19
103	50999965	Vaquería El Mimo Raingage at Caguas	R	18.214	-66.067	3	2016-'19
104	50999966	Barrio Beatriz Raingage at Caguas	R	18.183	-66.089	3	2016-'19
105	50999967	Barrio Montones Raingage at Las Piedras	R	18.163	-65.911	3	2016-'19
106	50999968	Las Piedras Construction Raingage at Las Piedras	R	18.204	-65.841	2	2017-'19
107	50999970	Barrio Apeadero Raingage near Villalba	R	18.159	-66.459	3	2016-'19
108	175858066100200	Jua 5 Well at Guayama	R	17.983	-66.167	3	2016-'19
109	180122066560300	Arenas 1 Well at Guanica	R	18.022	-66.934	<1	2018-'19
110	181026066100300	Barrio Rabanal Raingage at Cidra	R	18.174	-66.168	3	2016-'19
111	181529065575200	Gurabo Raingage at Gurabo	R	18.258	-65.964	3	2016-'19
112	181708066152400	Barrio Anones Raingage near Naranjito	R	18.286	-66.257	3	2016-'19
113	182134066544600	Barrio Guajataca Raingage above Lago Guajataca	R	18.359	-66.913	2	2017-'19
114	182350066063700	Raingage near Altamira Guaynabo	R	18.397	-66.110	3	2016-'19
115	182647066201700	Sabana Hoyos 2 Well at Vega Alta	R	18.446	-66.339	3	2016-'19

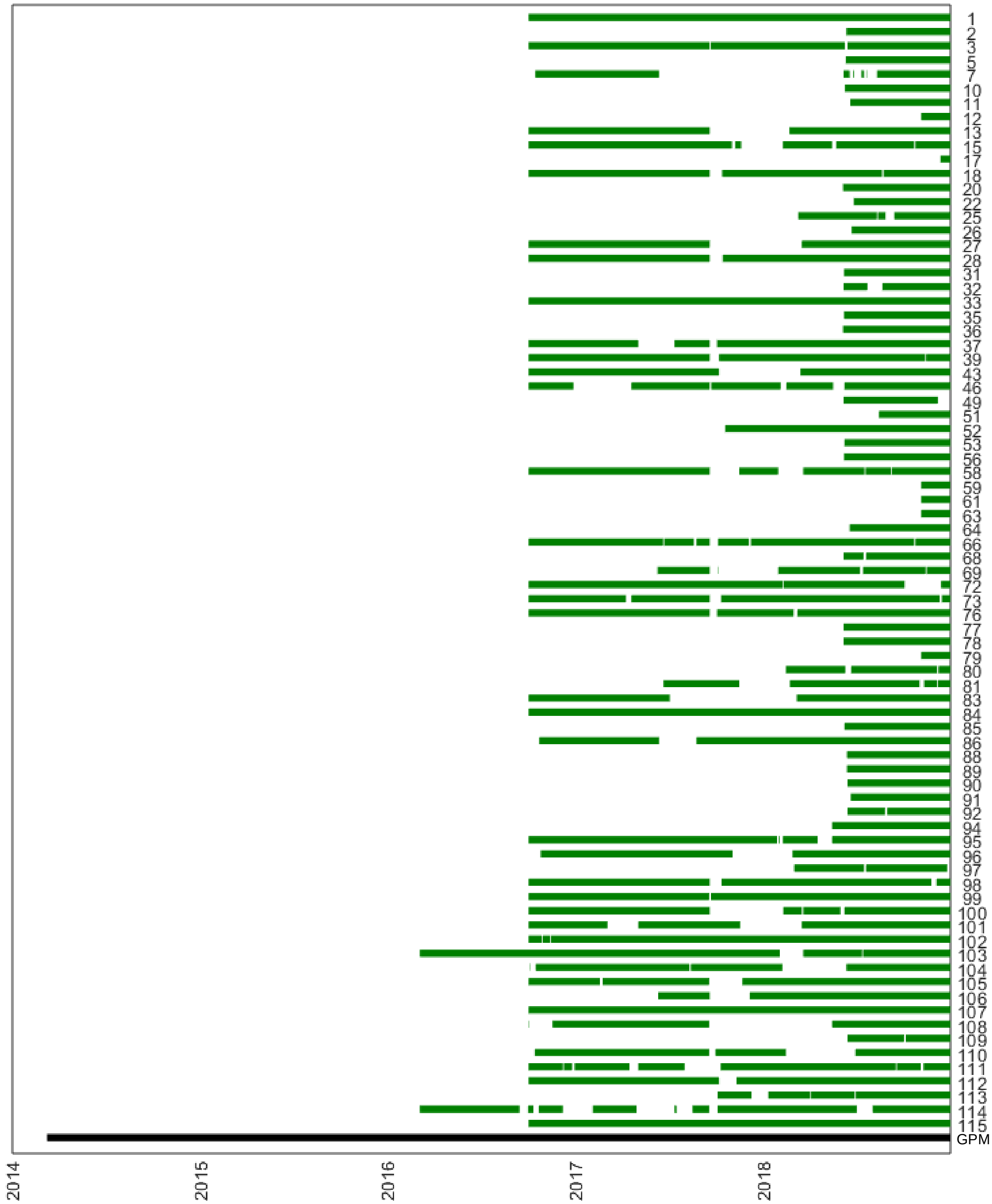

Figure 8: Timeline of daily raingage record reported at 79 selected USGS monitoring stations ordered by their Study Index (green), and the record of GPM IMERG data releases (black).

Table 5: Active NOAA weather stations reporting 1981- 2010 precipitation climate normals on main island of Puerto Rico

[*Study Index*, numerical identifier of each gage, created for this study; *NOAA Station*, numerical identifier for each NOAA weather station; *Site Name*, name describing NOAA weather station; *Lat.*, decimal latitude of watershed outlet with NAD83 datum; *Lon.*, decimal longitude of watershed outlet with NAD83 datum; *Annual Rainfall*, reported annual precipitation climate normal at each station]

Study Index	NOAA Station	Site Name	Lat.	Lon.	Years of Record	Period of Record	Annual Rainfall (mm)
116	RQC00660040	Aceituna Water Treatment Plant	18.147	-66.492	30	1981-'10	1942
117	RQC00660053	Adjuntas 1 NW	18.161	-66.722	30	1981-'10	1972
118	RQC00660061	Adjuntas Substation	18.175	-66.798	30	1981-'10	1997
119	RQC00660152	Aguirre	17.956	-66.222	30	1981-'10	1009
120	RQC00660158	Aibonito 1 S	18.128	-66.264	30	1981-'10	1530
121	RQC00660426	Arecibo Observatory	18.349	-66.753	30	1981-'10	2137
122	RQC00660668	Barceloneta 3 SW	18.429	-66.563	30	1981-'10	1589
123	RQC00662316	Boca	17.991	-66.816	30	1981-'10	846
124	RQW00011603	Borinquen Airport	18.498	-67.129	30	1981-'10	1390
125	RQC00661142	Cacaos Orocovis	18.226	-66.504	30	1981-'10	2155
126	RQC00661345	Calero Camp	18.472	-67.116	30	1981-'10	1466
127	RQC00661590	Canovanas	18.379	-65.894	30	1981-'10	1963
128	RQC00661901	Cayey 1 E	18.119	-66.166	30	1981-'10	1501
129	RQC00662336	Cerro Maravilla	18.155	-66.562	30	1981-'10	2523
130	RQC00662801	Coloso	18.381	-67.157	30	1981-'10	1925
131	RQC00662934	Corozal Substation	18.327	-66.359	30	1981-'10	1975
132	RQC00663023	Corral Viejo	18.084	-66.655	30	1981-'10	1582
133	RQC00663431	Dos Bocas	18.336	-66.667	30	1981-'10	1942
134	RQC00663532	Ensenada 1 W	17.973	-66.946	30	1981-'10	858
135	RQC00663657	Fajardo	18.310	-65.663	30	1981-'10	1709
136	RQC00663904	Guajataca Dam	18.396	-66.924	30	1981-'10	1933
137	RQC00664193	Guayama 2 E	17.978	-66.087	30	1981-'10	1386
138	RQC00664276	Gurabo Substation	18.258	-65.992	30	1981-'10	1653
139	RQC00664702	Isabela Substation	18.465	-67.053	30	1981-'10	1650
140	RQC00664867	Jajome Alto	18.072	-66.143	30	1981-'10	1934
141	RQC00665020	Juana Diaz Camp	18.051	-66.499	30	1981-'10	1071
142	RQC00665064	Juncos 1 SE	18.226	-65.911	30	1981-'10	1737
143	RQC00665097	Lajas Substation	18.033	-67.072	30	1981-'10	1219
144	RQC00665693	Magueyes Island	17.972	-67.046	30	1981-'10	1101
145	RQC00665807	Manatí 2 E	18.431	-66.466	30	1981-'10	1566
146	RQC00665908	Maricao 2 SSW	18.151	-66.989	30	1981-'10	2307
147	RQC00666083	Mayaguez Airport	18.254	-67.149	30	1981-'10	2167
148	RQC00666073	Mayaguez City	18.188	-67.138	30	1981-'10	1510
149	RQC00666361	Mora Camp	18.474	-67.029	30	1981-'10	1540
150	RQC00666390	Morovis 1 N	18.334	-66.408	30	1981-'10	1856
151	RQC00666514	Negro Corozal	18.289	-66.343	30	1981-'10	1913

Table 5 – Continued

Study Index	NOAA Station	Site Name	Lat.	Lon.	Years of Record	Period of Record	Annual Rainfall (mm)
152	RQC00666805	Paraíso	18.265	-65.721	30	1981-'10	2543
153	RQC00666983	Penualas 1 E	18.059	-66.718	30	1981-'10	1480
154	RQC00667292	Ponce 4 E	18.026	-66.525	30	1981-'10	977
155	RQC00668126	Rincon	18.338	-67.250	30	1981-'10	1522
156	RQC00668144	Río Blanco Lower	18.243	-65.785	30	1981-'10	2721
157	RQC00668306	Río Piedras Experimental Station	18.391	-66.054	30	1981-'10	1798
158	RQW00011630	Roosevelt Roads	18.255	-65.641	30	1981-'10	1329
159	RQW00011641	San Juan L M Marin Int'l. Airport	18.433	-66.011	30	1981-'10	1431
160	RQC00668815	San Lorenzo 3 S	18.152	-65.959	30	1981-'10	2406
161	RQC00668940	Santa Isabel	17.969	-66.377	30	1981-'10	921
162	RQC00669432	Toro Negro Forest	18.173	-66.493	30	1981-'10	2361
163	RQC00669521	Trujillo Alto SSW	18.328	-66.016	30	1981-'10	1792
164	RQC00669774	Villalba 1 SE	18.109	-66.506	30	1981-'10	1464
165	RQC00668814	Weather Forecast Office San Juan	18.431	-65.992	30	1981-'10	1857
166	RQC00669860	Yauco 1 NW	18.044	-66.861	30	1981-'10	1206

CHAPTER 4: SATELLITE REMOTE SENSING DATA

4.1 Introduction

Satellite remote sensing provides major sources of consistent, continuous data for atmospheric, ocean, and land studies at a variety of spatial and temporal scales across the globe. This is a powerful tool for experts in hydroscience and engineering to characterize and understand Earth system processes as they influence the movement and storage of water resources. Satellites measure a variety of physical quantities to gain insight into the complex water and energy cycles of Earth.

This chapter describes the three datasets gathered via satellite remote sensing that were used to build and operate watershed streamflow models across the main island of Puerto Rico:

(1) Elevation data obtained by the Space Shuttle Endeavour through the Shuttle Radar Topography Mission

(2) Rainfall estimates gathered by a constellation of satellites through the Global Precipitation Measurement Mission

(3) Evapotranspiration estimates collected by Moderate Resolution Imaging Spectroradiometer sensors aboard the Aqua and Terra satellites

The data products detailed here are unique because they offer benefit to global populations, not just local citizens. This is the power of satellite remote sensing.

4.2 Elevation from Shuttle Radar Topography Mission

Predicting spatial patterns and rates of runoff generation requires both a hydrologic model and characterization of the land surface. Most physically based models of hydrologic and geomorphic processes rely on spatially distributed or lumped characterizations of local slope and the drainage area (Beven & Kirkby, 2010; O'Loughlin, 1986). To understand the topography of Puerto Rico's terrain, I assembled a series of basin-scale Digital Elevation Models (DEM) built from elevation data gathered by the Shuttle Radar Topography Mission (SRTM).

SRTM is an international research effort spearheaded by the U.S. National Geospatial-Intelligence Agency (NGA) and NASA that obtained digital elevation models on a near-global scale. SRTM consisted of a dual-antenna radar system mounted to the Space Shuttle Endeavour during its 11-day mission in February 2000. Although SRTM gathered a single set of raw data, multiple products have been released of increasing resolution and quality. SRTM provides elevation data between latitudes 56°S to 60°N.

4.2.1 SRTM Radar Instrument Remote Sensing

During its 11-day mission, Space Shuttle Endeavour orbited Earth 16 times. The shuttle's cargo bay was outfitted with an active main antenna. Once the shuttle was in space, a mast extended out 60 meters from the main antenna truss. At the end of the mast, the passive outboard antenna acted as the second vantage point to receive radar signals. The main radar antenna transmitted a radar pulse toward Earth that was received by both the main radar antenna and the outboard antenna.

The SRTM instruments transmitted and collected two radar frequency bands. Both the main antenna and outboard antenna each contained C-Band and X-Band panels. The C-Band panel on the main antenna could transmit and receive radar signals with a wavelength of 5.6 centimeters. Its swath width was 225 kilometers, covering about 80% of Earth's land surface. The X-Band panel on the main antenna could transmit and receive radar signals with a wavelength of 3 centimeters. Its swath width was 50 kilometers, providing higher resolution data with less coverage over Earth's land surface. The outboard antenna received both the C-Band and X-Band signals but did not transmit pulses from its radar panels. These two synthetic aperture radar antennae collected independent images of Earth's surface that were combined to create an interferometric radar dataset of land surface elevation.

4.2.2 SRTM Data Processing and Integration

NASA's SRTM C-Band data processing system was comprised of three parts: interferometric processor, which converted the raw radar data into a height map and radar image strips; mosaic processor, compiled a mosaic of the height and image data one continent at a time from the many radar image strips; and the verification system, which tested the mosaics for quality, producing an accuracy map. In September 2014, a 1 arc-second near-global digital elevation model was released, providing elevation data for Puerto Rico with a spatial resolution of approximately 90 meters. The SRTM-derived DEM of Puerto Rico is shown in Figure 9.

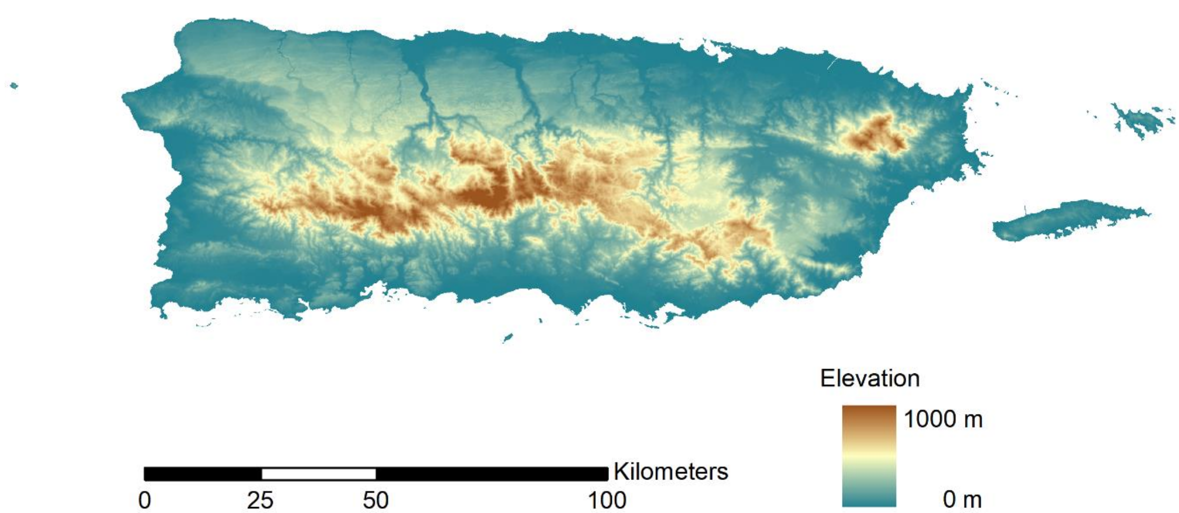

Figure 9: Topography of Puerto Rico from Shuttle Radar Topography Mission 1 arc-second Digital Elevation Model

4.3 Rainfall from Global Precipitation Measurement Mission

Rainfall drives runoff and potential flood disasters. As such, estimating rainfall accurately is crucial in understanding flood risk. The Global precipitation Measurement (GPM) Mission was launched in February 2014 to record frequent observations of Earth's precipitation. I utilized GPM observations to better understand the behavior or rainfall patterns over Puerto Rico and drive watershed runoff models across the island.

Operationally, the GPM mission is an international network of satellites that provide global estimates of rain and snow. In total, 13 satellites comprise this network, referred to as the "GPM constellation." At the heart of this constellation is the GPM Core Observatory. Its launch marks the beginning of the GPM mission in 2014. In fact, none of the other partner satellites were build and launched specifically for the GPM mission. Instead, this joint mission from NASA and the Japan Aerospace Exploration Agency (JAXA) integrates data already being gathered by satellites that were launched by other scientific agencies for other purposes. As a part of the GPM mission, data from the dozen partner satellites are converted to precipitation observations. Each satellite has a unique orbit and coverage zone so that a broad snapshot of Earth's precipitation can be provided at any point of the day. The GPM Core Observatory is so critical because its orbit overlaps all others, providing a common reference for all other satellites so that the GPM dataset may be calibrated to match up over its near-global footprint extending from latitudes 60°S to 60°N. (Hou et al., 2013).

4.3.1 GPM Core Observatory Remote Sensing

The Core satellite uses two measurement instruments, the GPM Microwave Imager (GMI) and the Dual-frequency Precipitation Radar (DPR). Together, these two instruments provide measurements against which partner satellite microwave measurements may be compared. Figure 10 illustrates the configuration of the GMI and DPR on the Core Observatory with their coverage swaths.

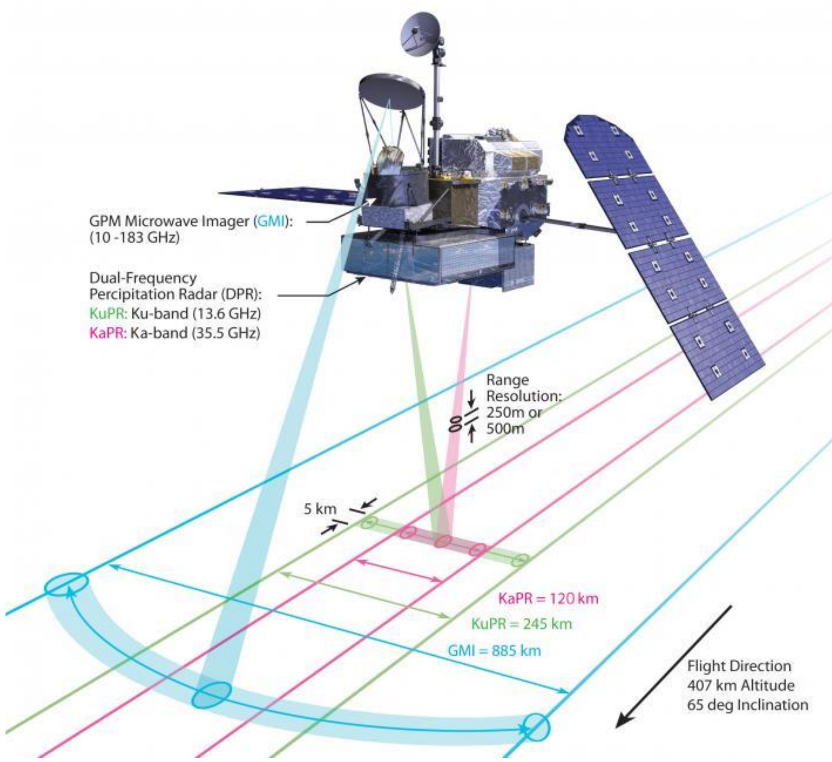

Figure 10: GPM Core Observatory instrument configuration and coverage (Hou et al., 2013)

The GMI is a powerful conical-scan microwave radiometer that delivers thirteen high-frequency channels of atmosphere brightness temperature measurements. Its 1.2-meter diameter antenna rotates 32 times per minute, providing improved spatial resolution from its predecessor, the microwave imager aboard the Tropical Rainfall Measurement Mission (TRMM). The GMI measures the intensity of microwave energy emitted by the atmosphere. The amount of radiation received is expressed as the brightness temperature. In the microwave region, absorption lines show spikes in brightness temperature used to profile temperature profiles, humidity, and other atmospheric conditions. GMI observations are used to derive vertical profiles of water vapor and ultimately rainfall rate. Note once again that GMI instrumentations enables the Core spacecraft to serve as both a precipitation standard and as a radiometric standard for the other GPM constellation members.

The DPR consists of a Ku-band precipitation radar (KuPR) and a Ka-band precipitation radar (KaPR). Much like the GMI, these devices that comprise the DPR are new and improved versions of devices flows on the TRMM satellite. Data collected from the KuPR and KaPR units provides 3-dimensional observations of rain in addition to an accurate estimation of rainfall rate with a sensitivity of 0.2 mm/hr. KaPR is used primarily to detect snow and light rain, even in high altitude environments. The KuPR is used primarily to detect heavy rainfall. The DPR utilizes differential attenuation observed by these two devices to determine if rain or snow is being measured.

4.3.2 GPM Data Processing and Integration via IMERG

A variety of Global Precipitation Measurement mission datasets are available, from raw brightness temperature observations to precipitation estimates from combined satellite and raingage measurements. The algorithm and processing sequence for the Integrated Multi-SatellitE Retrievals for GPM (IMERG) is intended to intercalibrate, merge, and interpolate satellite all available microwave precipitation estimates from the entire GPM constellation with microwave-calibrated infrared (IR) satellite estimates, precipitation gauge analyses, and other precipitation estimators. This process described fully within the Version 5 Algorithm Theoretical Basis Document (ATBD) for IMERG (Huffman et al., 2018).

Passive microwave sensors aboard the low-earth-orbit GPM constellation satellites provide the majority of the satellite-based precipitation measurements. IMERG compensates for the limited sampling rate of the GPM constellation satellites by combining with data from all other low-earth-orbit satellites and then augmenting the net product with geosynchronous-Earth-orbit IR estimates. Finally, precipitation gauge analyses are used to provide crucial regional bias correction to the combined satellite estimates.

The IMERG system is comprised of the following rainfall retrieval algorithms: the Climate Prediction Center Morphing-Kalman Filter (CMORPH-KF) (Joyce & Xie, 2011), the Precipitation Estimation from Remotely Sensed Information using Artificial Neural Networks-Cloud Classification System (PERSIANN-CCS) (Hong, Hsu, & Gao, 2004), and the TRMM Multi-Satellite Precipitation Analysis (TMPA) (Huffman et al., 2007). Since the release of IMERG data in April 2014, extensive studies have been devoted to the evaluation of the IMERG rainfall estimates compared to ground observations such as radars and gauges, or to other existing satellite rainfall data (Gaona, Overeem, Leijnse, & Uijlenhoet, 2016; Ndayisaba et al., 2016; Pai et al., 2016; Sharifi, Steinacker, & Saghafian, 2016; Tan, Petersen, & Tokay, 2016). An intercomparison study between the data using a hydrological model, that the IMERG products can adequately substitute TMPA products, both statistically and hydrologically (Tang, Ma, Long, Zhong, & Hong, 2016).

IMERG delivers GPM's highest resolution dataset at 0.1º maximum spatial resolution and 30-minute temporal resolution. Figure 11 shows the footprint of this GPM IMERG product over the main island of Puerto Rico. IMERG products are available in the form of near-real-time data, i.e., IMERG Early Run and Late Run, and in the form of post-real-time research data, i.e., IMERG Final Run, after monthly raingage analysis is received and taken into account. IMERG Early Run, Late Run, and Final Run data is released with a latency of 4 hours, 12 hours, and 2.5 months after observation time, respectively. While reducing this latency is crucial to operational forecasting systems, I chose to utilize IMERG Late Run data because it performs better than Early Run releases and is not gage-corrected like Final Run releases (Sungmin et al., 2017; Wang, Zhong, Lai, & Chen, 2017).

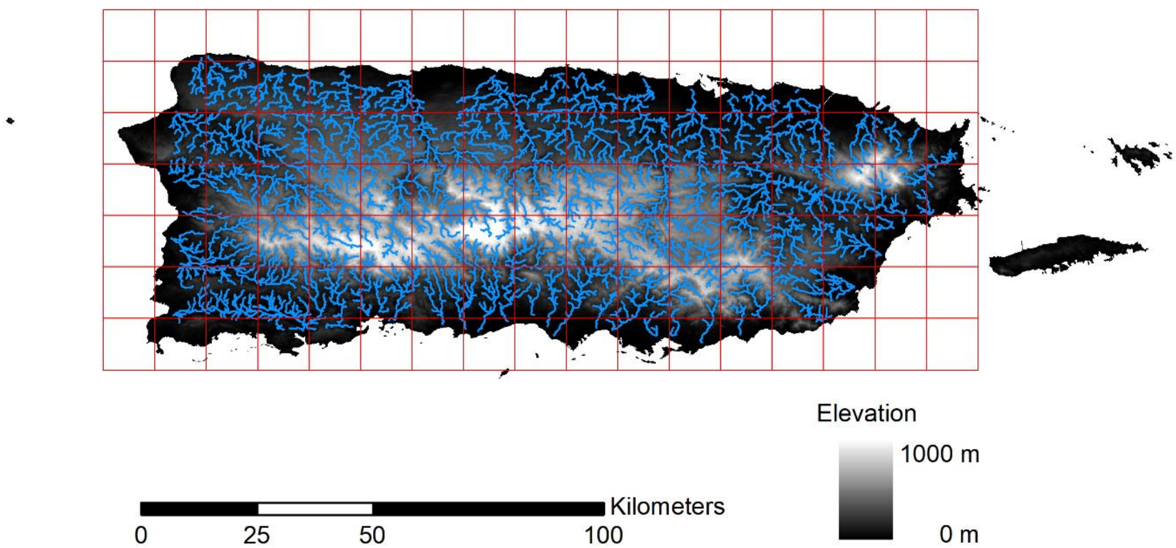

Figure 11: Integrated Multi-SatellitE Retrievals for Global Precipitation Measurement 0.1º spatial resolution product footprint over Puerto Rico with river network extracted from Shuttle Radar Topography Mission 1 arc-second Digital Elevation Model

4.4 Evapotranspiration from Moderate Resolution Imaging Spectroradiometer

Evapotranspiration is a key component of the global water cycle, constituting a significant water loss from drainage basins. On an annual basis, evapotranspiration (ET) is the largest consumptive use of water and is usually the second most important quantity in regional water budgets, second only to rainfall. It is not unusual for ET to consume around 70% of global rainfall on an annual basis (Chin, 2013). Evaporation is the process by which water is transformed from the liquid phase to the vapor phase, and transpiration by which water moves through plants and evaporates through leaf stomata. It is difficult to differentiate between these processes where the ground surface is covered by vegetation like Puerto Rico, but combined ET estimates are sufficient in modelling outward water flux from watersheds to the atmosphere. Traditionally, actual evapotranspiration has been computed as a residual in water balance equations, from estimates of potential evapotranspiration or, indirectly, from field measurements at meteorological stations (Kite & Droogers, 2000). But, modern remote sensing methods are now recognized as the most feasible means to provide such regional ET estimates over vegetated land surfaces (Courault, Seguin, & Olioso, 2005; Jiang & Islam, 1999; Kustas & Norman, 1996). To estimate evapotranspiration rates across Puerto Rico, I used estimates obtained by the Moderate Resolution Imaging Spectroradiomenter (MODIS).

MODIS is a key instrument carried by the NASA Earth Observing System AM-1 satellite, also known as “Terra,” and NASA Earth Observing System PM-1 satellite, also known as “Aqua.” Terra's orbit around the Earth is timed so that it passes from north to south across the equator in the morning, while Aqua passes south to north over the equator in the afternoon. Together, the MODIS devices aboard these satellites have sweeping 2,330-km wide viewing swaths that cover the entire Earth's surface every two days.

4.4.1 MODIS Instrument Remote Sensing

MODIS is designed to measure spectral radiance across 36 spectral bands ranging from 0.405 to 14.385 µm. It does so by detecting an analog signal of oncoming photons and converting it into digital data. Light that is reflected or emitted by the Earth back to outer space will pass through MODIS' scan aperture, enter into the scan cavity, and hit the scan mirror that reflects the incoming light onto MODIS' internal telescope, which in turn focuses the light onto four different detector assemblies.

First, light passes through the scan aperture. En route to the detector assemblies, light passes through spectral filters and beamsplitters that divide the light into wavelength bands within the scan cavity. Photons then strike one of four detector assemblies depending on its wavelength. MODIS is equipped with detectors for visible light, near infrared, shortwave/midwave infrared, and longwave infrared detection. Each time a photon strikes these detectors an electron is displaced and collected on a capacitor. They accumulate until they can be routed to a digitizer which converts the electrons from an analog signal to raw digital data.

4.4.1 MODIS Data Processing and Integration

Many ATBDs were developed for the MODIS devices aboard the Aqua & Terra Satellites. The algorithms described within utilize both physical theory and mathematical procedures with fundamental assumptions to convert the radiances received by the instruments to geophysical quantities describing behavior of the atmosphere, land, cryosphere, and ocean. Over 30 data products are released using MODIS measurements, each requiring its own ATBD that describes how earth system processes are assessed using radiance observations as a proxy. The NASA MOD16A2/A3 ATBD describes how evapotranspiration is estimated over the 109.03 million km^2 global vegetated land area.

The global 8-day (MOD16A2) and annual (MOD16A3) datasets provide terrestrial evapotranspiration estimates at 0.125° (~0.5-km) spatial resolution. The algorithm takes into account evaporation from wet and moist soil, evaporation from rainwater intercepted by the canopy before it reaches the ground, and transpiration through stomata on foliage. It follows the logic of the Penman-Monteith physical model, while having to hurdle over its associated challenges like requiring meteorological forcing data and aerodynamic and surface resistance inputs. This is made possible by daily meteorological data provided by NASA's Global Modeling and Assimilation Office (GMAO), which is derived using a global circulation model (GCM) that incorporates both remote sensing and in-situ measurements (Mu et al., 2013). Figure 12 shows a MODIS estimate of monthly evapotranspiration over Puerto Rico.

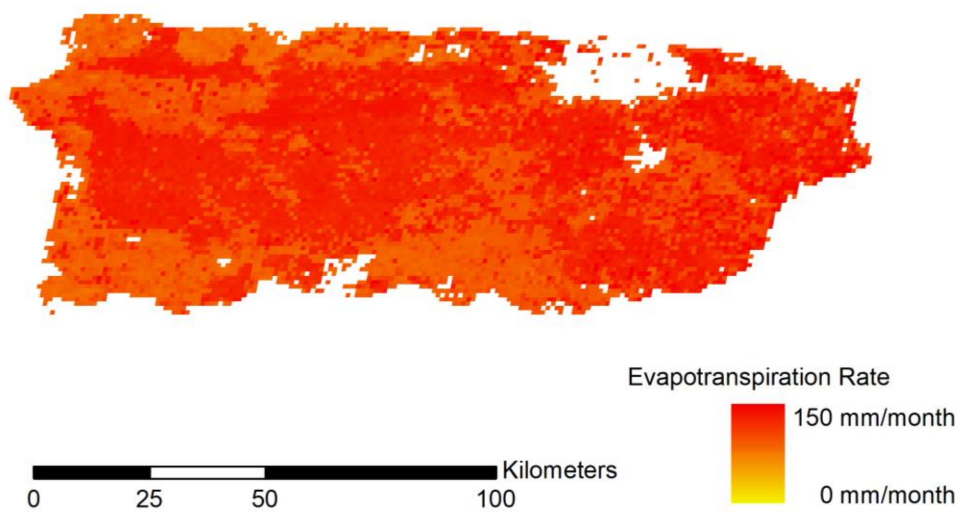

Figure 12: Moderate Resolution Imaging Spectroradiometer estimates of monthly evapotranspiration rate over the main island of Puerto Rico during August 2014

CHAPTER 5: METHODOLOGY

5.1 Introduction

To model streamflow and runoff across Puerto Rico, I adopted a geomorphologic partitioning of the island's natural terrain into links and hillslopes built from the SRTM-derived DEM. Links are defined as the portion of a channel between two junctions of a river network, and hillslopes are the adjacent areas that drain into the link. Hillslope-link models (HLMs) provide basic units of landscape organization into which a drainage basin is partitioned. Each hillslope-link unit defines a single natural finite control volume for modelling water transport (Mantilla, 2007; Mantilla & Gupta, 2005).

Water transport, in and out of hillslope-link units, was modeled using the Iowa Flood Center Top Layer hydrologic model. It separates the terrain into vertical soil layers, using ordinary differential equations (ODEs) to describe hillslope-link water transport processes including infiltration, percolation, runoff, evapotranspiration, and storage. Chapter 5.2 describes the governing equations and parameters that simulate each process. Chapter 5.3, Chapter 5.4, and Chapter 5.5 detail how local and satellite remote sensing data products were used as model forcings and parameters. Chapter 5.6 and Chapter 5.7 describe model setup and operation.

5.2 Iowa Flood Center Top Layer Hydrologic Model Description

The IFC Top Layer model is the current standard hillslope-link conceptual model used by the Iowa Flood Center, often referred to by its numerical code, "HLM-ASYNCH-254." This model represents the soil column as three vertical layers: the terrain surface, an upper soil layer referred to as the "top layer," and a lower soil layer referred to as the "subsurface." Each of these three layers acts as a storage volume and can generate streamflow in rates that vary in time. The

IFC Top Layer model is operated by modelling water fluxes from precipitation at a high temporal resolution (5-minute to hourly) and evapotranspiration rates at a low temporal resolution (daily or monthly) (Quintero, Mantilla, Anderson, Claman, & Krajewski, 2018).

5.2.1 IFC Top Layer Model Governing Equations Description

The IFC Top Layer model is governed by the following equations:

$$\frac{dq}{dt} = \frac{1}{\tau}\left(\frac{q}{q_r}\right)^{\lambda_1}\left(-q + c_2\left(q_{pc} + q_{sc}\right) + q_{in}(t)\right)$$

$$\frac{1}{\tau} = \frac{60 \cdot v_r \cdot \left(A_{up}/A_r\right)^{\lambda_2}}{(1 - \lambda_1) \cdot L \cdot 10^{-3}}$$

$$c_2 = A_h/60$$

$$q_r = 1$$

$$A_r = 1$$

$$\frac{ds_p}{dt} = c_1 p(t) - q_{pc} - q_{pt} - e_p$$

$$c_1 = 0.001/60$$

$$\frac{ds_t}{dt} = q_{pt} - q_{ts} - e_t$$

$$\frac{ds_s}{dt} = q_{ts} - q_{sc} - e_s$$

$$\frac{dV_p}{dt} = c_1 p(t)$$

$$\frac{dV_r}{dt} = q_{pc}$$

$$\frac{dq_b}{dt} = \frac{v_B}{L}\left(A_h q_{sc} - 60 \cdot q_b + q_{b,in}(t)\right)$$

where q(t) is the channel discharge (m^3/s) at time t, q_b(t) is the channel discharge from baseflow (m^3/s) at time t, p(t) is the precipitation rate (mm/hr) at time t, and e_{pot}(t) is the potential evaporation rate (mm/hr) at time t. Additionally, q_{in}(t) is the total discharge entering the channel from the directly upstream channels (m^3/s) at time t, while $q_{b,in}$(t) is the total discharge from baseflow entering the channel from the directly upstream channels at time t. The water column is represented by s_p for storage ponded on the surface (m), s_t for storage in the top layer (m), and s_s for storage in the subsurface (m). s_{precip}(t) is the total fallen precipitation (m^3) from time 0 to time t, and V_r(t) is the total volume of water transported as runoff (m^3) from time 0 to time t.

Water fluxes move water around the different layers of the hillslope, and other fluxes move water from the hillslope layers to the channel. Flux from ponded storage on the surface to the channel (m/min) is:

$$q_{pc} = k_2 \cdot s_p$$

Flux from ponded storage on the surface to the top layer (m/min) is:

$$q_{pt} = k_t s_p$$

$$k_t = k_2 \left(A + B \cdot \left(1 - \frac{s_t}{S_L}\right)^{\alpha} \right)$$

$$k_2 = v_h \cdot L/A_h \cdot 60 \cdot 10^{-3}$$

Flux from the top layer to the subsurface (m/min) is:

$$q_{ts} = k_i s_t$$

$$k_i = k_2 \beta$$

Flux from the subsurface to the channel (m/min) is:

$$q_{sc} = k_3 s_s$$

In addition, fluxes from evapotranspiration e_p, e_t, and e_s move water from the hillslope to the atmosphere at a rate dependent on input potential evapotranspiration, e_{pot}. These are fluxes are detailed further in Small (2015). Figure 13 illustrates general hillslope-link processes.

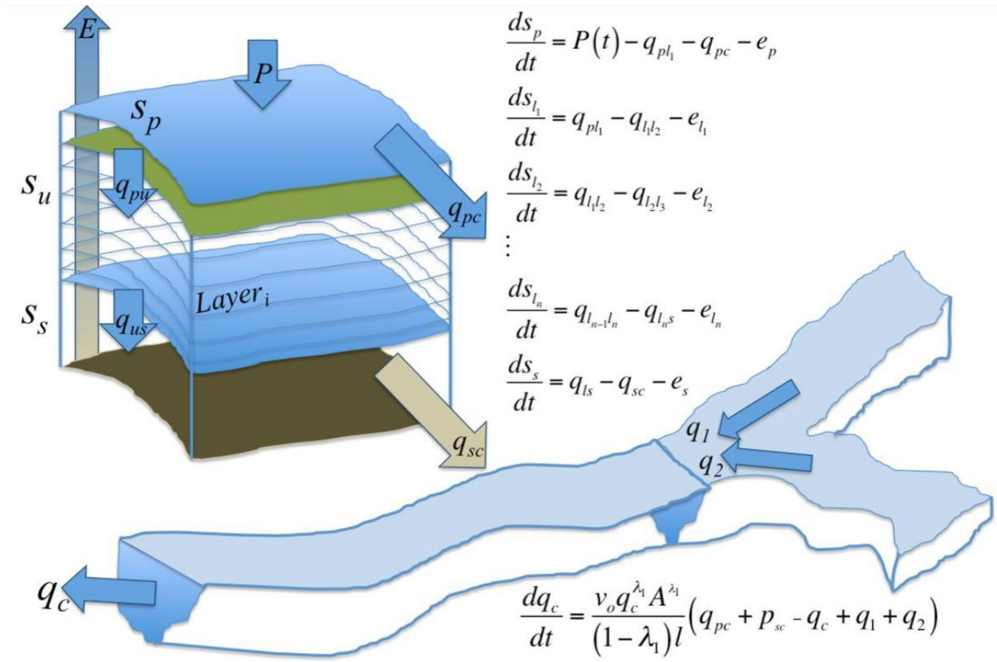

Figure 13: Decomposition of a hillslope-link unit with *n* conceptual soil layers in which water flow is governed by ODEs (Della Libera Zanchetta, 2017).

5.2.2 IFC Top Layer Model Parameters and States Description

Each hillslope-link unit is characterized by three parameters: channel length, L (km); hillslope area, A_h (km^2); and total upstream drainage area, A_{up} (km^2). All other parameters are lumped to represent the watershed globally, taking the same value at every hillslope-link unit. These global parameters are constant in time, describing channel reference velocity, v_r (m/s); exponent of channel velocity discharge, λ_1 (dimensionless); exponent of channel velocity area, λ_2 (dimensionless); constant velocity of water on the hillslope, v_h (m/s); infiltration from subsurface into the channel, k_3 (min^{-1}); percentage of percolation from top layer to subsurface, β (dimensionless); total hillslope soil depth, h_b (m); total topsoil depth, S_L (m); surface to top layer infiltration, additive factor, A (dimensionless); surface to top layer infiltration, multiplicative factor, B (dimensionless); surface to top layer infiltration, exponent factor, α (dimensionless); and channel baseflow velocity, v_B (dimensionless).

The IFC Top Layer model models a set of seven states for all hillslope-link units for a time t. Each hillslope-link unit is characterized by the volume of water transported in the channel as discharge and baseflow, ponded on the surface of the hillslope, held in the pore space of the soil top layer and subsurface, fallen as cumulative precipitation, and generated as runoff by the hillslope-link system.

5.3 Model Network Parameters Assignment & Topology Inputs

I utilized Terrain Analysis Using Digital Elevation Models (TauDEM) software to extract river networks across the main island of Puerto Rico. TauDEM incorporates DEM analysis tools and functions developed by Dr. David Tarboton over the years with support from a variety of sponsors. All raw elevation inputs were provided by the SRTM 1 arc-second global digital elevation model, which has a spatial resolution of approximately 90 meters across the main island of Puerto Rico. The process described below was completed for each of the 75 watersheds upstream of USGS streamflow gages listed in Table 1.

First, pits were removed from raw SRTM elevation grids to ensure hydraulic connectivity within each watershed. Pits are low elevation areas in DEMs that are completely surrounded by higher terrain. Pits are generally taken to be artifacts that interfere with the routing of flow across DEMs so they are removed by raising their elevation to the point where they drain off the edge of the domain (Jenson & Domingue, 1988). Figure 14 shows the result of removing these pit depressions on the SRTM-derived DEM for the watershed upstream of USGS 50035000, Río Grande de Manatí at Ciales.

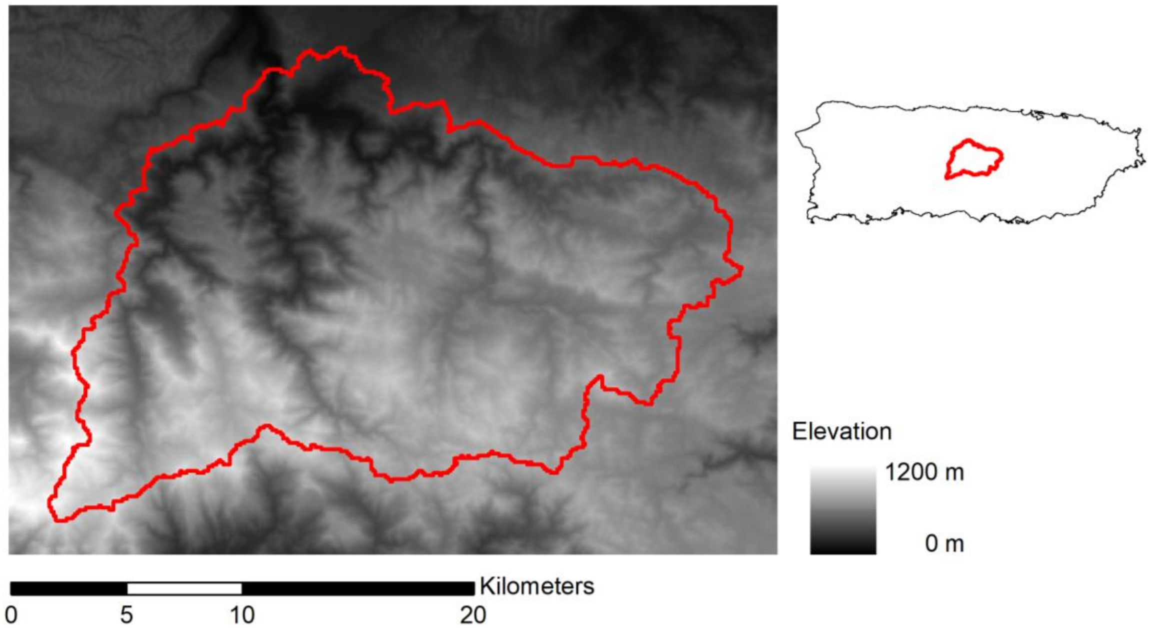

Figure 14: Pit-filled SRTM-derived DEM of the Río Grande de Manatí at Ciales watershed.

Flow directions were then assigned to DEM pixels to determine the paths of water. I used perhaps the simplest method for specifying flow directions by assigning flow from each pixel to one of its eight neighbors, either adjacent or diagonal, in the direction with steepest downward slope. This method is designated “D8” as flow can only be directed in eight directions (O’Callaghan & Mark, 1989). The D8 flow direction method has been used extensively to derive a wealth of information about the morphology of the land surface (Jenson, 1991; Tarboton, Bras, & Rodriguez-Iturbe, 1991). The D8 method produces good results in high gradient slops but it tends to produce flow in parallel lines along low steep areas (Hosseinzadeh, 2011). To increase performance in flat areas, flow directions were assigned away from higher ground and towards lower ground using the method of Garbrecht and Martz (Garbrecht & Martz, 1997). Figure 15 shows the D8 flow direction for the Río Grande de Manatí at Ciales watershed.

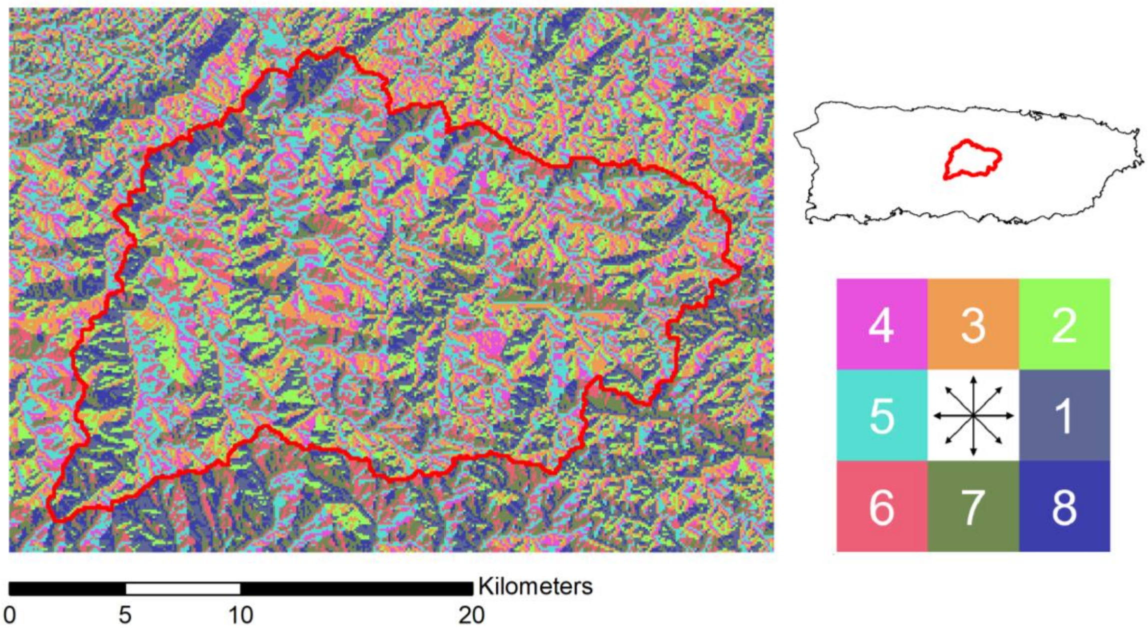

Figure 15: D8 flow direction grid of the Río Grande de Manatí at Ciales watershed.

The contributing area of terrain upslope of each grid cell was calculated by counting the number of upslope cells draining through it based on the D8 flow directions, resulting in an accumulation raster. Finally, the stream network was derived from this accumulation raster based on a defined threshold accumulation value. A low threshold accumulation value results in a very dense stream network because a link is defined everywhere that just a few pixels drain together. A high threshold accumulation value results in a coarse stream network because links are only defined where many pixels drain together. Due to the SRTM DEM’s coarse 90-meter resolution, a low threshold value was chosen, resulting in HLM models with a similar amount of sub-basins when compared to USGS stream networks defined across Puerto Rico. Figure 16 shows the HLM for the Río Grande de Manatí at Ciales watershed.

After the stream network was derived, each hillslope-link was assigned a unique value, associated with a flow direction, and ordered according to the Strahler ordering system. Cells that do not have any other grid cells draining in to them are Strahler order 1. When two or more flow paths of different order join, the Strahler order of the downstream flow path is the Strahler order of the highest incoming flow path. When two or more flow paths of equal order join, the downstream flow path is increased by one (Strahler, 1957). This is illustrated for the Río Grande de Manatí at Ciales watershed in Figure 16.

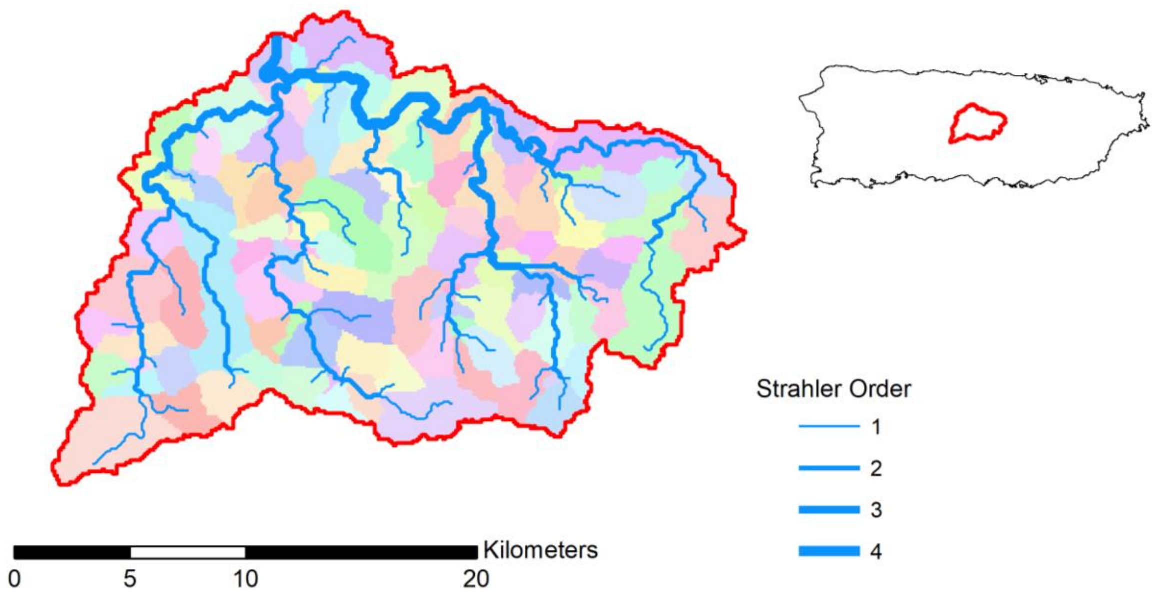

Figure 16: Hillslope-link model of the Río Grande de Manatí at Ciales watershed. Links weighted according to Strahler order.

Hillslope-link models like the one shown in Figure 16 are used to create stream network topology and network parameter files. The Iowa Flood Center Top Layer model is structured around the topology and network parameters defined by each HLM. Topology decomposes a natural stream network into a directed-tree data structure. Directed edges follow channel links in the flow direction, and tree-nodes are placed where two links meet. Network parameters describe each directed edge according to its channel length, hillslope area, and total upstream drainage area. Node connections describe how sub-basins are nested within the watershed. Figure 17 is a schematic of a sample surface drainage network decomposed into its tree topology. Figure 18 shows the processes occurring within each hillslope-link unit that routes water from hillslope storage to link transport downstream.

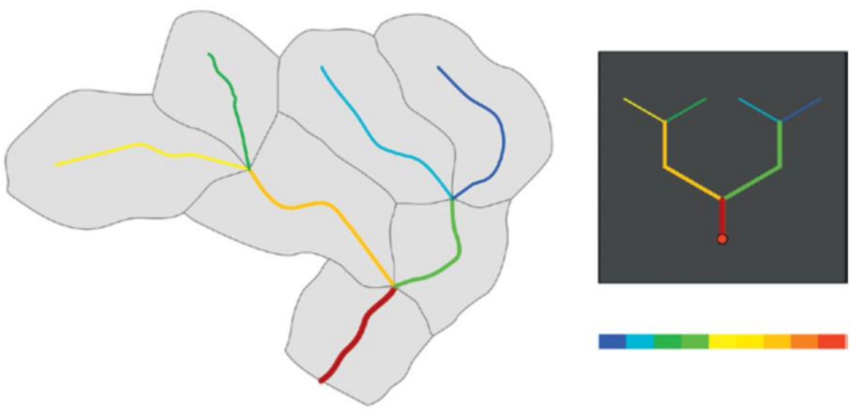

Figure 17: Landscape decomposition into hillslopes and channel links. Colored areas drain to the respective links (Krajewski et al., 2017).

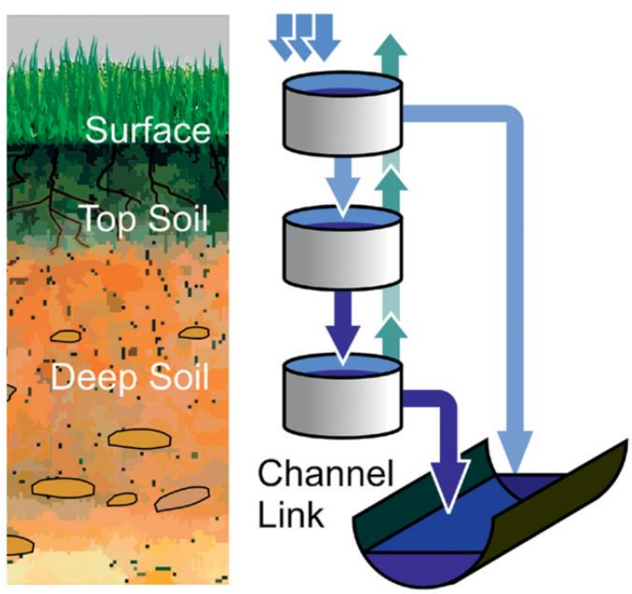

Figure 18: Hillslope-based water flux and storage accounting schematic (Krajewski et al., 2017).

5.4 Model Rainfall Inputs

IMERG Late Run data was processed to produce all rainfall inputs for this study. Ground observations from raingages or weather radar were not used to correct or calibrate IMERG Late Run rainfall estimates. Rainfall accumulation values were assigned using nearest neighbor sampling for those hillslopes that wholly fall within the footprint of a single IMERG pixel. Area-averaged values were assigned to those hillslopes split by the division between two or more IMERG pixels. Figure 19 shows a sample of IMERG Late Run rainfall data over the watershed upstream of USGS 50035000, Río Grande de Manatí at Ciales. Table 6 shows basin average monthly accumulations of rainfall as estimated by IMERG Late Run within each modelled watershed, comparing annual sums to the NOAA climate normals.

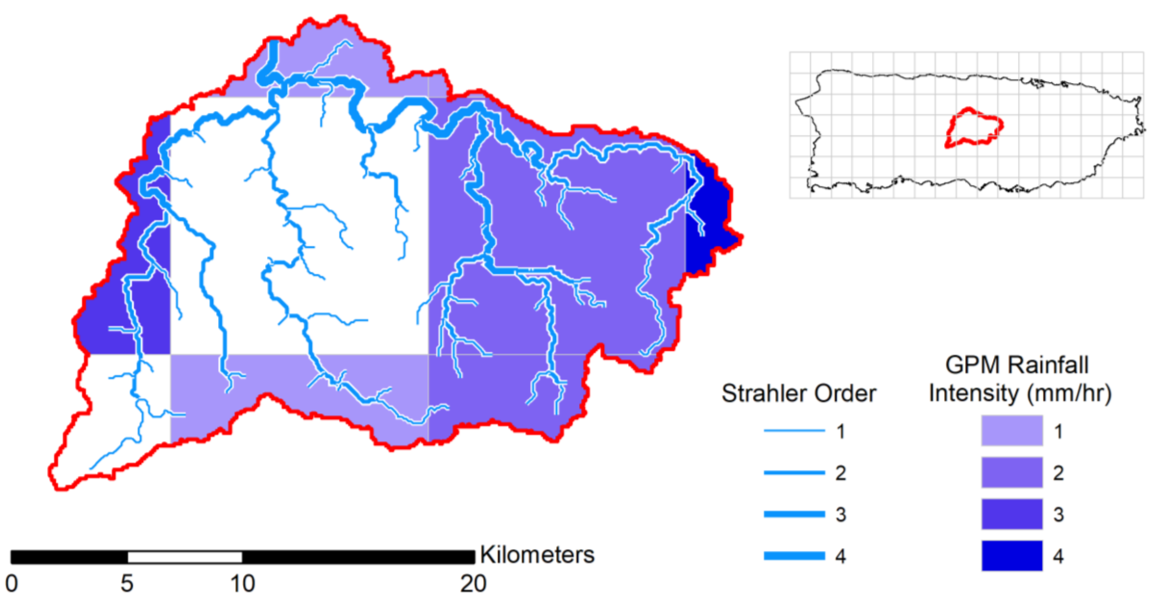

Figure 19: IMERG Late Run rainfall estimates from 12:00 PM to 12:30 PM on August 1, 2014 over the Río Grande de Manatí at Ciales watershed with stream links weighted according to Strahler order.

Table 6: Average monthly precipitation accumulations within 75 modelled watersheds in Puerto Rico estimated by IMERG Late Run

[*Study Index*, numerical identifier of each gage, created for this study; *USGS Streamgage*, numerical identifier for USGS each streamgage station located at basin outlet; *Site Name*, abbreviated name describing USGS streamgage station; *GPM Precipitation Rate Estimates*, basin-averaged monthly accumulations of IMERG Late Run rainfall estimates; *MAR*, mean annual rainfall interpolated from NOAA 30-year climate normals and averaged to each basin; *Difference*, percent difference between annual sum of basin-averaged rainfall accumulations estimated by IMERG Late Run and NOAA precipitation climate normals (negative values indicate that IMERG Late Run underestimates rainfall, while positive values indicate that IMERG Late Run overestimates rainfall)]

Index	USGS Streamgage	Site Name	GPM Precipitation Accumulation Estimates (mm)													MAR (mm)	Difference (%)
			Jan.	Feb.	Mar.	Apr.	May	Jun.	Jul.	Aug.	Sep.	Oct.	Nov.	Dec.	Total		
1	50010500	Río Guajataca at Lares	99	94	104	107	113	105	112	107	100	106	104	100	1250	1917	-42.2
4	50011200	Río Guajataca below Lago…	95	90	100	103	113	106	112	108	101	106	100	97	1232	1920	-43.7
5	50014800	Río Camuy near Bayaney	103	100	114	114	120	110	119	113	106	110	106	103	1317	1954	-38.9
6	50021700	Río Grande de Arecibo above…	116	115	129	130	136	121	127	121	112	114	113	110	1445	1911	-27.8
8	50024950	Río Grande de Arecibo below…	116	114	131	131	138	122	128	121	113	115	114	110	1453	1939	-28.6
9	50025155	Río Saliente at Coabey near…	115	114	138	135	140	126	130	121	112	113	111	105	1460	2240	-42.2
10	50026025	Río Caonillas at Paso Palma	112	109	127	126	135	121	125	118	112	113	111	106	1416	2088	-38.4
12	50027000	Río Limon above Lago Dos Bocas	120	122	143	141	147	129	132	123	115	118	115	111	1515	2001	-27.7
13	50028000	Río Tanama near Utuado	111	108	123	125	130	116	123	118	110	114	112	107	1399	1949	-32.9
14	50028400	Río Tanama at Charco Hondo	109	109	128	129	133	119	126	119	111	112	107	105	1405	2030	-36.4
15	50029000	Río Grande de Arecibo at…	112	111	130	129	136	121	126	120	112	114	111	107	1428	1997	-33.2
16	50031200	Río Grande de Manatí near…	94	88	97	100	109	104	109	108	104	106	100	97	1215	1885	-43.2
19	50034000	Río Gauta near Orocovis	104	100	115	115	122	114	117	113	105	106	106	104	1321	1985	-40.2
20	50035000	Río Grande de Manatí at Ciales	101	97	111	112	119	111	116	112	106	108	104	102	1299	1973	-41.2
21	50038100	Río Grande de Manatí at…	114	116	136	134	143	126	128	120	113	118	113	109	1471	1733	-16.4
23	50038320	Río Cibuco below Corozal	107	102	110	117	128	114	120	117	115	119	111	109	1369	1927	-33.8
24	50039500	Río Cibuco at Vega Baja	106	101	115	116	127	115	121	117	112	115	108	106	1360	1876	-31.9
25	50039995	Río Carité at spillway	110	113	132	131	133	120	126	125	117	116	112	108	1444	1745	-18.9
26	50043000	Río de la Plata at Proyecto La…	103	100	110	113	120	113	121	122	114	116	110	106	1348	1667	-21.1
27	50043197	Río Usabón at Highway 162…	86	76	80	85	96	93	102	105	97	104	98	95	1115	1639	-38.1
28	50043800	Río de la Plata at Comerio	97	94	101	104	113	108	115	116	109	113	106	102	1278	1659	-25.9

Table 6 – Continued

Index	USGS Streamgage	Site Name	GPM Precipitation Accumulation Estimates (mm)													MAR (mm)	Difference (%)
			Jan.	Feb.	Mar.	Apr.	May	Jun.	Jul.	Aug.	Sep.	Oct.	Nov.	Dec.	Total		
29	50044810	Río Guadiana near Guadiana	105	106	114	115	127	118	123	121	116	118	114	109	1386	1834	-27.8
30	50045010	Río de la Plata below La Plata…	100	96	104	107	116	109	118	118	111	114	107	104	1304	1695	-26.1
31	50046000	Río de la Plata at Highway 2…	101	97	106	108	118	110	118	118	111	114	107	104	1312	1711	-26.4
32	50047535	Río de Bayamón at Arenas	99	99	110	115	120	109	122	125	118	116	103	101	1338	1674	-22.3
34	50047560	Río de Bayamón below Lago de…	90	85	92	94	107	99	110	113	106	107	98	97	1199	1671	-32.8
35	50047850	Río de Bayamón near Bayamón	105	103	113	117	128	116	125	125	117	119	111	109	1388	1735	-22.2
36	50049100	Río Piedras at Hato Rey	93	85	86	92	105	101	107	110	104	105	97	96	1180	1781	-40.6
38	50050900	Río Grande de Loíza at…	101	103	109	112	121	111	120	121	112	119	113	107	1348	2023	-40.1
39	50051310	Río Cayaguas at Cerro Gordo	98	95	103	113	117	112	125	127	120	125	117	107	1360	2245	-49.1
40	50051800	Río Grande de Loíza at Highway…	97	93	102	107	115	110	119	121	114	118	111	103	1309	2154	-48.8
41	50053025	Río Turabo above Borinquen	99	94	103	106	115	105	112	114	108	109	100	98	1264	1867	-38.5
42	50055000	Río Grande de Loíza at Caguas	96	91	96	101	112	105	116	118	112	115	107	103	1272	1995	-44.3
43	50055225	Río Caguitas at Villa Blanca at…	95	94	100	102	114	106	114	112	104	108	104	102	1255	1763	-33.7
44	50055380	Río Bairoa bove Abiroa, Caguas	94	91	101	103	113	106	115	111	103	106	100	98	1241	1770	-35.1
45	50055750	Río Gurabo below El Mango	100	98	110	113	124	116	129	128	118	116	110	107	1371	2100	-42.0
46	50056400	Río Valenciano near Juncos	93	87	95	101	111	105	115	115	110	110	106	102	1250	2030	-47.6
47	50057000	Río Gurabo at Gurabo	95	90	97	102	114	108	120	120	112	112	107	104	1279	1975	-42.7
48	50058350	Río Canas at Río Canas	94	87	91	96	109	101	112	114	105	109	103	104	1224	1774	-36.7
49	50059050	Río Grande de Loíza below…	98	94	101	106	117	109	119	120	112	113	108	104	1302	1920	-38.4
50	50059210	Quebrada Grande at Barrio Dos…	104	102	108	117	128	117	124	123	117	121	115	111	1387	1791	-25.4
51	50061800	Río Canovanas near Campo Rico	114	118	138	139	145	130	139	133	121	120	116	111	1523	2007	-27.5
52	50063800	Río Espíritu Santo near Río…	107	105	131	134	139	122	132	128	117	115	107	105	1442	2133	-38.6
53	50064200	Río Grande near El Verde	108	110	126	130	132	121	134	133	122	120	115	109	1459	2117	-36.8
54	50065500	Río Mameyes near Sabana	100	96	116	122	130	118	123	121	112	112	103	100	1352	2273	-50.8
55	50067000	Río Sabana at Sabana	103	101	116	120	130	118	123	122	113	110	102	99	1356	2209	-47.8
56	50070900	Río Fajardo at Paraíso near…	101	99	113	116	126	118	124	124	113	111	106	103	1352	2378	-55.0
57	50071000	Río Fajardo near Fajardo	99	97	110	114	125	116	122	122	111	110	104	102	1333	2325	-54.2
58	50075000	Río Icacos near Naguabo	88	80	108	112	113	105	113	116	105	102	100	91	1235	2406	-64.4

Table 6 – Continued

Index	USGS Streamgage	Site Name	GPM Precipitation Accumulation Estimates (mm)													MAR (mm)	Difference (%)
			Jan.	Feb.	Mar.	Apr.	May	Jun.	Jul.	Aug.	Sep.	Oct.	Nov.	Dec.	Total		
60	50081000	Río Humacao at Las Piedras	97	92	102	111	110	108	123	126	118	119	114	107	1327	2098	-45.0
61	50083500	Río Guayanés near Yabucoa	102	98	113	122	131	119	127	126	117	117	111	107	1389	1983	-35.2
62	50085100	Río Guayanés at Central Roig	106	105	107	113	130	124	133	138	130	127	120	117	1449	2083	-35.9
63	50090500	Río Maunabo at Lizas	105	106	129	129	135	121	129	126	115	116	112	107	1431	1891	-27.7
64	50092000	Río Grande de Patillas near…	110	113	128	127	134	125	132	129	119	121	118	117	1473	1744	-16.8
65	50093000	Río Marín near Patillas	114	115	136	137	144	127	132	126	116	118	113	112	1489	1809	-19.4
67	50093120	Río Grande de Patillas below…	110	111	127	127	134	123	130	127	118	120	117	115	1460	1744	-17.8
70	50100200	Río Lapa near Rabo del Buey	91	82	81	90	107	108	112	115	109	115	110	104	1223	1558	-24.0
71	50100450	Río Majada at la Plena	107	102	107	114	131	124	131	129	121	123	119	116	1423	1716	-18.7
72	50106100	Río Coamo at Highway 14…	92	81	81	93	111	106	108	108	105	111	108	103	1208	1576	-26.4
74	50110650	Río Jacaguas above Lago…	92	78	84	92	104	103	108	106	99	102	101	98	1169	1943	-49.8
75	50110900	Río Toa Vaca above Lago…	100	91	95	101	115	109	114	111	106	111	112	107	1271	1845	-36.9
78	50111500	Río Jacaguas at Juana Díaz	92	80	85	92	105	102	106	105	100	105	103	99	1176	1726	-37.9
79	50112500	Río Inabón at Real Abajo	117	114	128	132	133	122	127	121	112	111	114	115	1445	2114	-37.6
80	50113800	Río Cerrillos above Lago…	120	120	138	140	143	126	132	125	114	115	115	113	1501	1924	-24.7
82	50114000	Río Cerrillos below Lago…	119	119	135	138	141	126	131	124	114	115	116	114	1493	1877	-22.8
83	50114900	Río Portugues near Tibes	120	118	134	137	143	126	131	123	114	115	116	115	1492	1750	-15.9
84	50115240	Río Portugues at Parque...	116	109	118	124	133	120	124	117	109	112	114	111	1407	1693	-18.4
85	50124200	Río Guayanilla near Guayanilla	99	86	90	102	114	105	109	107	104	109	109	103	1236	1528	-21.1
86	50126150	Río Yauco above Diversión…	110	104	115	122	132	117	122	116	109	112	113	110	1383	1500	-8.1
87	50129254	Río Loco at Las Latas near La…	91	77	80	97	110	106	108	108	106	112	103	99	1195	1322	-10.1
88	50136400	Río Rosario near Hormigueros	122	125	147	145	152	134	137	131	121	123	121	117	1575	1984	-23.0
89	50138000	Río Guanajibo near Hormigueros	98	92	100	109	122	112	117	116	109	114	108	102	1299	1710	-27.3
90	50144000	Río Grande de Añasco near San…	119	119	137	139	143	127	133	125	116	119	118	114	1509	1888	-22.3
92	50147800	Río Culebrinas at Highway 404…	90	83	92	99	109	105	112	108	101	104	98	94	1196	1811	-40.9
93	50148890	Río Culebrinas at Margarita…	87	80	88	94	105	102	109	106	100	102	96	91	1160	1797	-43.1

5.5 Model Evapotranspiration Inputs

Between 2000 and 2014, approximately 700 MOD16A2 near global datasets were released. They provide estimates of ET at 0.5-km spatial resolution every 8 days. I processed these 8-day datasets into a spatially distributed set of monthly ET rates for each of the 180 months spanning January 2000 to December 2014. Figure 20 shows the result of this processing for August 2014 over the Río Grande de Manatí at Ciales watershed. I then calculated the average over each modelled watershed to assign one monthly value representing the ET rate for each month. Lastly, each monthly rate of ET was compared to others of the same month but different years. I calculated a final representative rate of monthly ET in each watershed from the 15 values for January, then repeated the process for the remaining 11 months. A summary of monthly ET rates for each watershed is shown in Table 7.

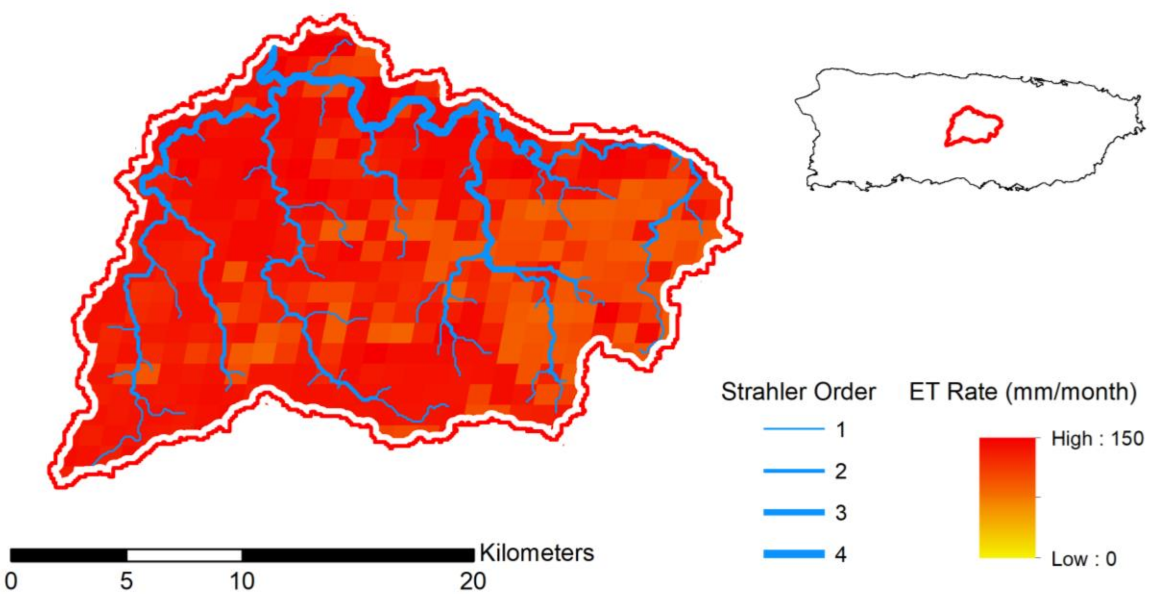

Figure 20: Average evapotranspiration rate during August 2014 within Río Grande de Manatí at Ciales watershed with rates estimated by the MOD16A2 algorithm and stream links weighted according to Strahler order.

Table 7: Average monthly evapotranspiration rates over 75 modelled watersheds in Puerto Rico estimated by MOD16A2.

[*Study Index*, numerical identifier of each gage, created for this study; *USGS Streamgage*, numerical identifier for USGS each streamgage station located at basin outlet; *Site Name*, name describing USGS streamgage station; *MODIS Evapotranspiration Rate Estimates*, average ET for each month of the year calculated from MOD16A2 algorithm estimates]

Index	USGS Streamgage	Site Name	MODIS Evapotranspiration Rate Estimates (mm/month)											
			Jan.	Feb.	Mar.	Apr.	May	Jun.	Jul.	Aug.	Sep.	Oct.	Nov.	Dec.
1	50010500	Río Guajataca at Lares	99	94	104	107	113	105	112	107	100	106	104	100
4	50011200	Río Guajataca below Lago Guajataca	95	90	100	103	113	106	112	108	101	106	100	97
5	50014800	Río Camuy near Bayaney	103	100	114	114	120	110	119	113	106	110	106	103
6	50021700	Río Grande de Arecibo above Utuado	116	115	129	130	136	121	127	121	112	114	113	110
8	50024950	Río Grande de Arecibo below Utuado	116	114	131	131	138	122	128	121	113	115	114	110
9	50025155	Río Saliente at Coabey near Jayuyu	115	114	138	135	140	126	130	121	112	113	111	105
10	50026025	Río Caonillas at Paso Palma	112	109	127	126	135	121	125	118	112	113	111	106
12	50027000	Río Limon above Lago Dos Bocas	120	122	143	141	147	129	132	123	115	118	115	111
13	50028000	Río Tanama near Utuado	111	108	123	125	130	116	123	118	110	114	112	107
14	50028400	Río Tanama at Charco Hondo	109	109	128	129	133	119	126	119	111	112	107	105
15	50029000	Río Grande de Arecibo at Central Cambalache	112	111	130	129	136	121	126	120	112	114	111	107
16	50031200	Río Grande de Manatí near Morovis	94	88	97	100	109	104	109	108	104	106	100	97
19	50034000	Río Gauta near Orocovis	104	100	115	115	122	114	117	113	105	106	106	104
20	50035000	Río Grande de Manatí at Ciales	101	97	111	112	119	111	116	112	106	108	104	102
21	50038100	Río Grande de Manatí at Highway 2 near Manatí	114	116	136	134	143	126	128	120	113	118	113	109
23	50038320	Río Cibuco below Corozal	107	102	110	117	128	114	120	117	115	119	111	109
24	50039500	Río Cibuco at Vega Baja	106	101	115	116	127	115	121	117	112	115	108	106
25	50039995	Río Carité at spillway	110	113	132	131	133	120	126	125	117	116	112	108
26	50043000	Río de la Plata at Proyecto La Plata	103	100	110	113	120	113	121	122	114	116	110	106
27	50043197	Río Usabón at Highway 162 near Barranquitas	86	76	80	85	96	93	102	105	97	104	98	95
28	50043800	Río de la Plata at Comerio	97	94	101	104	113	108	115	116	109	113	106	102
29	50044810	Río Guadiana near Guadiana	105	106	114	115	127	118	123	121	116	118	114	109
30	50045010	Río de la Plata below La Plata damsite	100	96	104	107	116	109	118	118	111	114	107	104
31	50046000	Río de la Plata at Highway 2 near Toa Alta	101	97	106	108	118	110	118	118	111	114	107	104

Table 7 – Continued

Index	USGS Streamgage	Site Name	MODIS Evapotranspiration Rate Estimates (mm/month)											
			Jan.	Feb.	Mar.	Apr.	May	Jun.	Jul.	Aug.	Sep.	Oct.	Nov.	Dec.
32	50047535	Río de Bayamón at Arenas	99	99	110	115	120	109	122	125	118	116	103	101
34	50047560	Río de Bayamón below Lago de Cidra Dam	90	85	92	94	107	99	110	113	106	107	98	97
35	50047850	Río de Bayamón near Bayamón	105	103	113	117	128	116	125	125	117	119	111	109
36	50049100	Río Piedras at Hato Rey	93	85	86	92	105	101	107	110	104	105	97	96
38	50050900	Río Grande de Loíza at Quebrada Arenas	101	103	109	112	121	111	120	121	112	119	113	107
39	50051310	Río Cayaguas at Cerro Gordo	98	95	103	113	117	112	125	127	120	125	117	107
40	50051800	Río Grande de Loíza at Highway 183 San Lorenzo	97	93	102	107	115	110	119	121	114	118	111	103
41	50053025	Río Turabo above Borinquen	99	94	103	106	115	105	112	114	108	109	100	98
42	50055000	Río Grande de Loíza at Caguas	96	91	96	101	112	105	116	118	112	115	107	103
43	50055225	Río Caguitas at Villa Blanca at Caguas	95	94	100	102	114	106	114	112	104	108	104	102
44	50055380	Río Bairoa bove Abiroa, Caguas	94	91	101	103	113	106	115	111	103	106	100	98
45	50055750	Río Gurabo below El Mango	100	98	110	113	124	116	129	128	118	116	110	107
46	50056400	Río Valenciano near Juncos	93	87	95	101	111	105	115	115	110	110	106	102
47	50057000	Río Gurabo at Gurabo	95	90	97	102	114	108	120	120	112	112	107	104
48	50058350	Río Canas at Río Canas	94	87	91	96	109	101	112	114	105	109	103	104
49	50059050	Río Grande de Loíza below Loíza damsite	98	94	101	106	117	109	119	120	112	113	108	104
50	50059210	Quebrada Grande at Barrio Dos Bocas	104	102	108	117	128	117	124	123	117	121	115	111
51	50061800	Río Canovanas near Campo Rico	114	118	138	139	145	130	139	133	121	120	116	111
52	50063800	Río Espíritu Santo near Río Grande	107	105	131	134	139	122	132	128	117	115	107	105
53	50064200	Río Grande near El Verde	108	110	126	130	132	121	134	133	122	120	115	109
54	50065500	Río Mameyes near Sabana	100	96	116	122	130	118	123	121	112	112	103	100
55	50067000	Río Sabana at Sabana	103	101	116	120	130	118	123	122	113	110	102	99
56	50070900	Río Fajardo at Paraíso near Fajardo	101	99	113	116	126	118	124	124	113	111	106	103
57	50071000	Río Fajardo near Fajardo	99	97	110	114	125	116	122	122	111	110	104	102
58	50075000	Río Icacos near Naguabo	88	80	108	112	113	105	113	116	105	102	100	91
60	50081000	Río Humacao at Las Piedras	97	92	102	111	110	108	123	126	118	119	114	107
61	50083500	Río Guayanés near Yabucoa	102	98	113	122	131	119	127	126	117	117	111	107
62	50085100	Río Guayanés at Central Roig	106	105	107	113	130	124	133	138	130	127	120	117

Table 7 – Continued

Index	USGS Streamgage	Site Name	MODIS Evapotranspiration Rate Estimates (mm/month)											
			Jan.	Feb.	Mar.	Apr.	May	Jun.	Jul.	Aug.	Sep.	Oct.	Nov.	Dec.
63	50090500	Río Maunabo at Lizas	105	106	129	129	135	121	129	126	115	116	112	107
64	50092000	Río Grande de Patillas near Patillas	110	113	128	127	134	125	132	129	119	121	118	117
65	50093000	Río Marín near Patillas	114	115	136	137	144	127	132	126	116	118	113	112
67	50093120	Río Grande de Patillas below Lago Patillas	110	111	127	127	134	123	130	127	118	120	117	115
70	50100200	Río Lapa near Rabo del Buey	91	82	81	90	107	108	112	115	109	115	110	104
71	50100450	Río Majada at la Plena	107	102	107	114	131	124	131	129	121	123	119	116
72	50106100	Río Coamo at Highway 14 at Coamo	92	81	81	93	111	106	108	108	105	111	108	103
74	50110650	Río Jacaguas above Lago Guayabal	92	78	84	92	104	103	108	106	99	102	101	98
75	50110900	Río Toa Vaca above Lago Toa Vaca	100	91	95	101	115	109	114	111	106	111	112	107
78	50111500	Río Jacaguas at Juana Díaz	92	80	85	92	105	102	106	105	100	105	103	99
79	50112500	Río Inabón at Real Abajo	117	114	128	132	133	122	127	121	112	111	114	115
80	50113800	Río Cerrillos above Lago Cerrillos near Ponce	120	120	138	140	143	126	132	125	114	115	115	113
82	50114000	Río Cerrillos below Lago Cerrillos near Ponce	119	119	135	138	141	126	131	124	114	115	116	114
83	50114900	Río Portugues near Tibes	120	118	134	137	143	126	131	123	114	115	116	115
84	50115240	Río Portugues at Parque Ceremonial Tibes	116	109	118	124	133	120	124	117	109	112	114	111
85	50124200	Río Guayanilla near Guayanilla	99	86	90	102	114	105	109	107	104	109	109	103
86	50126150	Río Yauco above Diversión Monserrate near Yauco	110	104	115	122	132	117	122	116	109	112	113	110
87	50129254	Río Loco at Las Latas near La Joya near Guanica	91	77	80	97	110	106	108	108	106	112	103	99
88	50136400	Río Rosario near Hormigueros	122	125	147	145	152	134	137	131	121	123	121	117
89	50138000	Río Guanajibo near Hormigueros	98	92	100	109	122	112	117	116	109	114	108	102
90	50144000	Río Grande de Añasco near San Sebastián	119	119	137	139	143	127	133	125	116	119	118	114
92	50147800	Río Culebrinas at Highway 404 near Moca	90	83	92	99	109	105	112	108	101	104	98	94
93	50148890	Río Culebrinas at Margarita damsite near Aguada	87	80	88	94	105	102	109	106	100	102	96	91

This process was also completed to find a representative monthly time series of ET rate over the entire main island of Puerto Rico. Figure 21 shows how these island-wide average ET rates vary month-to-month over 15 years. A statistical summary of average monthly ET rates is presented in Table 8.

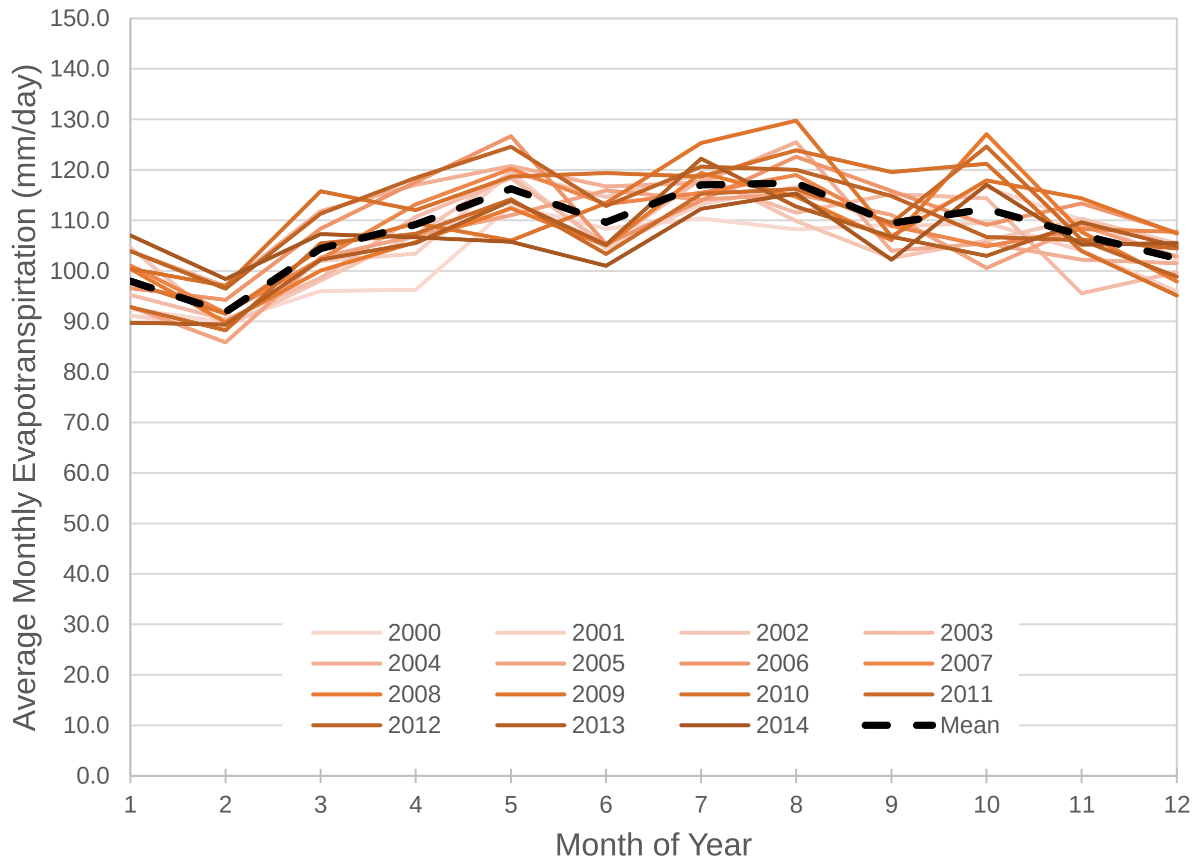

Figure 21: Spatially averaged monthly evapotranspiration rates on the main island of Puerto Rico estimated by MOD16A2, from 2000 to 2014. Mean values are shown in black.

Evapotranspiration is included in the IFC Top Layer model as daily (mm/day) or monthly (mm/month) ET rates within forcing files. The model calculates equivalent rates at specified time step increments (mm/ 5 min) from input tables of ET rate. Monthly average ET rates do not vary year-to-year unless the ET forcing files are manually changed to do so.

Table 8: Statistical summary of spatially averaged monthly evapotranspiration rates on the main island of Puerto Rico, from 2000 to 2014.

Month		Minimum	Maximum	Median	Mean	Standard Deviation
January	(mm/month)	89.7	107.0	97.8	98.0	5.5
February	(mm/month)	85.8	98.4	90.4	91.9	3.8
March	(mm/month)	96.0	115.8	102.7	104.4	5.6
April	(mm/month)	96.3	118.4	107.4	109.2	5.9
May	(mm/month)	105.7	126.7	118.4	116.3	6.1
June	(mm/month)	101.0	119.4	108.4	109.6	5.8
July	(mm/month)	110.4	125.3	117.5	117.1	4.0
August	(mm/month)	108.2	129.8	116.2	117.4	6.0
September	(mm/month)	102.2	119.6	108.9	109.4	5.1
October	(mm/month)	100.6	127.1	109.5	112.3	8.2
November	(mm/month)	95.6	114.4	107.8	107.1	4.7
December	(mm/month)	95.1	107.8	102.8	102.5	4.2

5.6 Model Global Parameters Assignment

Each modelled watershed is assigned a set of global parameters that influence the calculation of water transport processes the same way in all hillslope-link units. I analyzed the basin characteristics and local data summarized in Chapter 3.3 to create an island-wide model for Puerto Rico. Although each watershed could be calibrated to fit observations month-to-month, the performance of this island-wide model provides insight into how ungauged basins developing communities could benefit from satellite-driven hydrologic models. As such, the set of global parameters described here represents a best guess approximation of watershed behavior across the island, rather than a set of 75 watershed-scale calibrations of the IFC Top Layer model.

Using the entire record of USGS in-situ streamflow measurements, I explored the relationship of water flow velocity to discharge and drainage area across river networks in Puerto Rico. This relationship may be organized as a power law model that describes the river flow velocity across the network with increasing discharge and drainage area, the context of which forms the basis for many routing models, including the IFC Top Layer model (Ayalew, Krajewski, & Mantilla, 2014; Ghimire, Krajewski, & Mantilla, 2018). It has the form:

$$v_c = v_r Q^{\lambda_1} A^{\lambda_2}$$

where v_c is the channel velocity and Q is the corresponding flowrate for a given watershed of drainage area, A. In addition, v_r is the channel reference velocity, λ_1 is the exponent of channel velocity discharge, and λ_2 is the exponent of channel velocity area, which directly correspond to IFC Top Layer model global parameters.

I used 1604 measurements of the mean cross-sectional velocity and the concurrent discharge for basins of variable drainage area to estimate these three parameters. Figure 22 shows the ensemble of all state-wide velocity and discharge data used to fit the power law model to Puerto Rico streamflow conditions. In addition, power law fits are shown for six drainage areas ranging from 10 km^2 to 500km^2. The results of this island-wide power law model fit show that appropriate values for channel velocity discharge, exponent of channel velocity discharge, and the exponent of channel velocity area are 0.509 m/s, 0.316, and -0.090, respectively. The model explains about 53% of the variability in stream velocities (R^2 = 0.53), with a root-mean-square error (RMSE) value of 0.19 m/s.

I chose to increase the channel velocity discharge because many data points were recorded in coastal lowlands, where river gradients and average flow velocities are low. The chosen island-wide streamflow velocity power law model is:

$$v_c = 0.710 Q^{0.316} A^{-0.090}$$

By increasing channel velocity above the calculated power law model fit, streamflow will be better simulated in the interior mountain region that is most affected by floods.

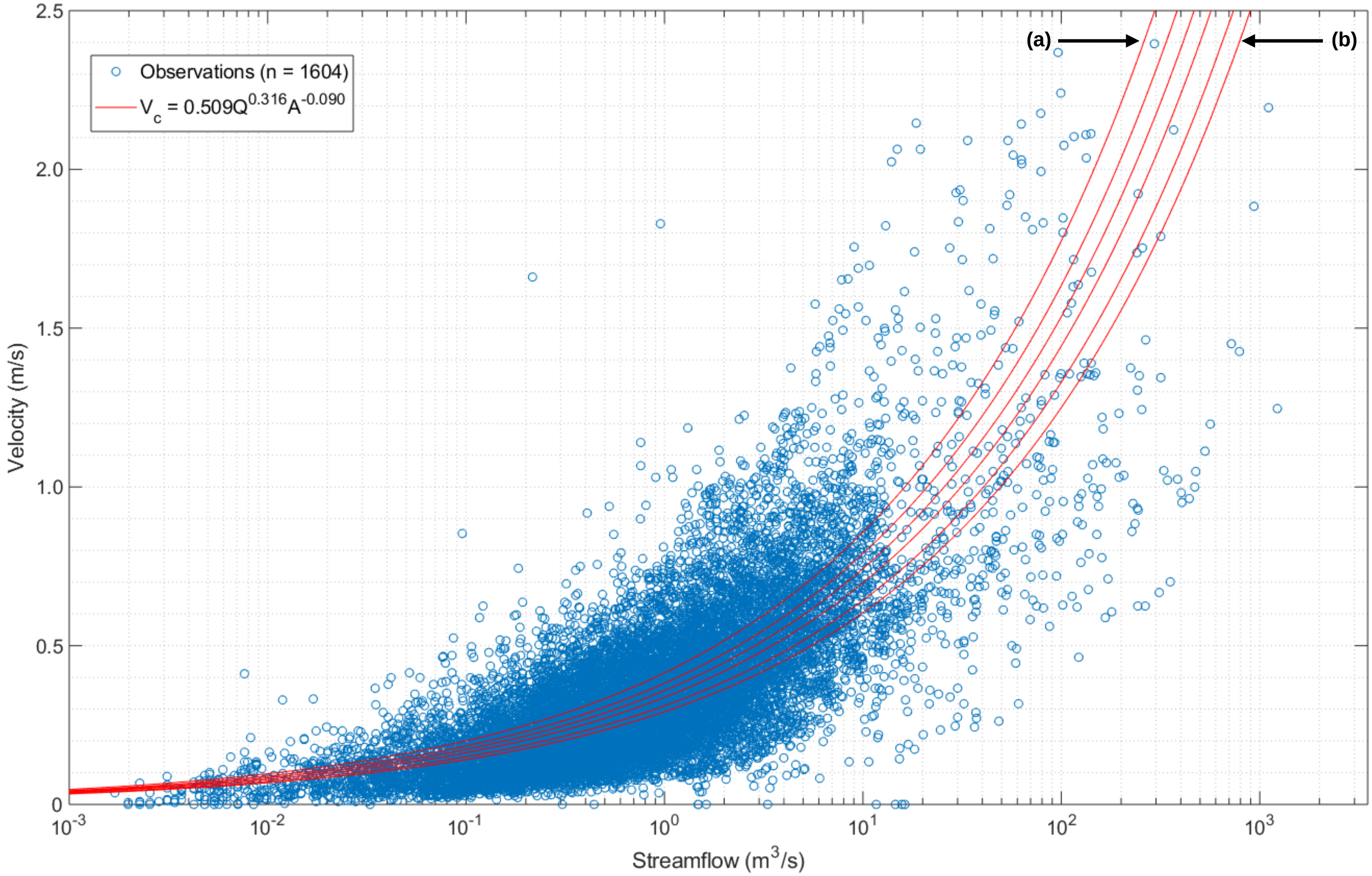

Figure 22: Island-wide power law river velocity model, where (a) corresponds to the model with drainage area 10 km^2 and (b) corresponds to the drainage area of 500 km^2, and the intermediate lines correspond to the drainage areas of 25, 50, 100, and 250 km^2, respectively, from (a) to (b).

The remaining global parameters were assigned the following values for all 75 modelled watersheds in Puerto Rico:

v_h = 0.15 m/s

k_3 = 8.00e-7 min^{-1}

β = 3.00 %

h_b = $0.1 \cdot DR$ m

S_L = DR m

A = 0.00 (dimensionless)

B = 99.00 (dimensionless)

α = 3.00 (dimensionless)

v_B = 1.00 m/s

where *DR* is the basin average maximum depth of soil, summarized in Table 1.

5.7 Model Operation

5.7.1 Initial Conditions and Time Scale

To minimize the influence of initial conditions on long term model performance, I decided to operate the IFC Top Layer model continuously for the 75 modelled basins in Puerto Rico from March 2014 to December 2018. Representative initial conditions were chosen once for each basin at the start of model runs. USGS procedures were followed to establish mean monthly streamflow rates normalized to drainage area. Over 640,000 values of daily mean streamflow from USGS historical records spanning October 1, 1985 to December 31, 2018 of were analyzed. This pool of data was gathered only from streamgages corresponding to the 75 modelled watersheds. Values of mean daily streamflow per unit area were averaged based on the month in which they fall, resulting in the values shown in Table 9.

Table 9: Mean monthly streamflow per unit area

Month		Mean	Standard Deviation	Count
January	$[m^3/s]/km^2$	0.79	1.73	55358
February	$[m^3/s]/km^2$	0.57	1.05	50512
March	$[m^3/s]/km^2$	0.56	1.41	53832
April	$[m^3/s]/km^2$	0.81	2.20	52075
May	$[m^3/s]/km^2$	1.27	2.70	53928
June	$[m^3/s]/km^2$	0.94	1.75	52325
July	$[m^3/s]/km^2$	0.93	1.88	54101
August	$[m^3/s]/km^2$	1.23	3.13	54143
September	$[m^3/s]/km^2$	2.21	12.41	52392
October	$[m^3/s]/km^2$	1.78	4.38	55280
November	$[m^3/s]/km^2$	1.72	3.51	53489
December	$[m^3/s]/km^2$	1.07	2.26	55349

The March value was substituted for streamflow initial conditions at the beginning of each model run with corresponding baseflow values equal to 75% of average flow, a portioning consistent with studies of watersheds in the interior mountain region (Rodríquez-Martínez & Santiago, 2016). Because storms do not follow a calendar, runs were not terminated until at least 24 hours after the last observation of rain by IMERG Late Run within each watershed, allowing for the full hydrologic response to be simulated and compared to streamgage observations.

5.7.2 Numerical Solver & Computational Resources

Mathematically, the IFC Top Layer model is a system of ordinary differential equations organized according to network topology, as described in Chapter 5.2. Processes within each hillslope unit are calculated independently because there is no "communication" between hillslopes, only between hillslopes and their nearby link. Calculations for the model are performed using the asynchronous (ASYNCH) software package developed by the IFC. ASYNCH is a parallel solver for systems of differential equations interconnected in a tree structure (Small et al., 2012). The model applies continuous-output Runge-Kutta methods to the equations at each hillslope, allowing for asynchronous time stepping. ASYNCH is implemented in C programming language and uses Message Passing Interface (MPI) to support its parallel computing architecture. ASYNCH is capable of running on personal computers, though its full potential is reached when executed on Argon, the University of Iowa's High Performance Computing (HPC) cluster. I relied on these computational resources to efficiently simulate streamflow for 2,584 hillslope-link units for approximately 500,000 time steps each.

ASYNCH's primary input file is the "global file" that summarizes references for all others, including river network topology and HLM parameters (see Chapter 5.3), rainfall forcing (see Chapter 5.4), evapotranspiration forcing (see Chapter 5.5), and initial conditions (see Chapter 5.7.1). The global file specifies network-wide global parameters (see Chapter 5.6) in addition to specifications for the numerical solver including absolute and relative error tolerances. ASYNCH's file/database-based Unix command line system allows for extraordinary flexibility (Della Libera Zanchetta, 2017). ASYCH does not provide tools for model analysis and post-processing. I wrote my own scripts to utilize HPC resources and evaluate model performance.

CHAPTER 6: MODEL EVALUATION AND CONCLUSIONS

6.1 Introduction

Model simulations spanning 58 months were evaluated for 54 of the 75 modelled watersheds. 21 watershed models were omitted because they are affected by large upstream control structures like dams and reservoirs or measure flow directly downstream of large urban areas. For example, the simulations of the watershed upstream of USGS 50093120 Río Grande de Patillas below Lago Patillas was not analyzed because flow is largely controlled by PREPA's operation of the Patillas Dam. As discussed in Chapter 6.2, two primary statistical performance measures were selected to evaluate model performance: Nash-Sutcliffe efficiency (NSE) and Kling-Gupta efficiency (KGE), which are detailed in Chapter 6.2. Some critical sources of error influencing model performance are discussed in in Chapter 6.3, while model runs using raingage forcing are presented in Chapter 6.4 in order to help elucidate how model performance can be improved.

6.2 Model Performance

Nash-Sutcliffe efficiency is an alternative goodness-of-fit index to a standard correlation coefficient that can be calculated as:

$$NSE = 1 - \left[\frac{\sum_{i=1}^{n}(X_i - Y_i)^2}{\sum_{i=1}^{n}\left(X_i - \overline{X}\right)^2}\right]$$

where X_i is the ith observation of streamflow, Y_i is the ith simulated value of streamflow, and $\overline{X}$ is the mean of observed streamflow data, and n is the number of corresponding pairs of simulated and observed values. NSE can range from $-\infty$ to 1, with values above zero indicating predictive performance better than the mean of observations. NSE has a variety of applications including the calibration and verification of catchment model parameters, evaluation of storm event models, assessment of sediment transport models, and evaluation of state-wide flood models (Erpul, Norton, & Gabriels, 2003; Kalin, Govindaraju, & Hantush, 2003; Krajewski et al., 2017). In fact, the American Society of Civil Engineers (ASCE) Watershed Management Committee recommends the NSE for evaluation of continuous moisture accounting models (American Society of Civil Engineers, 1993). The use of the index for a wide variety of model types indicates its flexibility as a goodness-of-fit statistic (McCuen, Knight, & Cutter, 2006). Monthly mean and overall NSE values are shown in Table 10 and Figure 23, respectively.

Kling-Gupta Efficiency is a decomposition of NSE which facilitates the analysis of the relative importance of its different components in the context of hydrological modelling that can be calculated as:

$$KGE = 1 - \sqrt{(r-1)^2 + (\beta - 1)^2 + (\gamma - 1)^2}$$

where r is the Pearson product-moment correlation coefficient, β is the ratio between the mean of simulated values of streamflow and the mean of streamflow observations, and γ is the ratio between the coefficient of variation (CV) of the simulated values of streamflow to the CV of streamflow observations. Monthly mean and overall KGE values are shown in Table 11 and Figure 24, respectively.

The ideal value of the Pearson product-moment correlation coefficient, $r = 1$ and it may be calculated as:

$$r = \frac{\sum_{i=1}^{n}\left((X_i - \overline{X})(Y_i - \overline{Y})\right)}{\sqrt{\sum_{i=1}^{n}(X_i - \overline{X})^2 \sum_{i=1}^{n}(Y_i - \overline{Y})^2}}$$

where X_i is the ith observation of streamflow, Y_i is the ith simulated value of streamflow, and $\overline{X}$ is the mean of observed streamflow data, $\overline{Y}$ is the mean of simulated values of streamflow, and n is the number of corresponding pairs of simulated and observed values. This component indicates the correlation of observations and simulation of streamflow. Monthly mean and overall r values are shown in Table 12 and Figure 25, respectively.

The ideal value of the ratio between the mean of simulated values of streamflow and the mean of streamflow observations, $\beta = 1$ and it may be calculated as:

$$\beta = \frac{\overline{Y}}{\overline{X}}$$

where $\overline{X}$ is the mean of observed streamflow data and $\overline{Y}$ is the mean of simulated streamflow data. This component indicates bias between observations and simulation of streamflow. Monthly mean and overall β values are shown in Table 13 and Figure 26, respectively.

The ideal value of the ratio between the CV of simulated values of streamflow and the CV of observations of streamflow, $\gamma = 1$ and it may be calculated as:

$$\gamma = \frac{S_Y/\overline{Y}}{S_X/\overline{X}}$$

where $\overline{X}$ is the mean of observed streamflow data, $\overline{Y}$ is the mean of simulated streamflow data, S_X is the standard deviation of observed streamflow data, and S_Y is the standard deviation of simulated streamflow data. This component indicates the variability of observations and simulation of streamflow. Monthly mean and overall KGE values are shown in Table 14 and Figure 27, respectively.

Table 10: Monthly average Nash Sutcliffe Efficiency, NSE

Index	USGS Streamgage	Nash Sutcliffe Efficiency, NSE											
		Jan.	Feb.	Mar.	Apr.	May	Jun.	Jul.	Aug.	Sep.	Oct.	Nov.	Dec.
5	50014800	-5.3	-1.9	-18.0	-0.5	-0.6	-0.5	-5.7	-0.3	-0.1	-1.3	-1.3	-5.9
9	50025155	-2.2	-0.7	-0.7	-0.4	-0.3	-2.4	-3.4	-0.1	-0.9	-0.4	-1.2	-8.1
10	50026025	-3.1	-0.5	-30.1	-0.5	-0.1	-29.9	-16.1	0.1	-0.1	-0.1	-0.4	-10.7
12	50027000	-0.7	0.0	-0.1	-0.3	-0.1	-51.2	-144.5	0.3	0.0	-0.1	-0.2	-4.4
13	50028000	-1.4	-0.8	-0.3	-0.2	-0.3	-0.8	-4.1	-0.1	-0.4	-0.6	-0.4	-6.8
14	50028400	-10.6	-14.0	-116.2	-0.9	-1.7	-5.2	-5.5	-1.8	-1.7	-1.8	-1.7	-31.0
16	50031200	-6.5	-0.1	-38.3	-21.2	-0.3	-11.8	-470.7	-1.4	0.2	-20.2	0.2	-4.0
19	50034000	-0.3	-1.6	-85.5	-0.5	0.1	-71.7	-436.3	0.0	-1.0	-0.1	-0.1	-1.4
20	50035000	-0.9	-0.3	-5.3	-2.0	0.0	-184.9	-627.0	-0.5	0.0	0.0	-3.1	-2.1
21	50038100	-13.9	-7.8	-207.2	-1.9	-9.5	-54.0	-52.3	-1.4	-2.1	-0.7	-0.7	-22.0
24	50039500	-0.6	-56.2	-7.2	-3.6	-0.2	-3.8	-316.6	-0.6	-1.0	-0.1	-0.4	-0.4
27	50043197	-3.4	-12.7	-339.8	-187.7	-21.4	-8805.0	-1468.4	-36.5	-0.4	-0.2	-47.0	-89.5
28	50043800	-0.2	-2.0	-78.9	-49.8	-0.6	-285.2	-226.9	0.1	-3.7	0.0	0.2	-29.4
29	50044810	-0.4	-6.4	-1.7	0.0	-0.1	-252.3	-880.1	-0.1	0.1	0.0	0.0	-1.1
31	50046000	-1.8	-54.8	-54.6	-19.4	-4.2	-61.1	-122.9	-3.6	-8.3	-0.5	0.3	-2.2
36	50049100	-0.3	-0.2	-0.9	0.0	-0.1	-0.7	-0.1	0.0	0.0	-0.1	0.0	-0.1
38	50050900	-1.0	-1.5	-13.1	-0.1	-0.7	-0.3	-0.1	-0.1	-0.1	-0.1	0.0	-3.6
39	50051310	-10.6	-26.1	-50.6	-1.1	-1.3	-4.7	-5.1	-0.1	-0.5	-11.1	-0.6	-19.0
40	50051800	-2.0	-1.4	-7.0	-0.2	-4.4	-3.5	-3.1	-0.2	-0.2	-0.9	-0.2	-4.7
41	50053025	-1.6	-2.0	-2.3	-0.4	-0.2	-0.7	-0.2	0.0	-0.1	-0.5	-0.1	-5.7
42	50055000	-1.7	-1.2	-1.4	-0.2	-0.4	-15.6	-4.7	0.0	0.0	-0.1	0.0	-2.5
43	50055225	-0.4	-0.7	-0.1	-0.1	0.0	-46.2	-0.7	0.0	0.0	-0.1	-0.1	-0.3
44	50055380	-0.4	-0.4	-0.2	-5.0	-0.2	-18.4	-38.2	0.0	0.0	-1.3	0.0	-0.3
45	50055750	-1.3	-0.8	-22.0	-25.9	-231.8	-312.8	-224.7	0.2	-1.2	-1.5	-0.3	0.0
46	50056400	-1.3	-23.4	-1.0	-0.9	-6.6	-3.3	-32.2	0.1	0.0	-1.2	0.0	-2.4
47	50057000	-0.5	-0.1	-22.1	-1.5	-2.8	-204.1	-171.7	0.2	0.0	0.1	-0.1	-0.3
48	50058350	-0.4	-1.4	-4.4	-0.1	-0.1	-4.1	-7.4	-0.1	-0.1	-0.1	-0.1	-0.8

Table 10 – Continued

Index	USGS Streamgage	Nash Sutcliffe Efficiency, NSE											
		Jan.	Feb.	Mar.	Apr.	May	Jun.	Jul.	Aug.	Sep.	Oct.	Nov.	Dec.
50	50059210	-2.2	-0.8	-2.1	-2.1	0.0	-272.0	-41.2	-1.1	0.0	-0.1	-0.1	-11.6
51	50061800	-1.4	-3.2	-0.9	-1.2	0.0	-13.2	-172.1	0.1	-1.7	-0.5	-0.1	0.0
52	50063800	-0.9	-1.2	-0.9	-0.6	-0.7	-0.5	-0.3	-0.2	-0.2	-0.4	-0.3	-0.7
53	50064200	-0.6	-1.1	-0.5	-0.2	-0.2	-0.2	-0.1	-0.2	-0.1	-0.2	-0.2	-0.5
54	50065500	-1.0	-1.0	-1.0	-0.4	-6.4	-0.7	-0.2	-0.2	-0.1	-0.2	-0.2	-0.3
55	50067000	-1.0	-0.7	-0.1	0.0	-0.2	-2.6	-18.9	0.0	0.0	-0.1	-0.2	-0.1
57	50071000	-0.5	-0.2	-0.9	-0.1	-0.1	0.0	-23.3	-0.1	0.0	0.0	-0.1	-0.1
58	50075000	-2.3	-0.9	-5.2	-0.7	-0.8	-5.4	-0.6	-0.3	-0.4	-0.6	-0.5	-1.0
60	50081000	-6.3	-8.7	-45.1	-1.2	-0.9	-13.5	-15.4	-0.1	-1.2	-19.0	0.0	-5.3
61	50083500	-3.8	-7.0	-51.8	-1.1	-1.6	-1.2	-1.0	-0.1	-0.6	-0.1	-0.2	-5.6
62	50085100	-5.9	-8.5	-58.3	-1.5	-260.0	-3.1	-1.2	-0.2	-0.8	-0.6	-0.2	-6.7
63	50090500	-3.2	-7.3	-22.8	-0.6	-0.3	-2.4	-0.7	-0.2	-0.6	-0.1	-0.2	-2.0
64	50092000	-2.0	-1.1	-58.8	-0.8	-0.2	-0.4	-0.6	0.0	-1.2	-0.3	-0.2	-8.2
65	50093000	-6.0	-4.5	-90.3	-1.9	-0.7	-2.1	-0.7	-0.3	-0.7	-656.8	-0.4	-1.5
72	50106100	-93.7	-180.0	-12790.5	-74.3	-495.6	-9111.1	-23552.6	-30.3	-0.2	0.0	-11.1	-88.8
74	50110650	-3.9	-2.3	-1.7	-0.1	-0.2	-54.1	-4.6	-0.1	-0.1	-0.1	-1.4	-8.2
75	50110900	-5.5	-429.1	-1689.8	-0.1	-1.1	-976.4	-187.5	-47.8	-2.2	0.0	-0.4	-232.0
79	50112500	-0.2	-0.3	-0.2	-0.1	-0.2	-7.2	-3.2	-0.3	-1.4	-1.2	-1.9	-3.6
80	50113800	-0.4	-0.3	-100.8	0.0	-0.1	0.0	-4.6	0.0	-0.2	-0.8	-0.9	-1.0
83	50114900	-3.8	-1.0	-42.5	-2.2	-0.7	-92.5	-89.4	-4.6	0.0	-0.5	-0.8	-9.4
84	50115240	0.0	-0.8	-33.3	-0.2	-0.1	-13.8	-24.1	-1.3	-0.4	-0.2	-0.4	-1.0
85	50124200	-0.4	-1.0	-186.5	-0.9	-0.2	-499.8	-407.8	-1.5	-1.4	-1.9	-1.7	-7.6
88	50136400	-24.0	-1.2	-2.9	-2.0	-25.1	-27.8	-136.0	-0.3	-0.2	-0.4	-2.3	-2.8
89	50138000	-1.2	-2.5	-13.1	-0.1	-1.8	-6.2	-379.7	0.1	-0.3	-2.2	-1.5	-2.3
90	50144000	-1.9	-0.3	-2.1	-0.4	-0.3	-3.4	-8.9	-0.1	-0.3	-0.8	-1.3	-5.8
92	50147800	-0.3	0.0	-0.1	-0.1	-0.1	-0.1	-0.1	-9.8	0.1	-0.1	0.0	-0.2
93	50148890	-0.1	-7.9	-59.9	-0.1	-0.2	-0.6	-12.7	-0.1	-0.2	-0.2	-0.1	-1.7

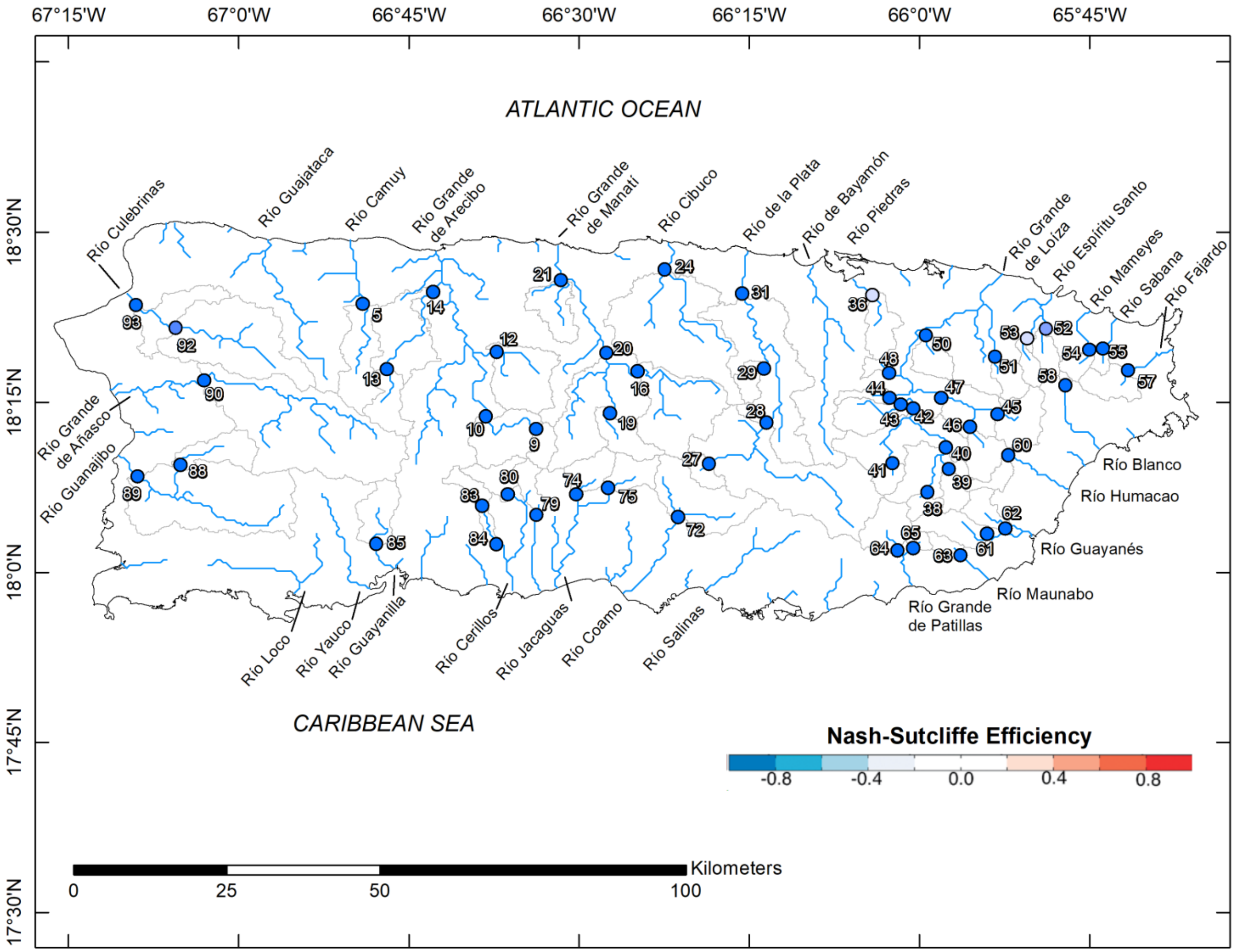

Figure 23: Overall NSE values at 54 basins across main island of Puerto Rico, numbered by Study Index.

Table 11: Monthly average Kling-Gupta Efficiency, KGE

Index	USGS Streamgage	Kling-Gupta Efficiency, KGE											
		Jan.	Feb.	Mar.	Apr.	May	Jun.	Jul.	Aug.	Sep.	Oct.	Nov.	Dec.
5	50014800	-0.2	-0.4	-0.4	-0.2	-0.1	0.0	-0.8	0.2	0.1	-0.2	-0.4	-0.3
9	50025155	-0.3	-0.3	-0.3	-0.2	-0.2	-0.2	-0.6	0.0	-0.1	-0.2	-0.1	-0.1
10	50026025	-0.3	-0.2	-0.1	0.0	-0.1	-1.0	-1.1	0.2	0.1	-0.1	0.1	-0.3
12	50027000	-0.2	-0.2	-0.1	0.0	-0.1	-1.2	-1.6	0.4	0.1	0.1	0.0	-0.4
13	50028000	-0.2	-0.3	-0.3	-0.3	-0.2	0.0	-0.2	0.0	0.0	-0.1	0.0	-0.2
14	50028400	-0.7	-0.6	-0.5	-0.5	-0.5	-0.4	-0.6	-0.3	-0.3	-0.4	-0.3	-0.4
16	50031200	-0.4	-0.3	-0.5	-0.5	-0.2	-0.7	-1.0	-0.1	0.2	-0.1	0.2	-0.1
19	50034000	-0.3	-0.3	-0.3	-0.1	0.0	-0.5	-3.4	0.2	0.0	0.1	0.2	0.1
20	50035000	-0.4	-0.2	-0.2	-0.2	-0.1	-1.2	-2.7	0.1	0.2	0.1	-0.8	0.1
21	50038100	-0.6	-0.5	-0.4	-0.4	-0.3	-1.8	-7.7	-0.4	-0.3	-0.3	-0.2	-0.5
24	50039500	-0.4	-1.2	-0.4	-0.2	0.1	-0.2	-2.0	0.0	0.2	0.3	0.2	0.2
27	50043197	-0.3	-1.2	-1.1	-1.0	-0.2	-6.2	-4.9	-0.6	0.0	0.0	-1.1	-0.8
28	50043800	-0.3	-0.4	-0.6	-0.7	-0.5	-1.8	-1.7	-0.1	-0.2	0.1	0.3	-0.4
29	50044810	-0.4	-0.3	-0.2	0.0	0.0	-3.1	-5.7	0.2	0.0	-0.1	0.2	0.1
31	50046000	-0.7	-1.2	-0.7	-0.9	-0.9	-2.0	-1.2	-0.6	-1.0	-0.1	0.3	-0.4
36	50049100	-0.4	-0.4	-0.3	-0.2	-0.4	-0.1	-0.1	-0.1	-0.1	-0.1	0.0	-0.2
38	50050900	-0.4	-0.4	-0.4	-0.4	-0.4	-0.1	-0.1	-0.2	-0.2	-0.1	-0.1	-0.7
39	50051310	-0.1	-0.3	-0.9	-0.3	-0.3	0.0	-0.2	0.1	0.1	0.0	-0.2	-1.4
40	50051800	-0.1	-0.3	-0.6	-0.2	-0.3	-0.3	0.0	0.0	0.1	0.0	0.0	-0.6
41	50053025	-0.3	-0.4	-0.3	-0.3	-0.2	-0.1	0.0	-0.1	-0.1	0.1	0.0	-0.2
42	50055000	-0.2	-0.3	-0.4	-0.2	-0.2	-0.4	-0.1	0.0	0.1	0.1	0.1	-0.2
43	50055225	-0.4	-0.5	-0.3	-0.3	-0.2	-0.8	0.0	-0.1	-0.1	-0.2	0.0	-0.1
44	50055380	-0.3	-0.5	-0.4	-0.7	-0.2	-1.5	-1.3	0.0	0.0	-0.4	0.0	0.0
45	50055750	-0.2	-0.4	-0.5	-0.6	-0.9	-1.3	-1.5	0.1	-0.1	0.0	-0.1	0.0
46	50056400	-0.2	-0.5	-0.1	-0.5	-0.7	-0.6	-1.6	0.0	0.0	0.1	0.0	-0.2
47	50057000	-0.2	-0.3	-0.3	-0.4	-0.9	-2.0	-3.9	0.1	0.1	0.1	0.0	0.0
48	50058350	-0.4	-0.5	-0.4	-0.4	-0.3	-0.2	-0.3	-0.3	-0.3	-0.2	-0.1	-0.3

Table 11 – Continued

Index	USGS Streamgage	Kling-Gupta Efficiency, KGE											
		Jan.	Feb.	Mar.	Apr.	May	Jun.	Jul.	Aug.	Sep.	Oct.	Nov.	Dec.
50	50059210	-0.3	-0.3	-0.3	-0.2	-0.1	-1.4	-1.0	-0.5	-0.1	-0.1	0.0	-1.2
51	50061800	-0.3	-0.3	-0.2	-0.1	0.1	-0.4	-1.2	0.1	-0.3	0.0	0.2	0.1
52	50063800	-0.5	-0.5	-0.4	-0.5	-0.4	-0.5	-0.1	-0.3	-0.1	-0.1	-0.1	-0.3
53	50064200	-0.5	-0.5	-0.4	-0.4	-0.3	-0.2	-0.1	-0.2	0.0	-0.1	0.0	-0.3
54	50065500	-0.5	-0.6	-0.5	-0.6	-0.3	-0.2	-0.2	-0.3	-0.2	-0.2	-0.1	-0.3
55	50067000	-0.5	-0.5	-0.4	-0.4	-0.3	-0.3	-0.7	-0.2	-0.2	-0.2	0.0	-0.2
57	50071000	-0.5	-0.5	-0.4	-0.3	-0.3	-0.1	-0.9	-0.2	-0.2	0.0	0.0	-0.2
58	50075000	-0.5	-0.6	-0.5	-0.5	-0.3	-0.4	-0.3	-0.2	-0.2	-0.2	-0.1	-0.2
60	50081000	-0.3	-0.3	-1.1	-0.3	-0.2	0.0	-0.5	0.1	-0.3	-0.2	0.0	-0.5
61	50083500	-0.2	-0.5	-1.5	-0.3	-0.4	0.0	0.0	-0.1	-0.1	0.1	0.0	-1.1
62	50085100	-0.3	-0.4	-1.6	-0.3	-2.2	-0.2	0.0	-0.1	-0.2	0.0	0.0	-1.0
63	50090500	-0.3	-0.3	-0.5	-0.2	-0.2	-0.1	0.0	-0.2	0.0	0.0	-0.1	-0.3
64	50092000	-0.2	-0.3	-2.5	-0.5	-0.2	-0.2	-0.1	-0.2	-0.4	0.1	0.0	-1.2
65	50093000	-0.3	-0.3	-0.4	-0.3	-0.3	-0.2	-0.1	-0.2	0.0	-1.6	-0.1	-0.3
72	50106100	-1.4	-2.5	-4.5	-3.2	-4.6	-9.7	-12.9	-3.2	-0.7	0.0	-0.4	-1.3
74	50110650	-0.2	-0.3	-0.3	-0.3	-0.3	-1.7	-0.8	-0.1	-0.1	-0.2	-0.4	-0.3
75	50110900	-0.2	-0.7	-1.2	-0.4	-0.5	-3.5	-2.9	-1.4	-0.8	-0.1	0.0	-1.3
79	50112500	-0.2	-0.2	-0.4	-0.1	-0.2	-0.6	-0.1	0.1	-0.2	-0.4	-0.1	-0.1
80	50113800	-0.2	-0.2	-0.3	-0.1	-0.1	-0.1	-0.6	0.1	-0.2	-0.3	-0.1	-0.3
83	50114900	0.0	0.2	-0.6	0.0	-0.2	-1.1	-3.5	-0.3	0.0	-0.3	-0.3	-1.0
84	50115240	-0.3	-0.4	-0.4	-0.2	-0.2	-1.6	-1.0	-0.1	-0.2	-0.2	-0.1	-0.2
85	50124200	-0.2	-0.4	-0.8	-0.2	-0.3	-3.5	-3.2	-0.3	-0.1	0.0	-0.1	-0.2
88	50136400	-0.5	-0.2	-0.4	-0.1	-0.3	-2.7	-4.6	0.0	-0.1	-0.1	-0.4	-0.3
89	50138000	-0.2	-0.1	-0.4	-0.2	-0.2	-0.2	-1.6	0.4	0.1	-0.9	-0.2	-0.7
90	50144000	-0.4	0.1	-0.3	-0.2	-0.2	-0.5	-1.1	0.0	-0.2	-0.1	-0.2	-0.6
92	50147800	-0.2	-0.2	-0.3	-0.3	-0.5	-0.3	-0.2	-0.6	-0.1	-0.3	-0.1	-0.2
93	50148890	-0.1	-0.3	-1.8	-0.2	-0.3	-0.3	-0.5	0.2	0.0	-0.1	0.0	-0.5

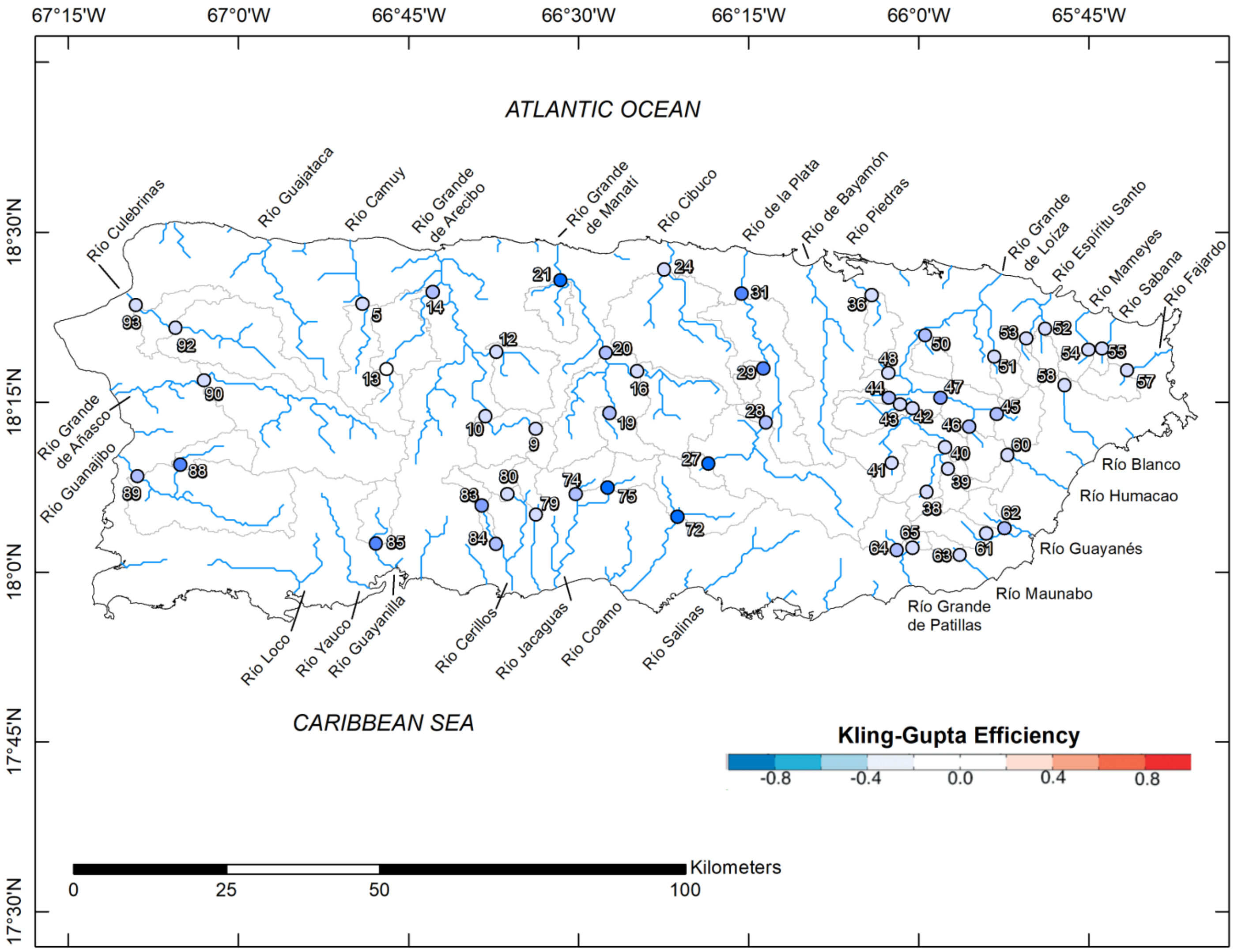

Figure 24: Overall KGE values at 54 basins across main island of Puerto Rico, numbered by Study Index.

Table 12: Monthly average Pearson product-moment correlation coefficient, r

Index	USGS Streamgage	Pearson Product-Moment Correlation Coefficient, r											
		Jan.	Feb.	Mar.	Apr.	May	Jun.	Jul.	Aug.	Sep.	Oct.	Nov.	Dec.
5	50014800	0.1	0.1	0.1	0.3	0.4	0.4	0.4	0.6	0.7	0.3	0.4	0.2
9	50025155	0.0	0.2	0.3	0.2	0.3	0.4	0.4	0.5	0.3	0.3	0.4	0.3
10	50026025	0.0	0.3	0.3	0.4	0.3	0.3	0.3	0.5	0.4	0.2	0.4	0.3
12	50027000	0.1	0.2	0.4	0.3	0.3	0.3	0.4	0.6	0.4	0.3	0.4	0.3
13	50028000	0.3	0.2	0.3	0.3	0.3	0.3	0.2	0.3	0.4	0.3	0.4	0.2
14	50028400	-0.1	0.0	0.1	0.1	0.1	0.2	0.2	0.3	0.3	0.2	0.3	0.1
16	50031200	0.1	0.1	0.2	0.4	0.3	0.3	0.2	0.5	0.6	0.4	0.5	0.4
19	50034000	0.0	0.0	0.1	0.4	0.5	0.2	0.5	0.5	0.4	0.4	0.6	0.4
20	50035000	0.0	0.2	0.4	0.4	0.3	0.4	0.4	0.6	0.5	0.4	0.4	0.4
21	50038100	0.0	0.1	0.2	0.2	0.2	0.2	0.2	0.3	0.4	0.3	0.4	0.4
24	50039500	0.0	0.3	0.1	0.4	0.5	0.5	0.3	0.4	0.6	0.5	0.6	0.6
27	50043197	0.1	0.0	0.1	0.2	0.3	0.3	0.6	0.6	0.5	0.3	0.4	0.2
28	50043800	0.0	0.1	0.2	0.2	0.2	0.3	0.6	0.5	0.4	0.4	0.6	0.4
29	50044810	0.0	0.1	0.2	0.4	0.2	0.5	0.3	0.4	0.4	0.3	0.5	0.2
31	50046000	-0.1	0.0	0.1	0.4	0.3	0.3	0.2	0.4	0.3	0.4	0.7	0.3
36	50049100	0.2	0.1	0.2	0.4	0.1	0.3	0.2	0.3	0.2	0.2	0.4	0.4
38	50050900	0.1	0.2	0.1	0.2	0.1	0.3	0.5	0.4	0.4	0.4	0.4	0.3
39	50051310	0.3	0.1	0.2	0.3	0.2	0.4	0.5	0.7	0.5	0.5	0.5	0.3
40	50051800	0.3	0.0	0.2	0.2	0.2	0.4	0.6	0.5	0.5	0.4	0.5	0.4
41	50053025	0.2	0.1	0.2	0.1	0.3	0.4	0.5	0.5	0.4	0.4	0.4	0.3
42	50055000	0.2	0.0	0.1	0.2	0.3	0.5	0.5	0.6	0.5	0.4	0.5	0.4
43	50055225	0.1	0.0	0.1	0.1	0.2	0.3	0.5	0.4	0.4	0.1	0.4	0.3
44	50055380	0.1	-0.2	0.0	0.1	0.1	0.2	0.4	0.3	0.3	0.2	0.4	0.3
45	50055750	0.2	0.0	0.2	0.3	0.4	0.3	0.4	0.4	0.4	0.4	0.3	0.4
46	50056400	0.2	0.1	0.2	0.1	0.3	0.2	0.4	0.5	0.3	0.5	0.5	0.3
47	50057000	0.1	0.0	0.2	0.3	0.3	0.3	0.4	0.5	0.5	0.5	0.6	0.4
48	50058350	0.2	0.0	0.0	0.2	0.3	0.4	0.5	0.3	0.3	0.3	0.4	0.4

Table 12 – Continued

Index	USGS Streamgage	Pearson Product-Moment Correlation Coefficient, r											
		Jan.	Feb.	Mar.	Apr.	May	Jun.	Jul.	Aug.	Sep.	Oct.	Nov.	Dec.
50	50059210	0.2	0.1	0.2	0.2	0.3	0.4	0.3	0.4	0.4	0.2	0.4	0.3
51	50061800	0.1	0.1	0.3	0.3	0.4	0.1	0.3	0.5	0.5	0.5	0.4	0.5
52	50063800	0.1	0.0	0.2	0.1	0.3	0.4	0.4	0.4	0.5	0.4	0.4	0.3
53	50064200	0.1	0.0	0.2	0.1	0.3	0.3	0.5	0.4	0.5	0.4	0.5	0.3
54	50065500	0.0	-0.1	0.2	0.1	0.2	0.4	0.3	0.3	0.3	0.3	0.4	0.3
55	50067000	0.0	0.0	0.2	0.2	0.3	0.3	0.3	0.3	0.3	0.3	0.5	0.3
57	50071000	0.0	0.0	0.2	0.3	0.3	0.3	0.3	0.3	0.3	0.3	0.5	0.3
58	50075000	0.1	0.0	0.1	0.3	0.4	0.2	0.3	0.4	0.4	0.3	0.4	0.5
60	50081000	0.1	0.1	0.1	0.3	0.3	0.3	0.4	0.6	0.4	0.3	0.5	0.2
61	50083500	0.2	0.1	0.2	0.2	0.2	0.4	0.5	0.5	0.4	0.6	0.5	0.4
62	50085100	0.2	0.1	0.2	0.3	0.1	0.4	0.5	0.6	0.5	0.6	0.6	0.5
63	50090500	0.3	0.2	0.1	0.2	0.2	0.3	0.5	0.4	0.5	0.5	0.4	0.3
64	50092000	0.3	0.1	0.1	0.2	0.3	0.1	0.5	0.5	0.5	0.5	0.4	0.5
65	50093000	0.3	0.1	0.1	0.2	0.2	0.3	0.4	0.4	0.4	0.3	0.3	0.3
72	50106100	0.3	0.2	0.0	0.2	0.3	0.4	0.5	0.4	0.3	0.4	0.6	0.2
74	50110650	0.2	0.1	0.1	0.2	0.2	0.3	0.2	0.2	0.3	0.2	0.5	0.2
75	50110900	0.4	0.1	0.0	0.3	0.3	0.3	0.2	0.2	0.3	0.3	0.5	0.1
79	50112500	0.2	0.2	0.1	0.4	0.3	0.3	0.4	0.5	0.3	0.3	0.4	0.3
80	50113800	0.1	0.4	0.1	0.4	0.5	0.4	0.1	0.5	0.3	0.3	0.4	0.1
83	50114900	0.3	0.5	0.1	0.4	0.4	0.3	0.3	0.4	0.4	0.3	0.5	0.1
84	50115240	0.0	0.0	0.0	0.1	0.1	0.2	0.0	0.4	0.2	0.1	0.3	0.0
85	50124200	0.3	0.0	0.2	0.4	0.3	0.4	0.3	0.4	0.2	0.3	0.4	0.2
88	50136400	0.2	0.2	-0.1	0.4	0.1	0.2	0.5	0.3	0.4	0.4	0.3	0.1
89	50138000	0.1	0.2	-0.1	0.3	0.2	0.5	0.5	0.6	0.5	0.6	0.4	0.2
90	50144000	0.1	0.4	0.1	0.2	0.2	0.1	0.2	0.4	0.3	0.3	0.3	0.2
92	50147800	0.1	0.4	0.1	0.3	0.0	0.3	0.2	0.3	0.3	0.3	0.3	0.2
93	50148890	0.2	0.1	0.3	0.3	0.2	0.3	0.2	0.6	0.5	0.4	0.4	0.2

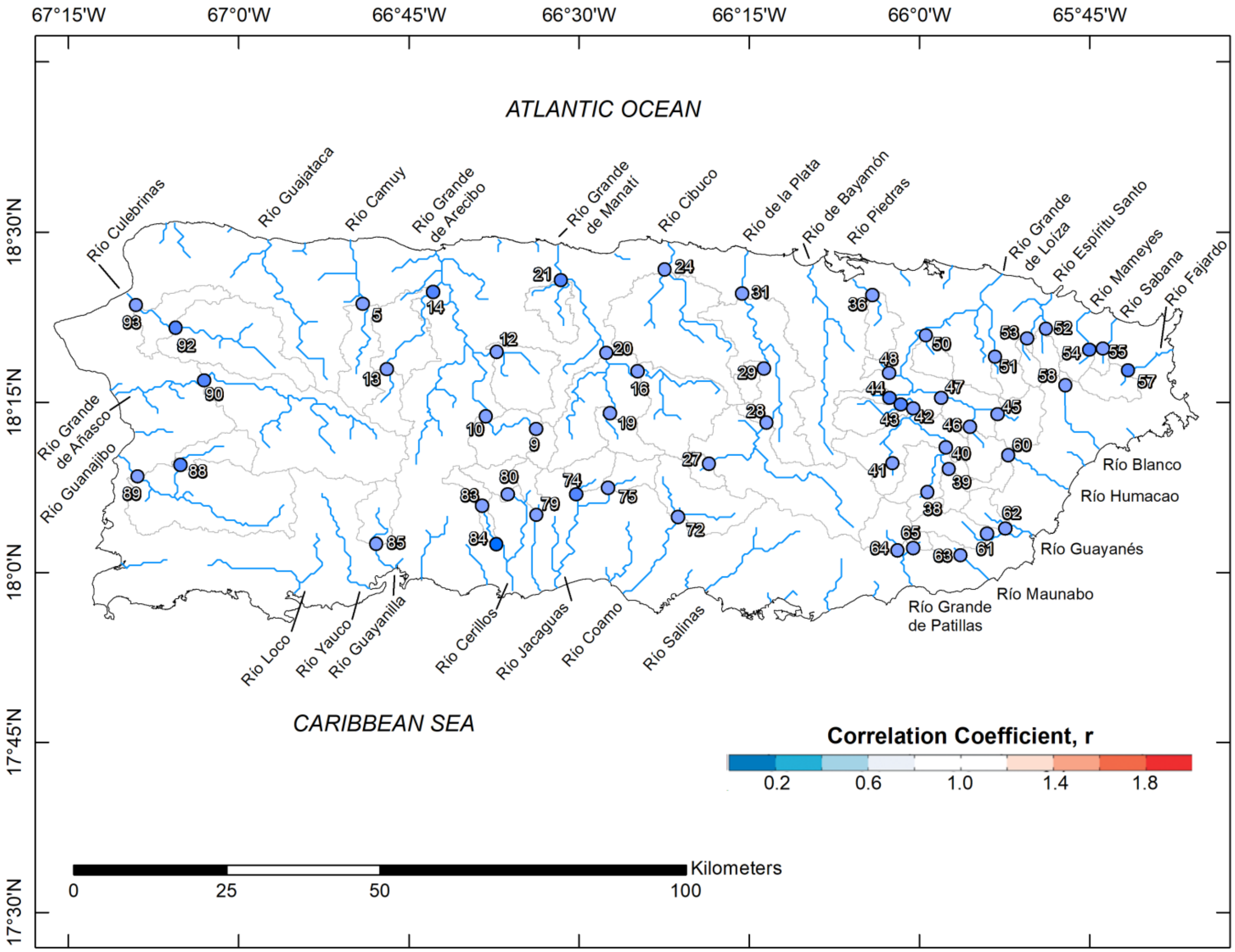

Figure 25: Overall r values at 54 basins across main island of Puerto Rico, numbered by Study Index.

Table 13: Monthly average ratio of mean simulated and mean observed flows, β

Index	USGS Streamgage	Ratio of Mean Simulated and Mean Observed Flows, β											
		Jan.	Feb.	Mar.	Apr.	May	Jun.	Jul.	Aug.	Sep.	Oct.	Nov.	Dec.
5	50014800	0.4	0.4	0.5	0.3	0.2	0.4	0.5	0.4	0.3	0.3	0.4	0.3
9	50025155	0.4	0.4	0.5	0.5	0.3	0.7	0.8	0.3	0.2	0.3	0.3	0.6
10	50026025	0.6	0.5	0.8	0.7	0.5	1.0	1.1	0.6	0.4	0.4	0.3	0.6
12	50027000	0.7	0.6	0.6	0.7	0.6	1.1	1.5	0.9	0.5	0.5	0.4	0.6
13	50028000	0.4	0.4	0.5	0.3	0.3	0.5	0.6	0.4	0.3	0.3	0.3	0.3
14	50028400	0.0	0.0	0.0	0.0	0.0	0.0	0.0	0.0	0.0	0.0	0.0	0.0
16	50031200	1.1	1.1	1.3	1.5	1.1	2.3	2.6	1.6	0.6	0.6	0.5	1.1
19	50034000	0.6	0.7	0.9	0.8	0.6	1.3	1.9	1.0	0.8	0.4	0.5	0.9
20	50035000	0.8	0.8	0.9	1.0	0.9	2.3	2.3	1.4	1.0	0.6	0.6	0.9
21	50038100	0.1	0.1	0.1	0.1	0.1	0.2	0.2	0.1	0.1	0.1	0.0	0.1
24	50039500	0.7	0.9	1.1	1.1	1.2	1.8	2.5	1.4	0.8	0.7	0.6	0.6
27	50043197	0.7	2.4	2.0	2.1	1.4	7.1	5.0	1.6	0.8	0.5	2.0	2.2
28	50043800	0.8	1.3	1.8	1.8	1.4	3.4	3.3	1.0	1.2	0.7	0.6	1.3
29	50044810	0.5	0.5	0.5	0.6	0.6	1.1	1.2	0.9	0.6	0.5	0.4	0.6
31	50046000	1.4	2.4	1.9	2.2	2.2	3.6	2.3	2.0	2.3	1.3	0.6	1.7
36	50049100	0.3	0.4	0.5	0.4	0.2	0.7	0.6	0.4	0.4	0.5	0.3	0.3
38	50050900	0.3	0.3	0.3	0.2	0.3	0.5	0.4	0.2	0.2	0.2	0.2	0.3
39	50051310	0.3	0.3	0.3	0.3	0.3	0.5	0.5	0.3	0.3	0.3	0.2	0.3
40	50051800	0.4	0.4	0.5	0.5	0.6	1.0	0.7	0.4	0.4	0.4	0.3	0.4
41	50053025	0.3	0.4	0.4	0.3	0.3	0.6	0.6	0.3	0.3	0.4	0.2	0.4
42	50055000	0.3	0.4	0.5	0.5	0.5	1.3	0.8	0.4	0.4	0.4	0.3	0.5
43	50055225	0.5	0.5	0.8	0.6	0.5	1.7	1.2	0.6	0.4	0.7	0.4	0.7
44	50055380	0.7	0.9	0.8	0.9	0.6	0.9	1.2	0.7	0.6	1.2	0.4	0.7
45	50055750	0.7	0.9	1.4	1.2	1.6	2.4	2.3	0.9	0.9	0.5	0.3	0.6
46	50056400	0.3	0.5	0.7	0.8	1.2	1.4	2.6	0.4	0.7	0.3	0.2	0.4
47	50057000	0.7	0.8	1.2	0.9	1.3	3.2	4.8	0.6	0.6	0.4	0.2	0.5
48	50058350	0.4	0.3	0.4	0.2	0.3	0.7	0.7	0.3	0.2	0.3	0.2	0.3

Table 13 – Continued

Index	USGS Streamgage	Ratio of Mean Simulated and Mean Observed Flows, β											
		Jan.	Feb.	Mar.	Apr.	May	Jun.	Jul.	Aug.	Sep.	Oct.	Nov.	Dec.
50	50059210	0.8	1.1	1.1	0.9	1.0	2.7	2.2	1.6	0.6	0.5	0.6	0.8
51	50061800	0.5	0.5	0.5	0.6	0.7	1.0	1.6	1.0	1.0	1.3	0.7	0.6
52	50063800	0.2	0.2	0.2	0.2	0.2	0.3	0.4	0.2	0.2	0.2	0.1	0.1
53	50064200	0.2	0.2	0.4	0.3	0.3	0.7	0.6	0.2	0.3	0.3	0.2	0.2
54	50065500	0.1	0.1	0.1	0.1	0.2	0.2	0.2	0.1	0.1	0.2	0.1	0.1
55	50067000	0.6	0.6	0.5	0.4	0.4	0.9	1.0	0.4	0.3	0.3	0.2	0.4
57	50071000	0.3	0.4	0.5	0.5	0.3	0.7	1.3	0.4	0.3	0.4	0.3	0.3
58	50075000	0.1	0.1	0.1	0.1	0.1	0.1	0.2	0.1	0.1	0.1	0.1	0.1
60	50081000	0.2	0.2	0.3	0.2	0.3	0.4	0.7	0.4	0.4	0.4	0.3	0.2
61	50083500	0.2	0.2	0.3	0.2	0.3	0.5	0.4	0.2	0.4	0.3	0.2	0.2
62	50085100	0.1	0.1	0.1	0.1	0.2	0.3	0.3	0.2	0.3	0.1	0.1	0.1
63	50090500	0.2	0.2	0.3	0.3	0.3	0.4	0.3	0.2	0.4	0.3	0.2	0.3
64	50092000	0.3	0.4	0.4	0.2	0.4	0.5	0.5	0.2	0.4	0.3	0.2	0.5
65	50093000	0.2	0.3	0.4	0.3	0.3	0.4	0.5	0.2	0.4	0.3	0.2	0.2
72	50106100	2.9	4.3	6.1	4.8	6.2	11.4	13.5	5.0	1.9	0.9	1.7	2.7
74	50110650	0.4	0.4	0.5	0.4	0.3	0.8	0.7	0.4	0.4	0.3	0.3	0.5
75	50110900	1.6	2.3	2.6	1.1	1.3	4.6	4.2	2.3	1.6	1.0	0.8	1.9
79	50112500	0.7	0.9	1.1	0.7	0.5	0.7	1.0	0.5	0.3	0.3	0.3	0.5
80	50113800	0.5	0.6	0.9	0.6	0.3	0.5	1.0	0.4	0.2	0.2	0.2	0.4
83	50114900	0.5	0.7	1.0	0.9	0.6	1.3	1.3	0.7	0.5	0.3	0.3	0.5
84	50115240	0.8	1.1	1.3	0.7	0.7	1.5	1.9	1.0	0.5	0.4	0.4	0.7
85	50124200	1.2	1.5	2.1	1.3	1.2	2.5	3.6	1.5	0.7	0.7	0.7	1.1
88	50136400	0.6	0.7	0.6	0.4	0.6	0.6	0.9	0.5	0.2	0.3	0.5	0.4
89	50138000	1.0	1.2	1.4	0.7	0.8	1.7	2.8	0.9	0.5	0.3	0.5	0.7
90	50144000	0.5	0.7	1.0	0.5	0.4	0.6	0.7	0.4	0.3	0.3	0.3	0.4
92	50147800	0.5	0.6	0.8	0.3	0.2	0.1	0.3	0.3	0.3	0.2	0.3	0.6
93	50148890	0.9	1.0	2.9	0.6	0.3	0.3	0.8	0.3	0.3	0.3	0.4	0.6

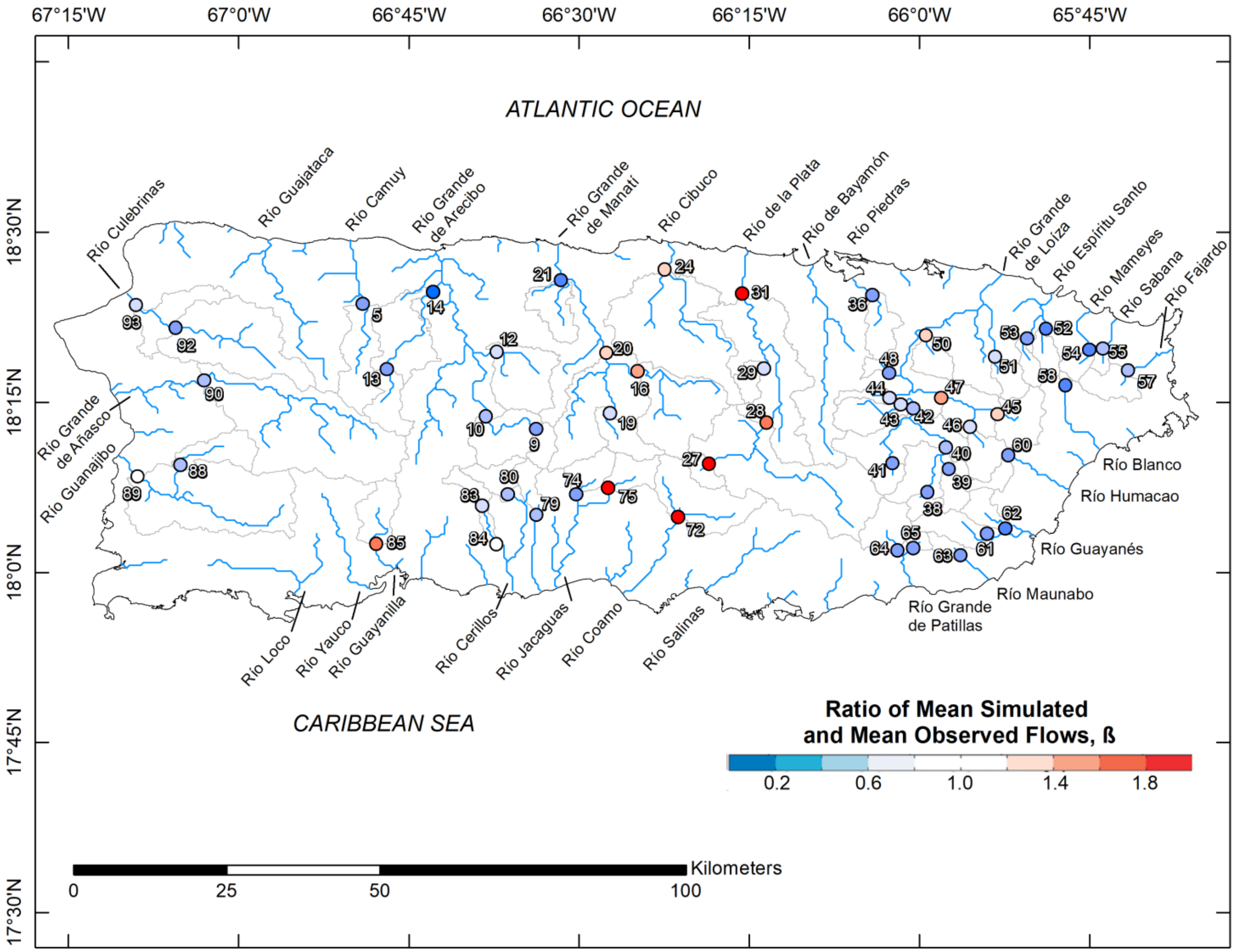

Figure 26: Overall β values at 54 basins across main island of Puerto Rico, numbered by Study Index.

Table 14: Monthly average Variability Ratio, γ

Index	USGS Streamgage	Variability Ratio, γ Jan.	Feb.	Mar.	Apr.	May	Jun.	Jul.	Aug.	Sep.	Oct.	Nov.	Dec.
5	50014800	1.0	0.6	0.8	0.4	0.6	1.1	2.1	1.3	0.9	1.5	1.8	1.3
9	50025155	0.4	0.3	0.2	0.4	0.5	1.2	1.8	0.7	0.8	1.1	1.3	1.0
10	50026025	0.5	0.3	0.4	0.5	0.3	1.7	2.1	0.6	0.7	0.8	1.0	1.7
12	50027000	0.4	0.2	0.2	0.5	0.3	2.4	3.1	0.7	0.6	0.8	0.9	1.6
13	50028000	0.3	0.2	0.1	0.2	0.3	0.9	1.1	0.7	0.9	1.0	1.0	1.0
14	50028400	0.7	0.6	0.3	0.3	0.4	1.1	1.3	0.8	0.7	0.6	0.9	0.8
16	50031200	0.2	0.2	0.1	0.4	0.3	0.7	0.4	0.6	0.5	0.9	0.7	1.2
19	50034000	0.2	0.2	0.3	0.4	0.4	2.0	5.1	0.6	1.0	0.8	1.2	0.7
20	50035000	0.2	0.2	0.2	0.4	0.3	2.2	3.8	0.5	0.7	0.7	2.0	0.9
21	50038100	0.4	0.4	0.4	0.4	0.5	3.2	9.5	1.3	1.1	1.0	1.0	1.6
24	50039500	0.2	1.7	0.2	0.3	0.6	0.7	2.4	0.8	1.2	1.1	1.5	0.6
27	50043197	0.2	0.2	0.7	0.5	0.6	3.1	3.0	0.7	0.6	0.6	0.6	0.3
28	50043800	0.2	0.1	0.3	0.5	0.3	1.1	1.2	0.3	0.6	0.7	0.6	1.2
29	50044810	0.1	0.2	0.3	0.5	0.5	4.0	6.6	0.6	0.5	0.5	1.1	1.0
31	50046000	0.2	0.2	0.5	0.6	0.4	1.1	1.6	0.5	0.6	0.7	0.7	0.5
36	50049100	0.1	0.1	0.3	0.1	0.2	0.5	0.5	0.5	0.7	0.4	0.6	0.3
38	50050900	0.2	0.2	0.6	0.1	0.3	0.7	0.4	0.4	0.5	0.6	0.6	0.9
39	50051310	0.5	0.5	1.6	0.3	0.6	1.0	1.2	0.6	1.0	1.3	1.4	2.3
40	50051800	0.5	0.3	1.1	0.3	0.4	1.2	1.0	0.6	0.9	1.0	1.2	1.5
41	50053025	0.2	0.2	0.6	0.3	0.4	0.8	0.6	0.4	0.6	1.0	0.8	0.8
42	50055000	0.4	0.4	0.6	0.4	0.4	1.1	0.9	0.4	0.8	0.8	0.8	1.0
43	50055225	0.1	0.1	0.2	0.3	0.2	0.9	0.7	0.3	0.4	0.4	0.6	0.5
44	50055380	0.1	0.2	0.1	1.6	0.3	2.5	2.5	0.4	0.4	0.4	0.6	0.4
45	50055750	0.3	0.1	0.1	0.2	0.4	1.1	1.1	0.5	0.8	1.1	0.6	0.4
46	50056400	0.5	0.8	0.4	0.2	0.3	0.7	0.8	0.4	0.6	0.8	0.7	0.8
47	50057000	0.2	0.2	0.1	0.2	0.3	0.9	0.7	0.6	0.6	0.6	1.0	0.6
48	50058350	0.1	0.1	0.2	0.1	0.3	0.9	1.1	0.3	0.4	0.4	0.6	0.6

Table 14 – Continued

Index	USGS Streamgage	Variability Ratio, γ											
		Jan.	Feb.	Mar.	Apr.	May	Jun.	Jul.	Aug.	Sep.	Oct.	Nov.	Dec.
50	50059210	0.1	0.4	0.2	0.2	0.3	1.7	0.9	0.5	0.4	0.4	0.6	1.8
51	50061800	0.2	0.3	0.3	0.4	0.5	1.3	1.9	0.9	1.3	0.8	0.8	0.4
52	50063800	0.2	0.2	0.3	0.2	0.3	1.0	0.5	0.3	0.6	0.7	0.7	0.4
53	50064200	0.1	0.2	0.2	0.1	0.2	0.6	0.4	0.4	0.5	0.6	0.7	0.4
54	50065500	0.3	0.2	0.2	0.1	0.3	0.9	0.6	0.4	0.5	0.5	0.7	0.5
55	50067000	0.2	0.1	0.1	0.1	0.2	0.6	0.5	0.3	0.3	0.4	0.7	0.4
57	50071000	0.1	0.1	0.1	0.2	0.3	0.5	0.6	0.3	0.4	0.6	0.8	0.4
58	50075000	0.3	0.1	0.3	0.1	0.3	0.6	0.5	0.4	0.5	0.9	0.8	0.6
60	50081000	0.5	0.5	1.7	0.3	0.8	1.1	2.0	0.9	1.7	1.2	1.1	0.9
61	50083500	0.6	0.8	2.0	0.4	1.0	1.1	0.8	0.4	1.3	1.0	1.3	2.0
62	50085100	0.7	0.8	2.2	0.3	3.1	1.1	1.0	0.5	1.5	1.1	1.2	2.1
63	50090500	0.5	0.4	0.8	0.4	0.6	1.2	0.6	0.5	1.0	0.9	1.2	1.1
64	50092000	0.4	0.3	2.7	0.1	0.5	0.8	0.7	0.3	1.3	0.9	0.8	2.2
65	50093000	0.4	0.3	0.8	0.4	0.4	1.0	0.7	0.5	1.2	2.6	1.1	0.6
72	50106100	0.5	0.3	0.8	0.3	0.6	2.3	4.9	0.5	0.3	0.9	1.4	0.7
74	50110650	0.6	0.3	0.4	0.2	0.3	2.7	1.8	0.5	0.6	0.6	1.7	1.1
75	50110900	0.3	0.7	0.6	0.1	0.3	2.0	1.4	0.5	0.4	0.5	0.7	1.3
79	50112500	0.2	0.2	0.1	0.3	0.3	1.1	1.0	0.7	0.9	1.5	1.4	0.7
80	50113800	0.3	0.1	0.4	0.3	0.4	0.3	1.1	0.7	0.6	1.3	1.3	1.1
83	50114900	0.7	0.5	1.2	0.8	0.9	2.2	4.8	1.0	0.6	1.2	1.5	2.2
84	50115240	0.1	0.1	0.3	0.4	0.3	1.7	1.4	0.7	0.7	0.8	1.0	0.7
85	50124200	0.2	0.3	0.3	0.3	0.2	3.7	2.6	0.5	0.8	1.0	1.2	0.6
88	50136400	1.1	0.3	0.4	0.4	0.7	3.4	5.7	0.9	0.7	0.6	1.9	0.9
89	50138000	0.4	0.4	0.6	0.2	0.6	0.8	1.7	0.9	0.9	2.1	1.8	2.1
90	50144000	1.2	0.5	0.6	0.3	0.3	1.2	1.9	0.6	0.5	0.7	1.3	1.9
92	50147800	0.3	0.1	0.1	0.2	0.3	0.3	0.5	1.4	0.5	0.3	0.5	0.3
93	50148890	0.3	0.5	0.1	0.2	0.3	1.0	1.3	0.8	0.9	0.8	0.8	1.0

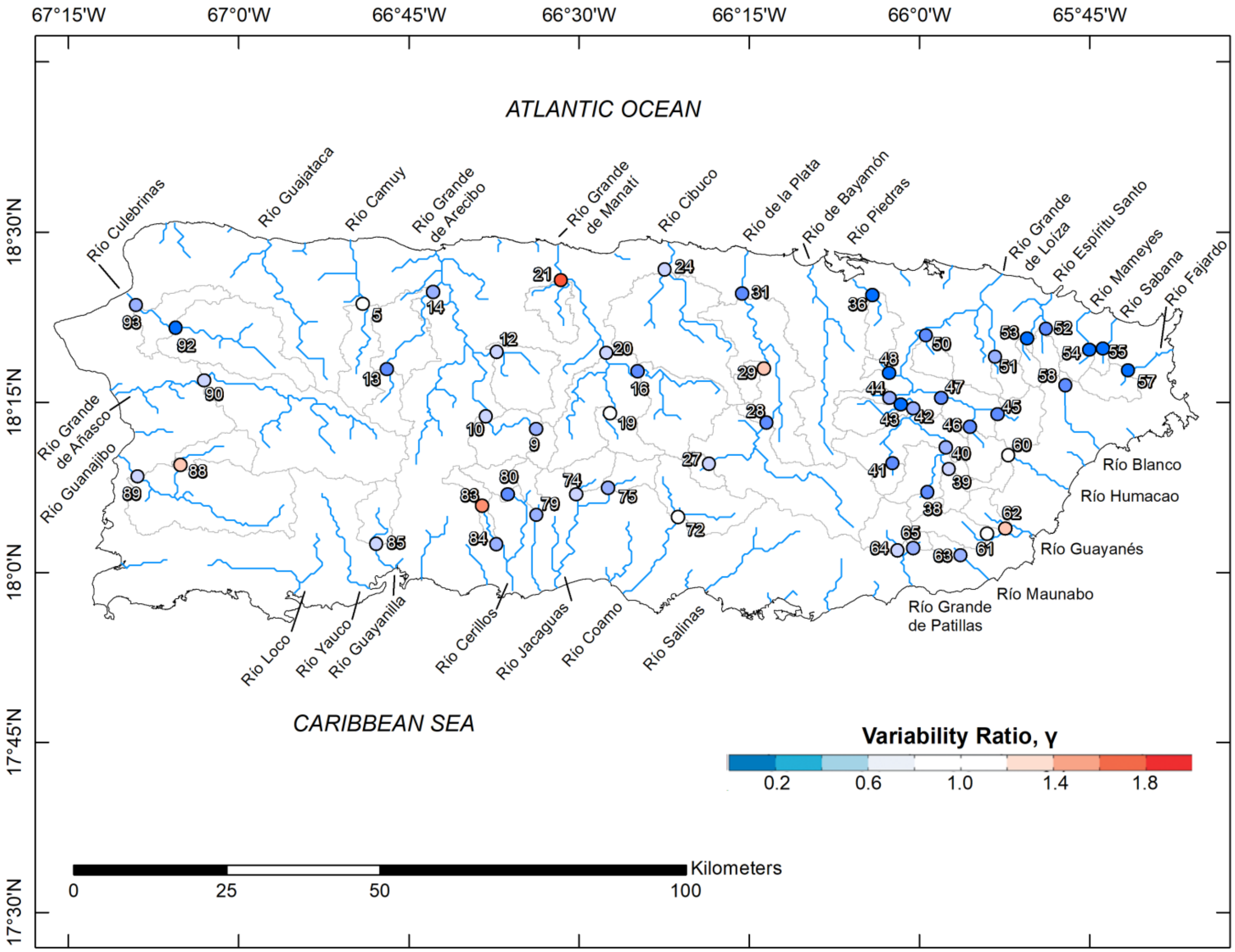

Figure 27: Overall γ values at 54 basins across main island of Puerto Rico, numbered by Study Index

6.3 Sources of Error

Model performance according to NSE and KGE measures shows poor accuracy. Certainly, multiple sources of error exist for this modelling approach, including persistent underestimation of rainfall and low spatiotemporal resolution of rainfall estimates. Although it is difficult to quantify their individual effects, it is clear that these limitations negatively influence the model's ability to accurately predict streamflow.

6.3.1 Underestimation of Rainfall Accumulation

As shown in Table 13 and Figure 26, the ratio of mean simulated and mean observed flows, β, has monthly average values between zero and one for every modelled watershed, depending on the season. This indicates that simulations are biased toward low estimation of streamflow. Underestimation of streamflow likely indicates underestimation of rainfall. Persistent underestimation of rainfall can cause antecedent conditions that are two dry, delaying the generation of runoff and decreasing peaks. Also, total rainfall water volumes estimated by IMERG Late Run may be less than the ground truth on an event-scale, causing less water to enter modelled watersheds as rainfall flux.

Antecedent conditions play a large role in the performance of hydrologic models at the plot, catchment, and watershed scales (Zehe & Blöschl, 2004). Regarding the challenges of hydrologic prediction, the National Research Council's (NRC's) Committee on Hydrologic Science (COHS) noted "in watershed rainfall-runoff transformation [...] initial and boundary conditions are the critical issues" (The National Research Council, 2003). Soil moisture and streamflow effectively represent the memory of a watershed between storm events. As such, persistent inaccurate estimation of rainfall within a hydrologic model will set too wet or too dry soil moisture conditions, or too high or too low streamflow rates before an upcoming storm event. Whether this storm event is predicted to cause a flood or not can be completely changed given different initial conditions within the model. Therefore, inaccurate estimation of current rainfall can decrease the accuracy of prediction for a subsequent events. And, there is certainly evidence of inaccurate estimation of rainfall on Puerto Rico by IMERG Late Run at both short and long temporal scales.

As shown in Table 6, IMERG Late Run estimates of rainfall underestimate total rainfall accumulations for the small watersheds in Puerto Rico on an annual scale. Similarly, Figure 28 shows that over a 27 month period, total rainfall accumulations as estimated by IMERG Late Run underestimates the quantity measured by USGS 182647066201700 Sabana Hoyos 2 with a 4.89% difference. This underestimation is small, as USGS observed a total of 4212 mm of rainfall, while IMERG Late Run estimated a total of 4011 mm. However, the total accumulations during short time periods can vary greatly.

During January of 2018, USGS observed a total of 148 mm of rainfall at Sabana Hoyos 2 Well at Vega Alta, while IMERG Late Run estimated only 5 mm total, a 186.93% difference. This illustrates the capacity of IMERG to greatly underestimate rainfall, as highlighted in yellow in Figure 28. During June of 2018, USGS observed 44 mm of rainfall at Sabana Hoyos 2 Well at Vega Alta, while IMERG Late Run estimated 487 mm total, a 166.86% difference. This illustrates the capacity of IMERG to also greatly overestimate rainfall, as highlighted in orange in Figure 28. As a result, the initial soil conditions for model analysis of nearby watersheds starting in February and July of 2018 would likely be too dry and too wet, respectively, and streamflow would likely be misrepresented. Although watersheds in Puerto Rico consistently demonstrate very quick hydrologic responses, they will nonetheless be influenced by the long-term behavior of soil moisture and streamflow (Smith et al., 2005).

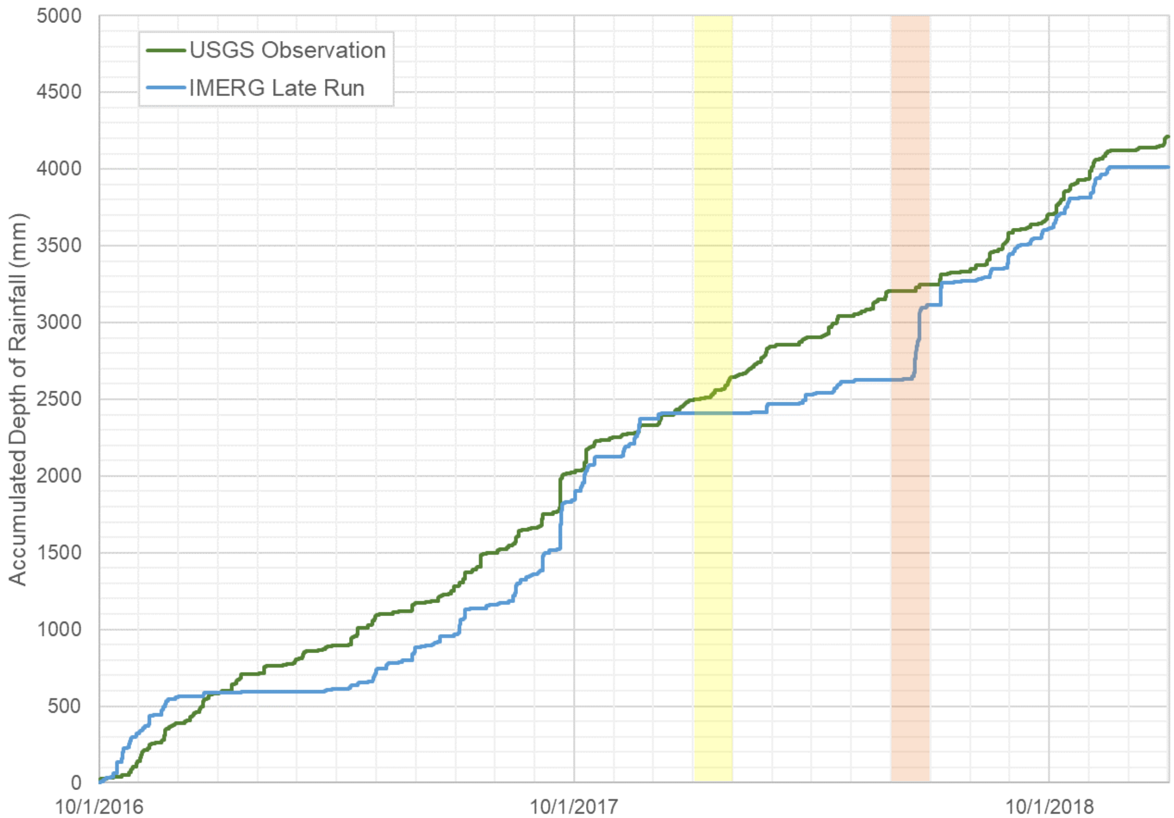

Figure 28: Total rainfall accumulation as measured by USGS 182647066201700 and estimated by IMERG Late Run from October 1, 2016 to December 31, 2018. Data from January of 2018 is highlighted in yellow to show a period of underestimation by IMERG Late Run, while data from June 2018 is highlighted in orange to show a period of overestimation by IMERG Late Run.

The persistent bias toward underestimation is illustrated in Figure 29, comparing simulated and measured streamflow at USGS 50039500 Río Cibuco at Vega Baja for the month of December, 2014. The NSE and KGE values for this watershed are both 0.65 for this month. Notably, the least accurate component of KGE is the ratio of mean simulated and mean observed flows, β, with a value of 0.74 for this month. While the timing of simulated and observed streamflow peaks are highly correlated and display similar variability, a clear bias toward streamflow underestimation is shown. Total rainfall estimates for this month fall below average estimates provided by Parameter-elevation Regressions on Independent Slopes Model (PRISM) precipitation normals for the month of December, suggesting that precipitation was likely underestimated (Daly, Helmer, & Quinones, 2003).

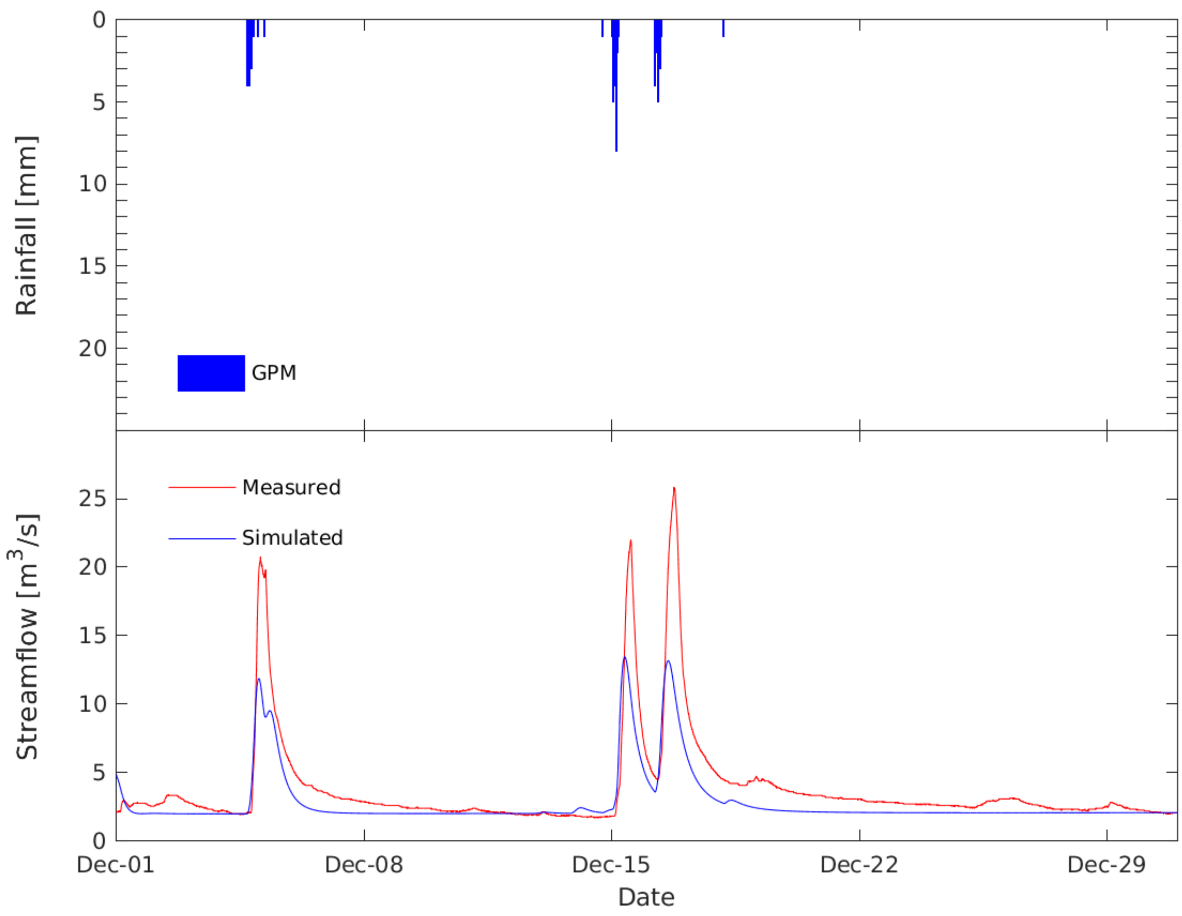

Figure 29: Simulated and measured streamflow at USGS 50039500 Río Cibuco at Vega Baja for the month of December, 2014. Mean areal rainfall values for the watershed as estimated by IMERG Late Run is shown above.

In addition, Figure 30 compares simulated and measured streamflow at USGS 50138000 Río Guanajibo near Hormigueros for the month of February, 2017. The NSE and KGE values for this watershed are 0.06 and 0.41, respectively. No rainfall was estimated by IMERG Late Run during this month so only baseflow is seen in the hydrograph. Notably, the least accurate component of KGE is the correlation coefficient, *r*, with a value of 0.50 for this month. Some storm events are simply not detected so the resulting runoff is not simulated, greatly reducing model performance. This is clearly seen in the first week of February 2017.

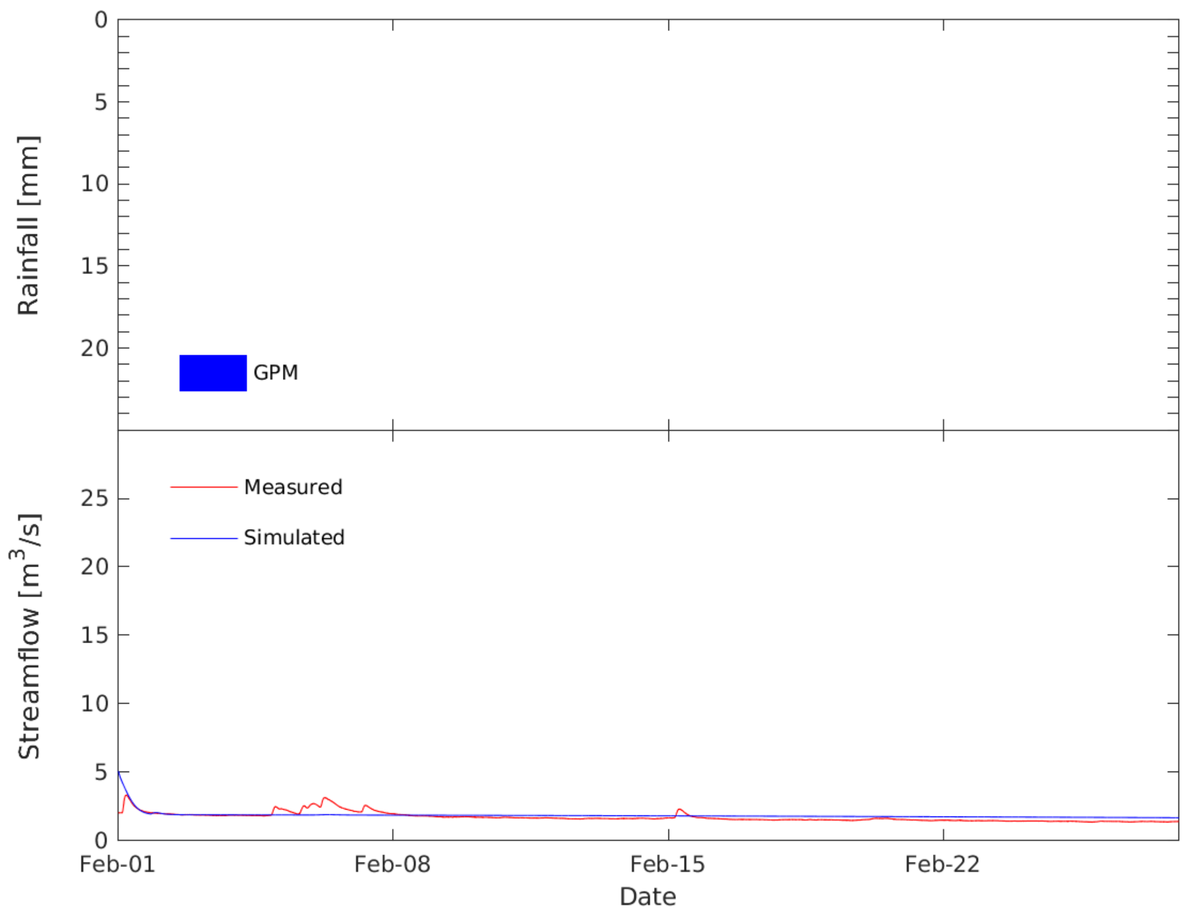

Figure 30: Simulated and measured streamflow at USGS 50138000 Río Guanajibo near Hormigueros for the month of February, 2017. Mean areal rainfall values for the watershed as estimated by IMERG Late Run is shown above.

Together, Figure 29 and Figure 30 illustrate the effects of inaccurate precipitation estimation on streamflow prediction. Underestimation of rainfall reduces the magnitude of predicted peak flows, while failing to detect rainfall allows the model to “miss” streamflow peaks. While the measured flows shown in Figure 30 would not generate flooding, the disconnect between IMERG Late Run estimates and observed streamflow is very clear.

To ensure that the overall water balance is accurate and evapotranspiration estimates are not biased, I computed the monthly average storage of water within each modelled watershed:

$$\Delta S = P - R - ET$$

where ΔS is the monthly change in depth of storage (m), P is the monthly rainfall depth estimated from basin-average climatic rainfall normals, R is the average monthly depth of runoff estimated from USGS streamgage measurements, and ET is the average monthly evapotranspiration rates from basin-average MODIS estimates. The results of these calculations are shown in Table 15. They demonstrate that evapotranspiration is likely not biased, as the change in storage is not highly negative or highly positive in both wet and dry seasons. If evapotranspiration rates were overestimated, a universal storage deficit would be expected. If evapotranspiration rates were underestimated, a universal storage surplus would be expected. Because neither trend is observed, evapotranspiration estimates are likely not causing the poor model performance observed.

Table 15: Monthly average change in water storage

Index	USGS Streamgage	Change in Water Storage (m)											
		Jan.	Feb.	Mar.	Apr.	May	Jun.	Jul.	Aug.	Sep.	Oct.	Nov.	Dec.
5	50014800	0.0	0.0	0.0	0.0	0.0	0.0	0.0	0.0	0.0	0.0	0.0	0.0
9	50025155	0.0	0.0	0.0	-0.1	-0.1	-0.1	-0.1	-0.2	-0.4	-0.1	-0.3	-0.1
10	50026025	0.0	0.0	0.0	0.0	0.0	0.0	0.0	0.0	-0.1	0.0	0.0	0.0
12	50027000	0.0	0.0	0.0	0.0	0.0	0.0	0.0	0.0	-0.1	0.0	-0.1	0.0
13	50028000	0.0	0.0	0.0	0.0	0.0	0.0	0.0	-0.1	-0.1	-0.1	-0.1	0.0
14	50028400	0.0	0.0	0.0	0.0	0.0	0.0	0.0	0.0	-0.1	0.0	-0.1	0.0
16	50031200	0.0	0.0	0.0	0.0	0.0	0.0	0.0	0.0	0.0	0.0	0.0	0.0
19	50034000	0.0	0.0	0.0	-0.1	-0.1	0.0	0.0	-0.1	-0.2	-0.1	-0.2	-0.1
20	50035000	0.0	0.0	0.0	0.0	0.0	0.0	0.0	0.0	0.0	0.0	0.0	0.0
21	50038100	0.0	0.0	0.0	0.0	0.0	0.0	0.0	0.0	0.0	0.0	0.0	0.0
24	50039500	0.0	0.0	0.0	0.0	0.0	0.0	0.0	0.0	0.0	0.0	0.0	0.0
27	50043197	-0.1	-0.1	-0.1	-0.2	-0.2	-0.1	-0.1	-0.2	-0.4	-0.2	-0.4	-0.1
28	50043800	0.0	0.0	0.0	0.0	0.0	0.0	0.0	0.0	0.0	0.0	0.0	0.0
29	50044810	-0.1	-0.1	-0.1	-0.2	-0.2	-0.1	-0.1	-0.2	-0.4	-0.2	-0.4	-0.1
31	50046000	0.0	0.0	0.0	0.0	0.0	0.0	0.0	0.0	0.0	0.0	0.0	0.0
36	50049100	0.0	0.0	0.0	-0.1	-0.1	0.0	0.0	-0.1	-0.2	-0.1	-0.2	-0.1
38	50050900	-0.1	-0.1	-0.1	-0.2	-0.2	-0.1	-0.1	-0.2	-0.5	-0.3	-0.5	-0.2
39	50051310	-0.1	0.0	-0.1	-0.1	-0.1	0.0	0.0	-0.1	-0.3	-0.1	-0.3	-0.1
40	50051800	0.0	0.0	0.0	0.0	0.0	0.0	0.0	0.0	0.0	0.0	0.0	0.0
41	50053025	-0.1	-0.1	-0.1	-0.2	-0.1	-0.1	-0.1	-0.2	-0.4	-0.2	-0.4	-0.1
42	50055000	0.0	0.0	0.0	0.0	0.0	0.0	0.0	0.0	0.0	0.0	0.0	0.0
43	50055225	0.0	0.0	0.0	-0.1	-0.1	0.0	0.0	-0.1	-0.1	-0.1	-0.2	0.0
44	50055380	-0.2	-0.1	-0.1	-0.3	-0.2	-0.1	-0.1	-0.3	-0.5	-0.3	-0.6	-0.2
45	50055750	0.0	0.0	0.0	0.0	0.0	0.0	0.0	0.0	-0.1	-0.1	-0.1	0.0
46	50056400	0.0	0.0	0.0	-0.1	0.0	0.0	0.0	-0.1	-0.1	-0.1	-0.2	0.0
47	50057000	0.0	0.0	0.0	0.0	0.0	0.0	0.0	0.0	0.0	0.0	0.0	0.0
48	50058350	-0.1	-0.1	-0.1	-0.1	-0.1	-0.1	-0.1	-0.2	-0.3	-0.2	-0.4	-0.1

Table 15 – Continued

Index	USGS Streamgage	Change in Water Storage (m)											
		Jan.	Feb.	Mar.	Apr.	May	Jun.	Jul.	Aug.	Sep.	Oct.	Nov.	Dec.
50	50059210	-0.1	0.0	0.0	-0.1	-0.1	0.0	0.0	-0.1	-0.2	-0.1	-0.2	-0.1
51	50061800	-0.1	0.0	0.0	-0.1	-0.1	-0.1	-0.1	-0.1	-0.2	-0.1	-0.3	-0.1
52	50063800	-0.1	0.0	-0.1	-0.1	-0.1	-0.1	-0.1	-0.1	-0.3	-0.2	-0.3	-0.1
53	50064200	-0.1	-0.1	-0.1	-0.1	-0.1	-0.1	-0.1	-0.2	-0.3	-0.2	-0.4	-0.1
54	50065500	-0.1	-0.1	-0.1	-0.1	-0.1	-0.1	-0.1	-0.2	-0.3	-0.2	-0.4	-0.1
55	50067000	-0.2	-0.1	-0.1	-0.3	-0.3	-0.1	-0.1	-0.3	-0.5	-0.3	-0.7	-0.2
57	50071000	0.0	0.0	0.0	0.0	0.0	0.0	0.0	0.0	-0.1	-0.1	-0.1	0.0
58	50075000	-0.6	-0.4	-0.5	-0.8	-0.9	-0.5	-0.5	-1.0	-1.6	-1.0	-2.1	-0.8
60	50081000	-0.1	-0.1	-0.1	-0.1	-0.1	-0.1	-0.1	-0.2	-0.3	-0.2	-0.4	-0.1
61	50083500	0.0	0.0	0.0	0.0	0.0	0.0	0.0	0.0	-0.1	-0.1	-0.1	0.0
62	50085100	0.0	0.0	0.0	0.0	0.0	0.0	0.0	0.0	-0.1	0.0	-0.1	0.0
63	50090500	-0.1	-0.1	-0.1	-0.2	-0.2	-0.1	-0.1	-0.2	-0.4	-0.2	-0.5	-0.2
64	50092000	0.0	0.0	0.0	0.0	0.0	0.0	0.0	-0.1	-0.1	-0.1	-0.1	0.0
65	50093000	-0.2	-0.1	-0.1	-0.2	-0.2	-0.1	-0.1	-0.3	-0.4	-0.3	-0.6	-0.2
72	50106100	0.0	0.0	0.0	0.0	0.0	0.0	0.0	0.0	0.0	0.0	0.0	0.0
74	50110650	0.0	0.0	0.0	0.0	0.0	0.0	0.0	0.0	-0.1	-0.1	-0.1	0.0
75	50110900	0.0	0.0	0.0	0.0	0.0	0.0	0.0	-0.1	-0.1	-0.1	-0.1	0.0
79	50112500	0.0	0.0	0.0	-0.1	-0.1	0.0	0.0	-0.1	-0.2	-0.1	-0.2	-0.1
80	50113800	0.0	0.0	0.0	-0.1	-0.1	0.0	0.0	-0.1	-0.2	-0.1	-0.2	-0.1
83	50114900	-0.1	-0.1	-0.1	-0.1	-0.1	-0.1	-0.1	-0.1	-0.2	-0.1	-0.3	-0.1
84	50115240	0.0	0.0	0.0	-0.1	-0.1	0.0	0.0	-0.1	-0.1	-0.1	-0.2	-0.1
85	50124200	0.0	0.0	0.0	0.0	0.0	0.0	0.0	0.0	-0.1	-0.1	-0.1	0.0
88	50136400	0.0	0.0	0.0	0.0	0.0	0.0	0.0	0.0	-0.1	0.0	-0.1	0.0
89	50138000	0.0	0.0	0.0	0.0	0.0	0.0	0.0	0.0	0.0	0.0	0.0	0.0
90	50144000	0.0	0.0	0.0	0.0	0.0	0.0	0.0	0.0	0.0	0.0	0.0	0.0
92	50147800	0.0	0.0	0.0	0.0	0.0	0.0	0.0	0.0	0.0	0.0	0.0	0.0
93	50148890	0.0	0.0	0.0	0.0	0.0	0.0	0.0	0.0	0.0	0.0	0.0	0.0

6.3.2 Coarse Spatiotemporal Resolution of Rainfall

The spatial and temporal resolution of IMERG Late Run estimates of rainfall is coarse, relative to weather radar. While IMERG Late Run provides rainfall estimates at ~11-km spatial resolution and 30-min temporal resolution, national weather radar networks usually provide rainfall estimates at 1-km spatial resolution and temporal resolutions of 5 or 10 minutes. In order to capture structures and extremes in rainfall that cannot be extrapolated form measurements at coarse resolution, rainfall should be estimated at high resolution, perhaps sub-kilometric scales (Ochoa-Rodriguez et al., 2015). Still, multiple studies have shown that coarse temporal resolution of rainfall inputs has a larger negative effect on hydrodynamic modelling results than spatial resolution (Krajewski, Lakshmi, Georgakakos, & Jain, 1991; Meselhe, Habib, Oche, & Gautam, 2009; Notaro, Fontanazza, Freni, & Puleo, 2013).

Perhaps an appropriate method to increase the utility of IMERG Late Run data for this application is to adopt existing rainfall downscaling techniques capable of reflecting the small-scale statistical properties that are consistent with those of measured precipitation fields (D'Onofrio, von Hardenberg, Provenzale, Palazzi, & Calmanti, 2014; Rebora, Ferraris, von Hardenberg, & Provenzale, 2006). Such a strategy may help address errors caused by coarse spatial resolution. However, addressing limited temporal resolution of IMERG Late Run data may not be viable because rainfall does not exhibit great persistence.

6.4 Comparison to Raingage Forcing

As shown in Figure 8, the historical record of rainfall measurements provided by the USGS is limited. However, sufficient data is available to perform streamflow simulations forced by raingage data during the last half of 2018. Since large floods are of greatest concern, I have focused on three of the five largest modelled watersheds during August, Puerto Rico's wettest month. Figure 31, Figure 32, and Figure 33 show model results forced by both IMERG Late Run and USGS 5-min raingage measurements for USGS 50029000, USGS 50035000, and USGS 50046000, respectively. These watersheds are located on three different major rivers and have many raingages nearby.

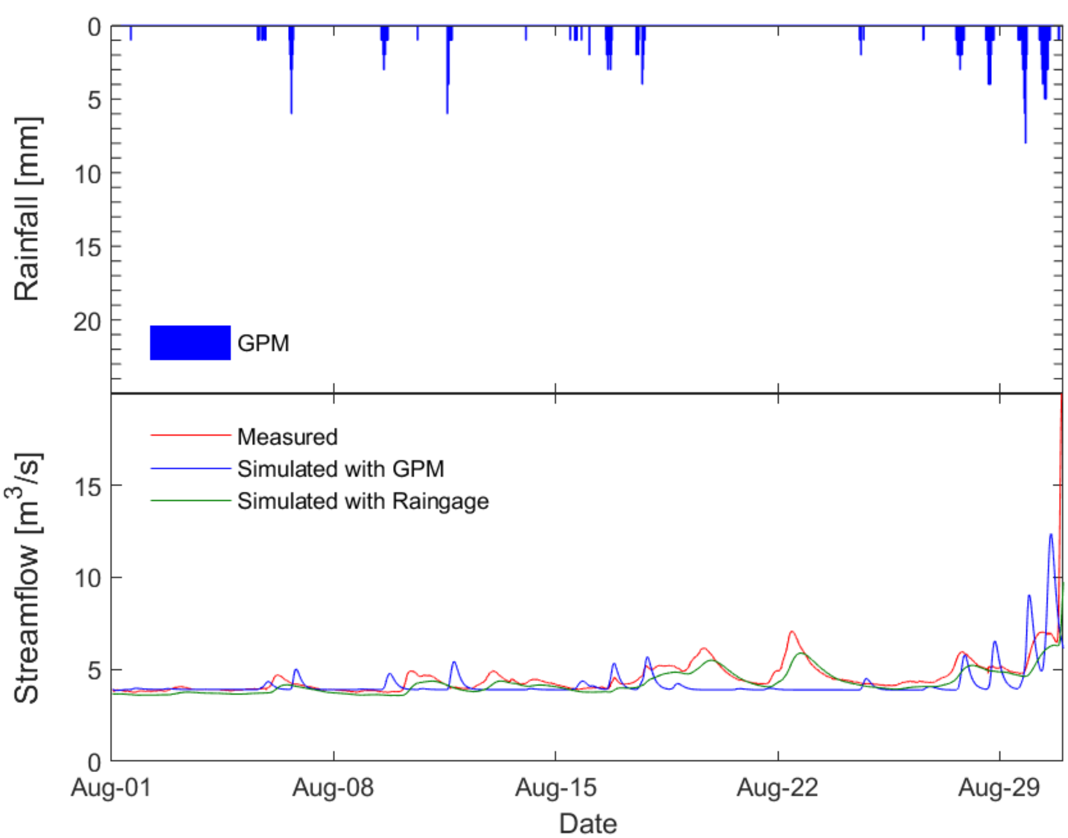

Figure 31: Simulated and measured streamflow at USGS 50029000 Río Grande de Arecibo at Central Cambalache for the month of August, 2018. Mean areal rainfall values for the watershed as estimated by IMERG Late Run is shown above.

Results show that using raingage forcing improves model performance greatly. This indicates that the Iowa Flood Center Top Layer model has skill for large watersheds in Puerto Rico. The included raingage data provides much finer temporal resolution than IMERG Late Run estimates. In addition, raingage measurements are likely closer to the "ground truth" and more accurate than IMERG Late Run estimates. Still, these results from the uncalibrated models show that peak flows are nonetheless underestimated consistently. This indicates that increased accuracy in model parameters is also necessary to sufficiently predict large flood events. Clearly, addressing limitations in IMERG Late Run precipitation estimates is only one part of improving complicated, interconnected model processes.

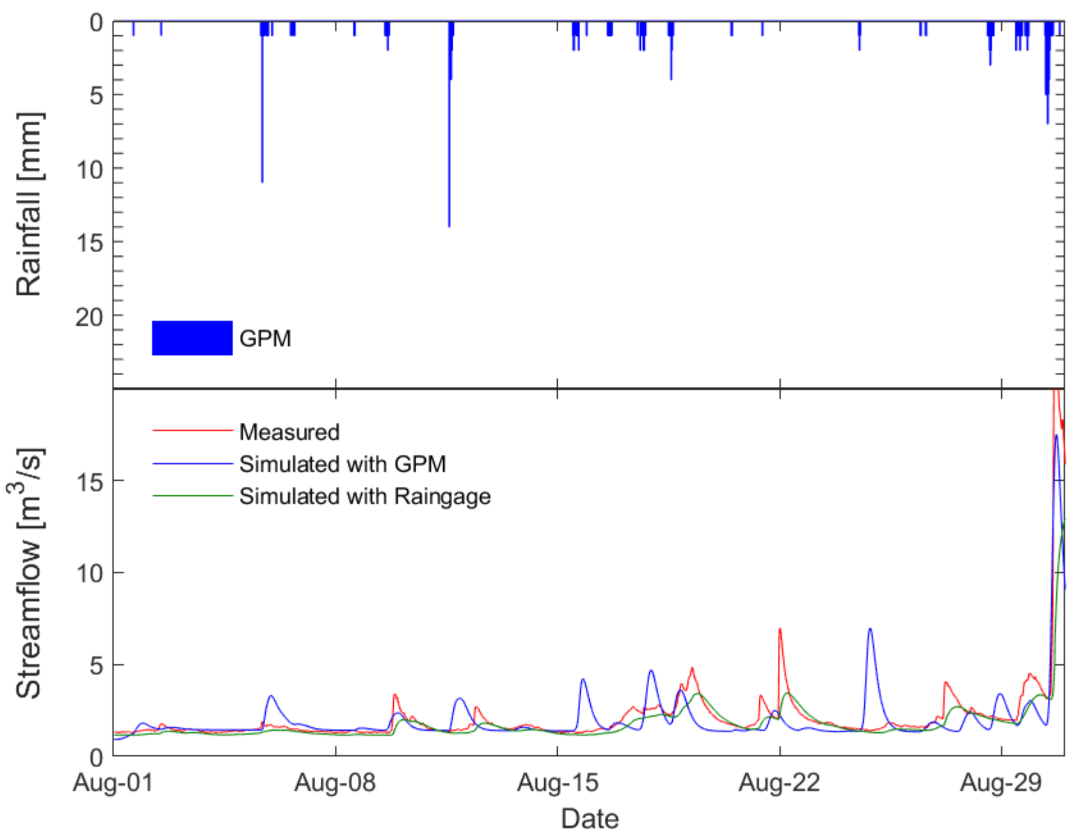

Figure 32: Simulated and measured streamflow at USGS 50035000 Río Grande de Manatí at Ciales for the month of August, 2018. Mean areal rainfall values for the watershed as estimated by IMERG Late Run is shown above.

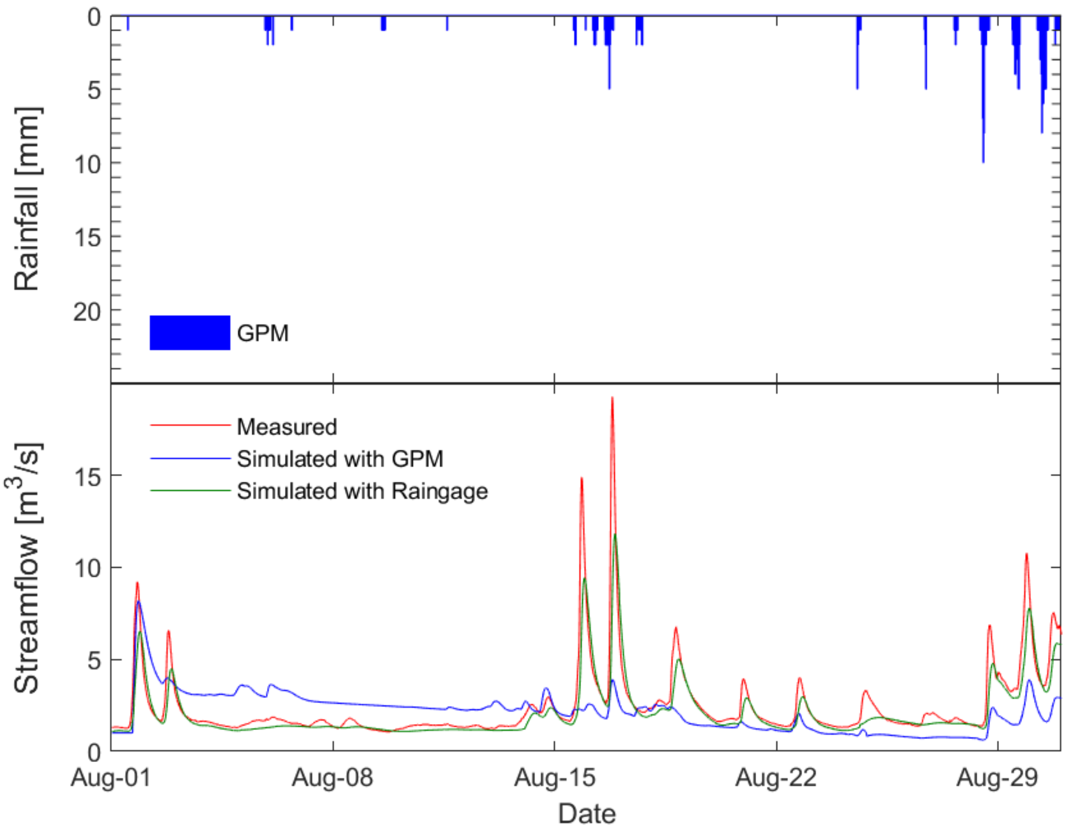

Figure 33: Simulated and measured streamflow at USGS 50046000 Río de la Plata at Highway 2 near Toa Alta for the month of August, 2018. Mean areal rainfall values for the watershed as estimated by IMERG Late Run is shown above.

6.5 Conclusions

Ultimately, the methods presented in this research need to be further developed in order to benefit vulnerable communities. Conceptually, continuous simulation of streamflow by watershed models driven exclusively by satellite remote sensing data is a cutting-edge approach to address the global disparity in flood prediction. Operationally, many sources of error integral to such an approach converge to produce inaccurate flood predictions across spatial and temporal scales. However, I can suggest a number of developments that would likely improve model performance.

Although many developing countries may be considered "data poor," it is unlikely that any are wholly "data bankrupt." Simply put, any and all available in-situ data can help refine modelling efforts. Perhaps satellite remote sensing data should not be used to provide all rainfall forcing, but instead be used to fill gaps in existing raingage and weather radar networks, even if they are sparse. In addition, satellite estimates of rainfall may be bias adjusted by on-the-ground observations. This bias adjustment can vary in space and time, such that regional and seasonal correction factors are applied. Bias adjustment can help limit the influence of persistent underestimation or overestimation of rainfall. In addition, rainfall downscaling may better reflect small scale spatial properties of storm events. And, more accurate estimation of physical model parameters can improve the accuracy of predictions.

Ultimately, truly sustainable solutions to flood-related problems must integrate the local knowledge of the communities that they serve. This research approached flood prediction in Puerto Rico as a top-down exercise, where decisions were made unilaterally to represent conditions from afar. No Puerto Rican scientists, engineers, or forecasters were consulted, nor were any local stakeholders involved. This research was motivated by one question: Can we predict floods from space? In seeking an answer, a wealth of human resources were ignored.

Still, the results of this research show that baseline requirements for flood prediction on the main island of Puerto Rico are likely above what can be provided by satellite remote sensing data alone. Perhaps further advancements in remote sensing technology and algorithms will address the limitations of the current version of IMERG Late Run. And, I hope that advanced modelling techniques like the WMO Flash Flood Guidance System will continue to be developed so that scientists and engineers can more effectively predict floods within the world's most vulnerable communities. This is certainly a step forward.

REFERENCES

Acevedo, G. (1982). *Soil Survey of Arecibo Area of Northern Puerto Rico.* Mayagüez, PR: National Resources Conservation Service, University of Puerto Rico College of Agricultural Sciences.

Ajami, K.N., Gupta, H., Wagener, T., and Sorooshian, S. (2004). Calibration of a Semi-Distributed Hydrologic Model for Streamflow Estimation Along a River System. *Journal of Hydrology*, 298(1–4), 112–135. https://doi.org/10.1016/j.jhydrol.2004.03.033

Allen, R.G., Tasumi, M., and Trezza, R. (2007). Satellite-Based Energy Balance for Mapping Evapotranspiration with Internalized Calibration (METRIC)—Model. *Journal of Irrigation and Drainage Engineering*, 133(4), 395–406. https://doi.org/10.1061/(asce)0733-9437(2007)133:4(395)

Amerian Society of Civil Engineers. (1993). Criteria for Evaluation of Watershed Models. *Journal of Irrigation and Drainage Engineering*, 119(3), 429–442.

Arguez, A., Durre, I., Applequist, S., Russel, S.V., Squires, M.F., Yin, X., Heim, R.R., and Owen, T.W. (2012). NOAA's 1981-2010 U.S. Climate Normals: An Overview. *Bulletin of the American Meteorological Society*, *93*(11), 1687–1697. https://doi.org/10.1175/BAMS-D-11-00197.1

Ayalew, T.B., Krajewski, W.F., and Mantilla, R. (2014). Connecting the Power-Law Scaling Structure of Peak-Discharges to Spatially Variable Rainfall and Catchment Physical Properties. *Advances in Water Resources*, 71, 32–43. https://doi.org/10.1016/j.advwatres.2014.05.009

Azar, D., and Rain, D. (2007). Identifying Population Vulnerable to Hydrological Hazards in San Juan, Puerto Rico. *GeoJournal*, 69(1–2), 23–43. https://doi.org/10.1007/s10708-007-9106-8

Basha, E., and Rus, D. (2008). Design of Early Warning Flood Detection Systems for Developing Countries. *Information and Communication Technologies and Development*, 5(4), 794–799.

Bastiaanssen, W.G.M., Noordman, E.J.M., Pelgrum, H., Davids, G., Thoreson, B.P., and Allen, R.G. (2005). SEBAL Model with Remotely Sensed Data to Improve Water-Resources Management under Actual Field Conditions. *Journal of Irrigation and Drainage Engineering*, 131(1), 85–93. https://doi.org/10.1061/(asce)0733-9437(2005)131:1(85)

Bastiaanssen, W.G.M., Meneti, M., Feddes, R.A., and Holtslag, A.A.M. (1998). A Remote Sensing Surface Energy Balance Algorithm for Land (SEBAL), Part 1: Formulation. *Journal of Hydrology*, 212–213, 198–212. https://doi.org/10.1016/S0022-1694(98)00254-6

Beven, K.J., and Kirkby, M.J. (2010). A Physically Based, Variable Contributing Area Model of Basin Hydrology. *Hydrological Sciences Bulletin*, 24(1), 43–69. https://doi.org/10.1080/02626667909491834

Boccheciamp, R.A. (1977). *Soil Survey of the Humacao Area of Eastern Puerto Rico*. Mayagüez, PR: National Resources Conservation Service, University of Puerto Rico College of Agricultural Sciences.

Boccheciamp, R. A. (1978). *Soil Survey of San Juan Area of Puerto Rico*. Mayagüez, PR: National Resources Conservation Service, University of Puerto Rico College of Agricultural Sciences.

Bonnin, G.M., Martin, D., Lin, B., Parzybok, T., Yekta, M., and Riley, D. (2006). *Precipitation-Frequency Atlas of the United States, Volume 3, Version 4.0: Puerto Rico and the U.S. Virign Islands.* Silver Spring, MD: National Oceanic and Atmospheric Administration.

Brakenridge, G.R., Syvitski, J.P.M., Niebuhr, E., Overeem, I., Higgins, S.A., Kettner, A.J., and Prades, L. (2017). Design with Nature: Causation and Avoidance of Catastrophic Flooding, Myanmar. *Earth-Science Reviews*, 165, 91–109. https://doi.org/10.1016/j.earscirev.2016.12.009

Carter, O.R. (1965). *Soil Survey of the Lajas Valley Area, Puerto Rico*. Mayagüez, PR: National Resources Conservation Service, University of Puerto Rico College of Agricultural Sciences.

Chin, D.A. (2013). *Water-Resources Engineering* (3rd ed.). Upper Saddle River, NJ: Pearson Education Inc.

Cleugh, H.A., Leuning, R., Mu, Q., and Running, S.W. (2007). Regional Evaporation Estimates from Flux Tower and MODIS Satellite Data. *Remote Sensing of Environment*, 106(3), 285–304. https://doi.org/10.1016/j.rse.2006.07.007

D'Onofrio, D., Palazzi, E., von Hardenberg, J., Provenzale, A., and Calmanti, S. (2014). Stochastic Rainfall Downscaling of Climate Models. *Journal of Hydrometeorology*, 15(2), 830–843. https://doi.org/10.1175/jhm-d-13-096.1

Daly, C., Helmer, E.H., and Quinones, M. (2003). Mapping the Climate of Puerto Rico, Vieques and Culebra. *International Journal of Climatology*, 23(11), 1359–1381. https://doi.org/10.1002/joc.937

Della Libera Zanchetta, A. (2017). *IFIS Model-Plus: A Web-Based GUI for Visualization , Comparison and Evaluation of Distributed Hydrologic Model Outputs*. University of Iowa.

Demir, I., and Krajewski, W.F. (2013). Towards an integrated Flood Information System: Centralized Data Access, Analysis, and Visualization. *Environmental Modelling and Software*, 50, 77–84. https://doi.org/10.1016/j.envsoft.2013.08.009

Di Baldassarre, G., Schumann, G., and Bates, P.D. (2009). A Technique for the Calibration of Hydraulic Models Using Uncertain Satellite Observations of Flood Extent. *Journal of Hydrology*, 367(3–4), 276–282. https://doi.org/10.1016/j.jhydrol.2009.01.020

Dinku, T., and Anagnostou, E.N. (2005). Regional Differences in Overland Rainfall Estimation from PR-Calibrated TMI Algorithm. *Journal of Applied Meteorology*, 44(2), 189–205. https://doi.org/10.1175/jam2186.1

Ebel, B. A., and Loague, K. (2006). Physics-Based Hydrologic-Response Simulation: Seeing Through the Fog of Equifinality. *Hydrological Processes*, 20(13), 2887–2900. https://doi.org/10.1002/hyp.6388

Erpul, G., Norton, L.D., and Gabriels, D. (2003). Sediment Transport from Interrill Areas Under Wind-Driven Rain. *Journal of Hydrology*, 276(1–4), 184–197. https://doi.org/10.1016/S0022-1694(03)00070-2

Few, R. (2003). Flooding, Vulnerability and Coping Strategies: Local Responses to a Global Threat. *Progress in Development Studies*, 3(1), 43–58. https://doi.org/10.1191/1464993403ps049ra

Flynn, K.M., Kirby, W.H., and Hummel, P.R. (2006). *Users Manual for Program PeakFQ, Annual Flood Frequency Analysis Using Bulletin 17B Guidelines. Reston, VA: United States Geological Survey*

Gaona, M.F.R., Overeem, A., Leijnse, H., and Uijlenhoet, R. (2016). First-Year Evaluation of GPM Rainfall over the Netherlands: IMERG Day 1 Final Run (V03D). *Journal of Hydrometeorology*, 17(11), 2799–2814. https://doi.org/10.1175/jhm-d-16-0087.1

Garbrecht, J., and Martz, L.W. (1997). The Assignment of Drainage Direction Over Flat Surfaces in Raster Digital Elevation Models. *Journal of Hydrology*, 193(1–4), 204–213. https://doi.org/10.1016/S0022-1694(96)03138-1

García-Pintado, J., Neal, J.C., Mason, D.C., Dance, S.L., and Bates, P.D. (2013). Scheduling Satellite-Based SAR Acquisition for Sequential Assimilation of Water Level Observations into Flood Modelling. *Journal of Hydrology*, 495(2013), 252–266. https://doi.org/10.1016/ j.jhydrol.2013.03.050

Ghimire, G.R., Krajewski, W.F., and Mantilla, R. (2018). A Power Law Model for River Flow Velocity in Iowa Basins. *Journal of the American Water Resources Association*, 54(5), 1055–1067. https://doi.org/10.1111/1752-1688.12665

Gierbolini, R. E. (1975). *Soil survey of Mayagüez Area of Western Puerto Rico*. Mayagüez, PR: National Resources Conservation Service, University of Puerto Rico College of Agricultural Sciences.

Gierbolini, R. E. (1979). *Soil survey of Ponce area of southern Puerto Rico*. Mayagüez, PR: National Resources Conservation Service, University of Puerto Rico College of Agricultural Sciences.

Grecu, M., Olson, W.S., and Anagnostou, E.N. (2004). Retrieval of Precipitation Profiles from Multiresolution, Multifrequency Active and Passive Microwave Observations. *Journal of Applied Meteorology*, 43(4), 562–575. https://doi.org/10.1175/1520-0450(2004)043<0562:roppfm>2.0.co;2

Guo, H., Chen, S., Bao, A., Behrangi, A., Hong, Y., Ndayisaba, F., Hu, J., and Stepanian, P.M. (2016). Early Assessment of Integrated Multi-satellitE Retrievals for Global Precipitation Measurement Over China. *Atmospheric Research*, *176–177*, 121–133. https://doi.org/10.1016/j.atmosres.2016.02.020

Hagen, E., and Teufer, J.F. (2009). Flooding in Afghanistan: A Crisis. In J.A.A. Jones, T.G. Vardanian, and C. Hakopian (Eds.), *Threats to Global Water Security* (pp. 179–185).

Hong, Y., Hsu, K.L., and Gao, X. (2004). Precipitation Estimation from Remotely Sensed Imagery Using an Artificial Neural Network Cloud Classification System. *Journal of Applied Meteorology*, 43(12), 1834–1852. https://doi.org/10.1175/JAM2173.1

Hosseinzadeh, S.R. (2011). Drainage Network Analysis, Comparison of Digital Elevation Model (DEM) from ASTER with High Resolution Satellite Image and Areal Photographs. *International Journal of Environmental Science and Development*, 2(3).

Hou, A.Y., Kakar, R.K., Neeck, S., Azarbarzin, A.A., Kummerow, C.D., Kojima, M., Oki, R., Nakamura, K., and Iguchi, T. (2013). The Global Precipitation Measurement Mission. *Bulletin of the American Meteorological Society*, *95*(5), 701–722. https://doi.org/10.1175/bams-d-13-00164.1

Huffman, G.J., Adler, R.F., Bolvin, D.T., Gu, G., Nelkin, E.J., Wolff, D.B., Bowman, K.P., Hong, Y., Stocker, E.F., and Wolff, D.B. (2007). The TRMM Multisatellite Precipitation Analysis (TMPA): Quasi-Global, Multiyear, Combined-Sensor Precipitation Estimates at Fine Scales. *Journal of Hydrometeorology*, *8*(1), 38–55. https://doi.org/10.1175/jhm560.1

Huffman, G. J., Behrangi, A., Imam, B., Sorooshian, S., Kuligowski, R. J., and Hsu, K. (2009). PERSIANN-MSA: A Precipitation Estimation Method from Satellite-Based Multispectral Analysis. *Journal of Hydrometeorology*, *10*(6), 1414–1429. https://doi.org/10.1175/2009jhm1139.1

Huffman, G. J., Bolvin, D. T., Braithwaite, D., Hsu, K., Joyce, R., Kidd, C., Nelkin, E.J., Sorooshian, S., Tan, J., and Xie, P. (2018). Algorithm Theoretical Basis Document (ATBD) Version 5.2- NASA Global Precipitation Measurement (GPM) Integrated Multi-satellitE Retrievals for GPM (IMERG). *IMERG Algorithm Theoretical Basis Document (ATBD)*, *IMERG Algo*(February), 1–31. https://doi.org/https://pmm.nasa.gov/resources/documents/ gpm-integrated-multi-satellite-retrievals-gpm-imerg-algorithm-theoretical-basis-

Ivette Gómez, L., Munk Ravnborg, H., and Rivas Hermann, R. (2007). *Institucionalidad para la Gestión del Agua en Nicaragua*. Managua, Nicaragua: Instituto de Investigación y Desarollo.

Jackson, R.D., Reginato, R.J., and Idso, S.B. (1977). Wheat Canopy Temperature: A Practical Tool. *Water Resources Research*, 13(3), 651–656. https://doi.org/10.1029/ WR013i003p00651

Jenson, S.K. (1991). Applications of Hydrologic Information Automatically Extracted from Digital Elevation Models. *Hydrological Processes*, 5(1), 31–44. https://doi.org/10.1002/hyp.3360050104

Jenson, S.K., and Domingue, J.O. (1988). Extracting Topographic Structure from Digital Elevation Data for Geographic Information System analysis. *Photogrammetric Engineering and Remote Sensing*, 54(11), 1593–1600. https://doi.org/0099-1112/88/5411-1593$02.25/0

Jiang, L., and Islam, S. (1999). A Methodology for Estimation of Surface Evapotranspiration Over Large Areas Using Remote Sensing Observations. *Geophysical Research Letters*, 26(17), 2773–2776. https://doi.org/10.1029/1999GL006049

Joyce, R.J., and Xie, P. (2011). Kalman Filter–Based CMORPH. *Journal of Hydrometeorology*, 12(6), 1547–1563. https://doi.org/10.1175/jhm-d-11-022.1

Kalin, L., Govindaraju, R. S., and Hantush, M. M. (2003). Effect of Geomorphologic Resolution on Modeling of Runoff Hydrograph and Sedimentograph Over Small Watersheds. *Journal of Hydrology*, 276(1–4), 89–111. https://doi.org/10.1016/S0022-1694(03)00072-6

Kirkby, M. J. (1976). Tests of the Random Network Model, and its Application to Basin Hydrology. *Earth Surface Processes*, 1(3), 197–212. https://doi.org/10.1002/esp.3290010302

Kite, G.W., and Droogers, P. (2000). Comparing Evapotranspiration Estimates from Satellites, Hydrological Models and Field Data. *Journal of Hydrology*, 229(1–2), 3–18. https://doi.org/10.1016/S0022-1694(99)00195-X

Krajewski, W.F., Ceynar, D., Demir, I., Goska, R., Kruger, A., Langel, C., Mantilla, M., Niemeier, J., Quintero, F., Seo, B.C., Small, S.J, Weber, L.J., and Young, N. C. (2017). Real-Time Flood Forecasting and Information System for the State of Iowa. *Bulletin of the American Meteorological Society*, 98(3), 539–554. https://doi.org/10.1175/BAMS-D-15-00243.1

Krajewski, W.F., Lakshmi, V., Georgakakos, K.P., and Jain, S.C. (1991). A Monte Carlo Study of Rainfall Sampling Effect. *Water Resources Research*, 27(1), 119–128.

Kummerow, C.D., Hong, Y., Olson, W.S., Yang, S., Adler, R.F., McCollum, J., Ferraro, R., Petty, G., Shin, D.B., and Wilheit, T. T. (2001). The Evolution of the Goddard Profiling Algorithm (GPROF) for Rainfall Estimation from Passive Microwave Sensors. *Journal of Applied Meteorology*, *40*(11), 1801–1820. https://doi.org/10.1175/1520-0450(2001)040<1801:TEOTGP>2.0.CO;2

Kustas, W.P., and Norman, J.M. (1996). Use of Remote Sensing for Evapotranspiration Monitoring Over Land Surfaces. *Hydrological Sciences Journal*, 41(4), 495–516. https://doi.org/10.1080/02626669609491522

López, M.A., Colón-Dieppa, E., and Cobb, E.D. (1979). *Floods in Puerto Rico, Magnitude and Frequency*. Fort Buchanan, PR: United States Geological Survey.

López, M.A., and Fields, F.K. (1970). *A Proposed Streamflow-Data Program for Puerto Rico*. Fort Buchanan, PR: United States Geological Survey.

Mantilla, R. (2007). *Physical Basis of Statistical Scaling in Peak Flows and Stream Flow Hydrographs for Topologic and Spatially Embedded Random Self-Similiar Channel Networks*. University of Colorado.

Mantilla, R., and Gupta, V.K. (2005). A GIS Numerical Framework to Study the Process Basis of Scaling Statistics in River Networks. *IEEE Geoscience and Remote Sensing Letters*, 2(4), 404–408. https://doi.org/10.1109/LGRS.2005.853571

McCuen, R.H., Knight, Z., and Cutter, A.G. (2006). Evaluation of the Nash–Sutcliffe Efficiency Index. *Journal of Hydrologic Engineering*, 11(6), 597–602. https://doi.org/10.1061/(asce)1084-0699(2006)11:6(597)

Meselhe, E.A., Habib, E.H., Oche, O.C., and Gautam, S. (2009). Sensitivity of Conceptual and Physically Based Hydrologic Models to Temporal and Spatial Rainfall Sampling. *Journal of Hydrologic Engineering*, 14(7), 711–720. https://doi.org/10.1061/(asce)1084-0699(2009)14:7(711)

Milly, P.C.D., Betancourt, J., Falkenmark, M., Hirsce, R.M., Kundzewicz, Z.W., Lettenmaeier, D.P., and Stouffer, R.J. (2008). Stationarity Is Dead: Whither Water Management? *Science, 319(5863),* 573–574. https://doi.org/10.1126/science.1151915

Moore, R.B., and Dewald, T.G. (2016). The Road to NHDPlus- Advancements in Digital Stream Networks and Associated Catchments. *Journal of the American Water Resources Association*, 52(4), 890–900. https://doi.org/10.1111/1752-1688.12389

Mu, Q., Zhao, M., and Running, S. (2013). MODIS Global Terrestrial Evapotranspiration (ET) Product (NASA MOD16A2/A3). *Algorithm Theoretical Basis Document, Collection 5*. Missoula, MT: The University of Montana College of Forestry and Conservation Numerical Terradynamic Simulation Group

Noel, C. (1990). The Origins of Kriging. *Mathematical Geology*, *22*(3), 47–55.

Notaro, V., Fontanazza, C.M., Freni, G., and Puleo, V. (2013). Impact of Rainfall Data Resolution in Time and Space on the Urban Flooding Evaluation. *Water Science and Technology*, 68(9), 1984–1993. https://doi.org/10.2166/wst.2013.435

Ntelekos, A.A., Georgakakos, K.P., and Krajewski, W.F. (2006). On the Uncertainties of Flash Flood Guidance: Toward Probabilistic Forecasting of Flash Floods. *Journal of Hydrometeorology*, *7*(5), 896–915. https://doi.org/10.1175/jhm529.1

O'Callaghan, J.F., and Mark, D.M. (1989). The Extraction of Drainage Networks from Digital Elevation Data. *Computer Vision, Graphics and Image Processing*, *47*(1), 45–58. https://doi.org/10.1016/0734-189X(89)90053-4

O'Loughlin, E.M. (1986). Prediction of Surface Saturation Zones in Natural Catchments by Topographic Analysis. *Water Resources*, *22*(5), 794–804.

Ochoa-Rodriguez, S., Wang, L.P., Gires, A., Daniel Pina, R., Reinoso-Rondinel, R., Bruni, G., Ichiba, A., Gaitan, S., Cristiano, E., van Assel, J., Kroll, S., Murla-Tuyls, D., Bruno, T., Schertzer, D., Tchiguirinskaia, I., Onof, C., Willems, P., and ten Veldhuis, M.C. (2015). Impact of Spatial and Temporal Resolution of Rainfall Inputs on Urban Hydrodynamic Modelling Outputs: A Multi-Catchment Investigation. *Journal of Hydrology*, 531, 389–407. https://doi.org/10.1016/j.jhydrol.2015.05.035

Pai, D.S., Norouzi, H., Prakash, S., Liu, Z., AghaKouchak, A., and Mitra, A.K. (2016). A Preliminary Assessment of GPM-Based Multi-Satellite Precipitation Estimates Over a Monsoon Dominated Region. *Journal of Hydrology*, *556*, 865–876. https://doi.org/10.1016/ j.jhydrol.2016.01.029

Petty, G.W., and Krajewski, W.F. (2010). Satellite Estimation of Precipitation Over Land. *Hydrological Sciences Journal*, 41(4), 433–451. https://doi.org/10.1080/02626669609491519

Prabhakara, C., Iacovazzi, R.J., and Yoo, J.M. (2004). TRMM Precipitation Radar and Microwave Imager Observations of Convective and Stratiform Rain Over Land and their Theoretical Implications. *Journal of the Meteorological Society of Japan*, 80(5), 1183–1197. https://doi.org/10.2151/jmsj.80.1183

Puerto Rico Department of Natural Resources. (1980). *Coastal flood hazards and responses in Puerto Rico, An Overview: San Juan, Puerto Rico*. San Juan, PR: National Oceanic and Atmospheric Administration Coastal Services Center

Quintero, F., Mantilla, R., Anderson, C., Claman, D., and Krajewski, W.F. (2018). Assessment of Changes in Flood Frequency Due to the Effects of Climate Change: Implications for Engineering Design. *Hydrology*, 5(1), 19. https://doi.org/10.3390/hydrology5010019

Ramos-Gines, O. (1999). *Estimation of Magnitude and Frequency of Floods for Streams in Puerto Rico: New Empirical Models.* Guaynabo, PR: United States Geological Survey.

Rebora, N., Ferraris, L., von Hardenberg, J., and Provenzale, A. (2006). RainFARM: Rainfall Downscaling by a Filtered Autoregressive Model. *Journal of Hydrometeorology*, 7(4), 724–738. https://doi.org/10.1175/jhm517.1

Rodríquez-Martínez, J., and Santiago, M. (2016). *The Effects of Forest Cover on Base Flow of Streams in the Mountainous Interior of Puerto Rico, 2010*. Reston, VA: United States Geological Survey.

Sawicz, K., Wagener, T., Sivapalan, M., Troch, P.A., and Carrillo, G. (2011). Catchment Classification: Empirical Analysis of Hydrologic Similarity Based on Catchment Function in the Eastern USA. *Hydrology and Earth System Sciences*, 15(9), 2895–2911. https://doi.org/10.5194/hess-15-2895-2011

Scanlon, B. R., Keese, K. E., Flint, A. L., Flint, L. E., Gaye, C. B., Edmunds, W. M., and Simmers, I. (2006). Global synthesis of groundwater recharge in semiarid andaridregions Bridget. *Hydrological Processes*, *20*(June 2008), 3335–3370. https://doi.org/10.1002/hyp

Schanze, J., Zeman, E., and Marsalek, J. (2006). *Flood Risk Management: Hazards, Vulnerability and Mitigation Measures*. Dordrecht, The Netherlands: Springer.

Schumann, G., and Di Baldassarre, G. (2010). The Direct Use of Radar Satellites for Event-Specific Flood Risk Mapping. *Remote Sensing Letters*, 1(2), 75–84. https://doi.org/10.1080/ 01431160903486685

Schumann, G., Matgen, P., Hoffmann, L., Hostache, R., Pappenberger, F., and Pfister, L. (2007). Deriving Distributed Roughness Values from Satellite Radar Data for Flood Inundation Modelling. *Journal of Hydrology*, 344(1–2), 96–111. https://doi.org/10.1016/ j.jhydrol.2007.06.024

Sharifi, E., Steinacker, R., and Saghafian, B. (2016). Assessment of GPM-IMERG and Other Precipitation Products Against Gauge Data Under Different Topographic and Climatic Conditions in Iran: Preliminary Results. *Remote Sensing*, 8(2). https://doi.org/10.3390/ rs8020135

Skakun, S., Kussul, N., Shelestov, A., and Kussul, O. (2014). Flood Hazard and Flood Risk Assessment Using a Time Series of Satellite Images: A Case Study in Namibia. *Risk Analysis*, 34(8), 1521–1537. https://doi.org/10.1111/risa.12156

Small, S.J., Jay, L.O., Mantilla, R., Curtu, R., Cunha, L.K., Fonley, M., and Krajewski, W.F. (2012). An Asynchronous Solver for Systems of ODEs Linked by a Directed Tree Structure. *Advances in Water Resources*, 53, 23–32. https://doi.org/10.1016/j.advwatres.2012.10.011

Smith, J.A., Paula, S.R., and Baeck, M.L. (2005). Tropical Cyclones and the Flood Hydrology of Puerto Rico. *Water Resources Research*, 41(6), 1–16. https://doi.org/10.1029/2004WR003530

Spencer, R.W., Goodman, M.H., and Hood, R.E. (1988). Precipitation Retrieval over Land and Ocean with the SSM/I: Identification and Characteristics of the Scattering Signal, *Journal of Atmospheric and Oceanic Technology*, 6, 254–273.

Stedinger, J.R., and Griffis, V.W. (2008). Flood Frequency Analysis in the United States: Time to Update. *Journal of Hydrologic Engineering*, 13(4), 199–204. https://doi.org/10.1061/(asce)1084-0699(2008)13:4(199)

Stephens, E.M., Bates, P.D., Freer, J.E., and Mason, D.C. (2012). The Impact of Uncertainty in Satellite Data on the Assessment of Flood Inundation Models. *Journal of Hydrology*, 414–415, 162–173. https://doi.org/10.1016/j.jhydrol.2011.10.040

Stephens, G.L., and Kummerow, C.D. (2007). The Remote Sensing of Clouds and Precipitation from Space: A Review. *Journal of the Atmospheric Sciences*, 64(11), 3742–3765. https://doi.org/10.1175/2006jas2375.1

Strahler, A.N. (1957). Quantitative Analysis of Watershed Geomorphology. *American Geophysical Union Transactions*, 38(6), 913–920.

Sungmin, O., Foelsche, U., Kirchengast, G., Fuchsberger, J., Tan, J., and Petersen, W.A. (2017). Evaluation of GPM IMERG Early, Late, and Final Rainfall Estimates Using WegenerNet Gauge Data in Southeastern Austria. *Hydrology and Earth System Sciences*, 21(12), 6559–6572. https://doi.org/10.5194/hess-21-6559-2017

Tan, J., Petersen, W.A., and Tokay, A. (2016). A Novel Approach to Identify Sources of Errors in IMERG for GPM Ground Validation. *Journal of Hydrometeorology*, 17(9), 2477–2491. https://doi.org/10.1175/jhm-d-16-0079.1

Tang, G., Ma, Y., Long, D., Zhong, L., and Hong, Y. (2016). Evaluation of GPM Day-1 IMERG and TMPA Version-7 Legacy Products Over Mainland China at Multiple Spatiotemporal Scales. *Journal of Hydrology*, 533, 152–167. https://doi.org/10.1016/j.jhydrol.2015.12.008

Tang, Q., Gao, H., Lu, H., and Lettenmaier, D.P. (2009). Remote Sensing: Hydrology. *Progress in Physical Geography*, 33(4), 490–509. https://doi.org/10.1177/0309133309346650

Tarboton, D.G., Bras, R.L., and Rodriguez-Iturbe, I. (1991). On the Extraction of Channel Networks from Digital Elevation Data. *Hydrological Processes*, 5, 81–100. https://doi.org/ 10.1002/hyp.3360050107

The National Research Council. (2003). Predictability and Limits to Prediction in Hydrologic Systems. *Eos*, 82(2).

Thwin, S., Chan, N., Fritz, H.M., Thu, M.K., and Blount, C. (2011). Observations and Modeling of Cyclone Nargis Storm Surge in Myanmar, *Solution to Coastal Disasters*, 1–9. https://doi.org/10.1061/41185(417)1

Tramblay, Y., Bouaicha, R., Brocca, L., Dorigo, W., Bouvier, C., Camici, S., and Servat, E. (2012). Estimation of Antecedent Wetness Conditions for Flood Modelling in Northern Morocco. *Hydrology and Earth System Sciences*, 16(11), 4375–4386. https://doi.org/10.5194/hess-16-4375-2012

United States Interagency Advisory Committee on Water Data. (1982). *Guidelines for Determining Flood Flow Frequency: Bulletin 17B.* Reston, VA: Hydrology Subcommittee, Office of Water Data Coordination, United States Geological Survey.

United Nations Department of Economic and Social Affairs. (2018). *World Economic Situations and Perspectives, 2018*. https://doi.org/10.1007/BF02929547

United States Water Resources Council (1978). *The Nation's Water Resources 1975-2000, Volume 4: Caribbean Region.* Washington, D.C.: United States Government Printing Office.

Wan, Z., Zhang, Y., Zhang, Q., and Li, Z.L. (2004). Quality Assessment and Validation of the MODIS Global Land Surface Temperature. *International Journal of Remote Sensing*, 25(1), 261–274. https://doi.org/10.1080/0143116031000116417

Wang, Z., Zhong, R., Lai, C., and Chen, J. (2017). Evaluation of the GPM IMERG Satellite-Based Precipitation Products and the Hydrological Utility. *Atmospheric Research*, 196, 151–163. https://doi.org/10.1016/j.atmosres.2017.06.020

Ward, P.J., Jongman, B., Weiland, F.S., Bouwman, A., van Beek, R., Bierkens, M.F.P., Ligtvoet, W., and Winsemius, H.C. (2013). Assessing Flood Risk at the Global Scale: Model Setup, Results, and Sensitivity. *Environmental Research Letters*, *8*(4), 44019. https://doi.org/ 10.1088/1748-9326/8/4/044019

Winsemius, H.C., Van Beek, L.P.H., Jongman, B., Ward, P.J., and Bouwman, A. (2013). A Framework for Global River Flood Risk Assessments. *Hydrology and Earth System Sciences*, 17(5), 1871–1892. https://doi.org/10.5194/hess-17-1871-2013

World Meteorological Organization. (2014). *Atlas of Mortality and Economic Losses from Weather, Climate and Water Extremes*. Geneva, Switzerland: World Meteorological Organization. https://doi.org/ISBN 978-92-63-11123-4

World Meteorological Organization. (2016). *Development and Implementation of International and Regional Flash Flood Guidance (FFG) and Early Warning Systems*.

World Meteorological Organization. (2016). *Development and Implementation of the Southeastern Asia-Oceania Flash Flood Guidance (SAOFFG)*. Geneva, Switzerland: World Meteorological Organization.

World Meteorological Organization. (2016). *Establishment of a Flash Flood Guidance System for South America*. Geneva, Switzerland: World Meteorological Organization.

World Meteorological Organization. (2017a). *Central America Flash Flood Guidance (CAFFG) System First Steering Committee Meeting (SCM1)*. Geneva, Switzerland: World Meteorological Organization.

World Meteorological Organization. (2017b). *Follow-Up Operational Workshop Central Asia Region Flash Flood Guidance (CARFFG) System*. Geneva, Switzerland: World Meteorological Organization.

World Meteorological Organization. (2017c). *Initial Planning Meeting of the Southeast Asia Flash Flood Guidance System (SeAFFGS)*. Geneva, Switzerland: World Meteorological Organization.

World Meteorological Organization. (2018a). *Development and Implementation of the Myanmar Flash Flood Guidance System (MyanmarFFGS) Initial Planning Meeting Final Report.* Geneva, Switzerland: World Meteorological Organization.

World Meteorological Organization. (2018b). *Development and Implementation of the Northwest South America Flash Flood Guidance System (NWSAFFGS) Initial Planning Meeting Final Report.* Geneva, Switzerland: World Meteorological Organization.

World Meteorological Organization. (2018c). *Follow-up Operational Workshop South Asia Region Flash Flood Guidance (SAsiaFFG) System Report*. Geneva, Switzerland: World Meteorological Organization.

World Meteorological Organization. (2018d). *Report of the Second Steering Committee Meeting (SCM 2) of the Haiti and Dominican Republic Flash Flood Guidance System.* Geneva, Switzerland: World Meteorological Organization.

Yan, K., Di Baldassarre, G., Solomatine, D.P., and Schumann, G.J.P. (2015). A Review of Low-Cost Space-Borne Data for Flood Modelling: Topography, Flood Extent and Water Level. *Hydrological Processes*, 29(15), 3368–3387. https://doi.org/10.1002/hyp.10449

Zehe, E., and Blöschl, G. (2004). Predictability of Hydrologic Response at the Plot and Catchment Scales: Role of Initial Conditions. *Water Resources Research*, 40(10), 1–21. https://doi.org/10.1029/2003WR002869